

N72-15940

NASA TECHNICAL
MEMORANDUM

NASA TM X-62,110

NASA TM X-62,110

**CASE FILE
COPY**

INITIAL ROTATION-LOADING AND LOW-SPEED FLUTTER
TEST RESULTS FOR A STRAIGHT WING VERSION
OF THE SPACE SHUTTLE VEHICLE

Robert W. Warner, Phillip R. Wilcox, and Bruno J. Gambucci

Ames Research Center
Moffett Field, Calif. 94035

January 1972

ABSTRACT

For three straight semispan model space shuttle wings, the maximum total load (including vibrations) during rapid rotation from 66° to 0° angle of attack, at Mach numbers from 0.28 to 0.60, was essentially no higher than that measured (non-statistically) for buffet. During slow rotation over the same angle range, there was no visible flutter. For one of the wings, however, unstable aerodynamic damping was established at two fixed angles of attack.

INITIAL ROTATION-LOADING AND LOW-SPEED FLUTTER TEST
RESULTS FOR A STRAIGHT WING VERSION OF THE
SPACE SHUTTLE VEHICLE

by

Robert W. Warner

Phillip R. Wilcox

and

Bruno J. Gambucci

SUMMARY

Loading and flutter results are presented for rapid rotation and slow rotation from 66° to 0° angle of attack for three semispan model space shuttle wings (straight, aspect ratio 7, semispan 5 ft.), together with total damping results at selected fixed angles. Mach numbers ranged from 0.28 to 0.60, Reynolds numbers per foot from 0.32×10^6 ft.⁻¹ to 3.66×10^6 ft.⁻¹, and dynamic pressures from 21 psf to 243 psf. The maximum total load (including vibrations) was not more than 12 percent higher than the maximum mean load during rapid rotation scaled from the prototype, as compared to 11 percent for (non-statistical) buffet in the present test and 17 percent in a previous test. There was no visible flutter during slow rotation. "Near flutter" (stable total damping but zero or unstable aerodynamic damping) was established at several conditions for the basic wing but not for the torsionally stiffer wing or for the torsionally stiffer wing with a leading edge spoiler.

INTRODUCTION

During its return to earth, the space shuttle orbiter enters the atmosphere at an angle of attack of approximately 60° for braking purposes. At a specified design Mach number, in the range from low supersonic to low subsonic, the orbiter rotates rapidly to a lifting attitude. The resulting rapid load change suggests the possibility of structural vibrations large enough to cause a significant dynamic overload, and the passage through the stall region suggests the possibility of stall flutter. The present purpose is to investigate these possibilities experimentally at low subsonic Mach numbers for the straight, thick, high-aspect-ratio wing of reference 1 and for two variations from that wing. An auxiliary purpose is to search for low damping at fixed angles of attack.

At fixed angles of attack, stall flutter has already been investigated for the straight wing of the space shuttle (references 2 and 3), but for a

smaller model than the present wings and without a boundary layer trip. Also at fixed angles, stall flutter has been investigated in reference 1, but at high subsonic and low supersonic Mach numbers.

NOTATION

"A"	denotes basic wing
a_∞	free-stream speed of sound
"B"	denotes torsionally stiffer wing
"BSP"	denotes torsionally stiffer wing with leading-edge spoiler
b	wing semichord at 3/4 semispan
C_N	normal force coefficient, $\frac{\text{normal force}}{S q_\infty}$
c_r	root chord
c_t	tip chord
f	frequency, HZ
h	bending deflection signal
M	free stream Mach number
P_t	tunnel total pressure
q_∞	free stream dynamic pressure
R_D	ratio of the mean load at the minimum in the load curve immediately after the stall to the maximum mean load
R_{DL}	ratio of the maximum total load, including vibrations, to the maximum mean load
R_S	ratio of the mean load at stall to the maximum mean load
S	twice the planform area of the semispan wing model
α	geometric angle of attack relative to wind tunnel centerline
ζ	damping ratio
θ	torsional deflection signal
μ	relative density of wing, i.e., semispan wing mass divided by mass of air in truncated cone with semispan wing as diameter
ρ_∞	free stream air density
ω_α	highest frequency involving first torsion

TEST EQUIPMENT AND PROCEDURE

The model wing geometry is shown in figure 1, a schematic of the rotation mechanism for the wing in figure 2, photographs of the rotation mechanism in figure 3, the wing model installation in the 12-foot pressure wind tunnel in figure 4, operating characteristics of the wind tunnel in figure 5, the mode shape frame in figure 6, still-air mode shapes in figures 7 and 8, and a sample unfiltered spectrum in figure 9.

Models

The model designated wing "A" in the present report is the wing model 2 of reference 1. As pointed out therein, the planform and section parameters for wing "A" (and for all the present wings) are:

$$\text{Aspect ratio} = \frac{(\text{full span})^2}{S} = \frac{(120)^2}{2070} \approx 7$$

$$\text{Taper ratio} = \frac{c_t}{c_r} = \frac{9}{25.5} = 0.353$$

$$\text{Leading edge sweep} \approx 14^\circ$$

$$\text{Semispan wing area} = \frac{S}{2} = 1035 \text{ in.}^2$$

Airfoil profile (parallel to the flow): NACA OOX-64

Root thickness ratio = 14%

Tip thickness ratio = 10%

All wings are supported by the same steel tongue. The tongue slips into a tapered cavity (figure 1) in the base of each wing, a cavity molded into a metallic potting material. The tongue extends 11.6 inches into the wing, a distance corresponding to the wing-fuselage intersection on the full-scale space shuttle vehicle.

As indicated in figure 1 and in reference 1, wing "A" has a fiberglass skin over a stiff plastic foam interior with a birch spar at the 20% chord position. The mass ratio μ for the outer 80% of the semispan is

$$= \frac{608 \times 10^{-4}}{\rho_\infty}$$

with ρ_∞ designating the free stream air density in slugs/ft.³. For the present tests, the range of μ is defined by:

$$\mu = 13.7 \text{ at } M = 0.3, p_t = 4107 \text{ psf}$$

$$\mu = 156 \text{ at } M = 0.6, p_t = 381 \text{ psf}$$

Additional information on the physical characteristics of wing "A" can be found in reference 1.

Wings "B" and "BSP" have no spar but have approximately the same mass and μ values as wing "A". They have a 0.020-inch thick 2024 T3 aluminum skin over a honeycomb interior with fiberglass leading and trailing edges. The honeycomb is filled with stiff plastic foam over the first (upstream) 14% and last 16.5% of the chord but is otherwise unfilled. For wing "B", the bending deflections per unit tip load are the same as those for wing "A" (figure 9 of reference 1) and the twist angles per unit tip torque (pure couple) are one-fourth those for wing "A" (figure 10 of reference 1). The bending deflections and tip load were at 40% chord, and the twist angles were measured in planes normal to the 40% chord line.

These stiffness comparisons are assumed applicable to wing "BSP" also, since "BSP" is simply "B" with a light leading edge spoiler added. The spoiler is a fiberglass "T" section with the flanges (0.025" thick) glued to the wing so that the projection normal to the wing (0.050" thick) is on the 25% chord line. The projection height and flange widths are 5% of the chord, ranging from 0.45" at the tip to 1.11" at the inboard end of the spoiler (11.6" from the root).

Rotation Mechanism for Models

As indicated in figure 1, the models are supported by a tongue which has a rotation axis passing through the quarter chord point of the mean aerodynamic chord. This rotation is provided by mounting the tongue on the rotation mechanism of figures 2 and 3. The hydraulic cylinder (actuator) drives the wing from 66° to roughly 0° angle of attack in as little as 0.4 seconds (A rotation time of 0.6 second for the model corresponds to the estimated full scale rotation time of 6 seconds.) The time history of angular displacement is roughly the integral of a half sine wave velocity pulse and approximates the prototype time history estimated by analog computer simulation. This time history is achieved by a servo valve, shown in figure 2(a), together with a displacement feedback system and servo command. The displacements are measured by an angular potentiometer.

It was required of the rotation mechanism developed for the present test that the rapid rotation just described be achieved while retaining adequate base fixity for overload and flutter testing. In an attempt to meet this requirement, a massive design was utilized as seen in figure 3, where the rotating disk is 1-1/2 inches thick. In addition, heavy duty thrust bearings with close tolerances were used. The bearings are shown schematically in figure 2 and were located at the ends of the longest shaft that would fit into the wind tunnel mounting region. Specifically, the bearings are 6-1/8 inches apart on a tubular shaft having a 5-5/16 inch outside diameter and a 7/8 inch wall thickness. The inside of the shaft contains the feedback potentiometer already mentioned and a second potentiometer used for recording angle of attack.

For additional root fixity in the various rocking modes of the rotating disk, an upstream clamp and a downstream clamp were added, as seen in figures 2 and 3. These clamps minimized rocking directly by their column forces and indirectly by tightening the upper thrust bearing. They could be activated and deactivated hydraulically at any fixed angle of attack.

Apparatus and Instrumentation

The Ames 12-foot pressure wind tunnel was used in the present test, with model installation shown in figure 4. The wind tunnel is a variable-density, low-turbulence type that operates at subsonic speeds. Its operating characteristics are given in figure 5.

Wing oscillations and wing loads were sensed by strain gage bridges located in one-inch-wide slots in the tongue. The elements of the bridge in the center slot are arranged in a 45-degree pattern relative to the air stream, and this bridge is referred to as the "torsion gage". The elements of the other two bridges are normal to the air stream, and these bridges are referred to as the "forward bending gage" and the "rear bending gage".

Frequencies, Damping Values, and Mode Shapes in Still Air

All still-air vibrations were activated with the model wings mounted in the wind tunnel, as in figure 4. Several angles of attack were used to check their effect on root fixity. All damping ratios and the corresponding natural frequencies were found from decays which followed either a tap on the wing tip with a mallet or a sudden shut-off of the air supply to an air exciter at the wing tip.

The air exciter was particularly useful for high frequency modes, but was used sparingly because it was a bulky device to move in and out of the wind tunnel. It consisted of two large wheels driven by an electric motor, with gear teeth arranged on the wheel circumferences so as alternately to interrupt high-pressure air jets on either side of the wing tip.

Still-air frequency and damping results are given in the following table for wing "A" ("Clamped" means that the upstream and downstream hydraulic clamps of figure 3 were activated and that check valves prevented, or nearly prevented, return flow from the hydraulic actuator; "pressure off" means that hydraulic pressure was removed from the actuator, after positioning, but not from the clamps; wing root was at room temperature unless otherwise specified; frequencies given without damping values were estimated from wind-on results at low dynamic pressure):

Mode	f Frequency HZ	ζ (Damping in % of Critical)	α Degrees	Excitation Prior to Decay	Before or After Wind-on Test	Wing Root Conditions
1st bending	34.0	2.1%	5	Air at leading edge	before	Clamped, pressure on
1st bending	31.6	1.0%	0	Mallet	before	Clamped, pressure off
1st bending	34.0	1.4%	0	Mallet	before	Clamped, pressure off Wing root at 130°F
1st bending	31.1	1.2%	15	Mallet	before	Clamped, pressure off
1st bending	28.1	4.1%	0	Mallet	before	Unclamped, pressure on
1st bending	31.7	1.8%	15	Mallet	after	Clamped, pressure on
1st bending	32.3	2.6%	60	Mallet	after	Clamped, pressure on
2nd bending	85	1.7%	5	Air at leading edge	before	Clamped, pressure on
1st torsion and 2nd bending	110	2.1%	5	Air at leading edge	before	Clamped, pressure on
1st torsion and 2nd bending	99	1.5%	15	Mallet	after	Unclamped, pressure on
1st torsion and 2nd bending	100	2.8%	60	Mallet	after	Unclamped, pressure on
1st torsion and 3rd bending	133					
3rd bending and 2nd torsion	175	1.4%	5	Air at leading edge	before	Clamped, pressure on

For wing "B", frequency and damping values in still air are given in the following table (with terminology as for wing "A"):

Mode	Frequency HZ	ζ (Damping in % of Critical)	α Degrees	Excitation Prior to Decay	Before or After Wind-on Test	Wing Root Conditions
1st bending	34	1.9%	15	Mallet	Before	Clamped, pressure on
1st bending	34	2.4%	60	Mallet	Before	Clamped, pressure on
2nd bending	85					
1st torsion	140	2.3%	15	Mallet	Before	Unclamped, pressure on
3rd bending	185					
2nd torsion	300					
And for wing "BSP"						
1st bending	32.0	1.2%	0	Mallet	After	Clamped, pressure off
1st bending	31.9	1.3%	15	Mallet	After	Clamped, pressure off
1st bending	32.4	1.4%	60	Mallet	After	Clamped, pressure off
1st bending	32.6	6.7%	60	Mallet	After	Unclamped, pressure on
2nd bending	85					
1st torsion	136	0.9%	15	Mallet	After	Unclamped, pressure on
1st torsion	133	1.9%	60	Mallet	After	Unclamped, pressure on
3rd bending	185					
2nd torsion	300					

The reader should be cautioned against overemphasizing the frequency and damping contrasts in the foregoing tables. For example, the listed differences in frequency for the first bending mode wing "A" are more probably due to errors than to the listed differences in wing root and other conditions (with cycle counting, for high damping, and oscillograph timing lines considered to be among the possible sources of error). For the same mode, the damping values of 1.4% and 1.0% with the wing root at 130°F and room temperature, respectively, are well within a measurement accuracy.

If the damping results for wings "B" and "BSP" are considered to be results before and after the wind-on test for essentially the same wing, then the 0.9% value for 1st torsion suggests a large change relative to the 2.3% value. It would be more reasonable, however, to regard both values as part of the scatter. The most reliable damping differences in the foregoing tables are those between the clamped and unclamped conditions in first bending (with the damping in the unclamped condition so high for wing "B" that 1st bending was not excited by the mallet).

The mode designations for wings "B" and "BSP" were based on a previous node-line determination for a different wing-root condition. For wing "A", however, the mode designations were based on measured mode shapes; and the "question mark" means that the mode labeled "1st torsion and second bending (?)" could not be excited in the mode-shape test.

For the mode shape measurement, 12 highly sensitive noncontacting capacitive probes (proximity deflection sensors) were developed by Dean Harrison of the Ames Research Center, Electronics Research Branch, and assembled in a mode shape frame as shown in figure 6. The probe outputs were calibrated by deflecting the wing statically and measuring the deflections opposite the probes with a dial gage. Mode shapes, as forced by an electrodynamic shaker, were then determined with wing "A" installed in the tunnel.

The mode shape results are presented for excitation at the leading edge of the wing tip in figure 7 and at the trailing edge in figure 8. The four lowest frequencies are presented in each case, and these represent the first five modes except for the unexcited mode mentioned earlier. Frequencies are somewhat different from those given earlier primarily because of the stiffness and inertia of the shaker moving parts. The RMS displacements in the modes are given in tables with the modal plots. These displacements are proportional to the length of the modal vectors, and the relative signs of the vectors correspond to the phase of the time histories in a simultaneous oscillograph display. Numerical locations of the 12 deflection points are given in figure 7(a) only.

The mode shapes were measured not only to identify mode shapes but also to serve as useful coordinates for possible future flutter analyses. The most important coordinate information, which is not obtainable from node-line studies, is the torsion present in the first bending modes of figures 7(a) and 8(a) and the bending present in the mostly torsion modes of figures 7(c) and 8(c). A suitable mean would have to be found between the modes of figures 7 and 8, of course, if the results were to be used for coordinates.

Test Procedure and Data Reduction

In the course of the test, the angle of attack ranged from 0° to 66° , the Mach number from 0.28 to 0.60, the dynamic pressure from 21 psf to 243 psf, and the Reynolds number per foot from $0.32 \times 10^6 \text{ ft}^{-1}$ to $3.66 \times 10^6 \text{ ft}^{-1}$. Boundary layer trips were located 2-1/4 inches from the leading edge on both sides of the wing and extended from the outer bolt-head fairing to the tip, as shown in figure 4.

The test procedures for each air-flow condition started with a slow (1 or 2 minute) rotation from 0° to 66° angle of attack. Then rapid rotations were made from 66° to 0° with time durations of 0.4, 0.6, and 0.9 seconds. Finally two minutes of random vibration data were taken at the fixed angle or angles of attack which gave the maximum wing strain gage response (generally in the stall region), and fixed angles of 0° , 2° , and roughly 66° were added in most cases. In some cases, more than one wing-root clamping condition was tried at the fixed angles of attack.

This procedure constituted a survey for flutter and large dynamic overload. In their absence, the survey was broadened by avoiding small steps in fixed angle of attack, Mach number, and dynamic pressure.

At the fixed angles of attack, digital equipment was used to record the mean static wing loads (indicated by the strain gages), the tunnel conditions, and the angle of attack. At the fixed angles and also during the wing rotations, magnetic tape was used to record the mean and vibratory strain gage outputs and the angle of attack.

The data reduction for dynamic overload consisted of putting the magnetic tape output onto oscillograph paper for both the fast and slow angle sweeps and making the appropriate measurements on the paper. For "near-flutter" (where the total damping is stable but the aerodynamic part is zero or unstable), the data were reduced by playing the magnetic tape output through a band pass filter into an autocorrelation computer (reference 4) for the two-minute segments of random vibration data at the fixed angles of attack. The autocorrelation computer measures the total damping for comparison with the still-air or structural damping.

The band-pass filter was required to isolate individual modes in the presence of many modes (see figure 9 for a sample unfiltered response spectrum). For maximum speed of data reduction, the filter was set with both the high and low pass at a single frequency; and this frequency was varied in a search for low total damping.

The single frequency setting has the advantage of fine filtering but the disadvantage of maximum filter effect on the measured damping. At one of the frequencies of interest, 148 HZ, the filters had a ζ value of approximately 8.5% of critical, and measured wing damping values in that neighborhood are obviously meaningless. As shown for a sample calibration in reference 5, however, the single frequency setting can give accurate damping measurements for low damping (less than 3% error for $\zeta = 0.2\%$ of critical). Unfortunately, the equipment required for the calibration technique of reference 5 was not available for the present test. Fortunately, the low damping values, particularly "near-flutter", are the values of greatest interest.

RESULTS AND DISCUSSION

Test Results

The bending strain gage signal in figure 10 is a typical time history during rapid wing rotation from 66° to 0° angle of attack (nominal angles), with (1) the dynamic load (at a particular angle) and (2) the stall and (3) the minimum in the load curve immediately after the stall. Results on these three quantities under various flow conditions are presented as functions of elapsed rotation time for wing "A" in figures 11 through 13 and for wings "B" and "BSP" in figures 14 through 16.

Results at fixed angle of attack, which comprise all of the quantitative results associated with flutter, are presented as functions of dynamic pressure for wing "A" in figures 17 through 21, for wing "B" in figures 22 and 23, and for wing "BSP" in figures 24 and 25. These results include total damping, root mean square bending oscillations, root mean square torsional oscillations, and the ratio of the two oscillations at various Mach numbers, frequencies, and fixed angles of attack.

Discussion of Results for Wing Rotation

The most important quantitative results for the space shuttle orbiter in the wing-rotation part of the test are the ratios (R_{DL}) of the maximum total load, including vibrations, to the maximum mean load for the rapid rotations from 66° to 0° angle of attack. A survey of figures 11 and 14 indicates, for the three wings tested, that the maximum R_{DL} for an elapsed rotation time of 0.6 seconds was 1.12. This rotation time is the most important of the three given since it is scaled from that for the full-scale vehicle (6 sec.).

For the slow rotations, requiring 60 to 100 seconds, the maximum R_{DL} in figures 11 and 14 was 1.11. This R_{DL} was caused by buffet at $\alpha = 66^\circ$ prior to rotation. Since the record time prior to slow rotation was less than 30 seconds,* it is possible that a longer record would give a higher R_{DL} . In fact, information in reference 3 suggests an R_{DL} of 1.17 for buffet of the space shuttle straight wing at $\alpha = 60^\circ$.

When the R_{DL} values of 1.11 and 1.17 prior to slow rotation (if any) are compared with the value of 1.12 for a rotation time of 0.6 seconds, it is apparent that the maximum total loads (including vibrations) caused by rapid rotation are no larger than those due to fixed-wing buffet. In fact, the maximum R_{DL} of 1.20 in figures 11 and 14 and a rotation time of 0.4 seconds is not much worse than 1.17, and the maximum of roughly 1.10 for 0.9 seconds is the smallest of the maximums.

The vibrations caused by rapid rotation are transient responses to the mechanical load changes at the beginning and end of rotation and to the aerodynamic load changes in the minimum in the load curve immediately after the stall and stall regions (figure 10). Buffet is superimposed at $\alpha = 66^\circ$ and possibly at some of the rapidly traversed angles.

*No attempt has been made to present the buffet information statistically. Records of 120 second duration were taken at $\alpha = 66^\circ$, but not for all cases.

All vibrations large enough to affect the load time histories significantly have a frequency near first bending, or approximately 30 cps. In many cases there were so few cycles in the neighborhood of the stall and the minimum in the load curve immediately after the stall that the vibrations could not be distinguished from the mean, with figure 10 being a marginal case in this regard. In some cases, particularly near $\alpha = 66^\circ$, the oscillatory loads could not be distinguished from the instrumentation noise (with figure 10 being marginal); and R_{DL} was listed as unity for these cases.

The reason that the ratios R_{DL} in figures 11 and 14 are so close to unity is simply that the largest vibrations tend to occur in the middle of the loading range specifically, in, or near, the normal force recovery between the minimum in the load curve immediately after the stall and the stall illustrated in figure 10. In this region, the ratio of the single amplitude incremental load to the mean load at $\alpha = 66^\circ$ is sometimes quite large, with the largest being 0.43. This ratio is not large enough, however, to produce loads higher than the mean load at $\alpha = 66^\circ$; and R_{DL} is always determined by the smaller oscillations at $\alpha = 66^\circ$.

Except for the lowest q_∞ in figure 11(a), there is a tendency in figure 11 for the highest values of R_{DL} due to rapid rotation to occur for the lowest values of q_∞ . A possible explanation for this tendency is that the oscillations at $\alpha = 66^\circ$ are relatively independent of q_∞ while the mean loads are proportional to q_∞ . Such independent oscillations might be caused by the mechanical load changes mentioned earlier.

No such parametric variation with q_∞ is apparent in the R_{DL} values for the torsionally stiffer wings "B" and "BSP" in figure 14, and those values are somewhat lower than the corresponding values for wing "A" in figure 11. The lower R_{DL} values may result simply from a smoother application of mechanical load by the hydraulic cylinder at the start of rapid rotation ($\alpha = 66^\circ$). Such variations could also occur on the full-scale vehicle due to the pilot or autopilot.

It is also apparent in figure 14 that the spoiler on wing "BSP" did not greatly affect the R_{DL} values. On the other hand, the ratio (not plotted) of the maximum vibration amplitude to the maximum mean load was lower by a factor ranging from two to three for wing "BSP" than for wing "B". This could result from the fact that the spoiler essentially removed the minimum in the load curve immediately after the stall in the mean load variation. (Note that for the double-flagged symbols, the values of R_D in figure 16 are very close to those of R_S in figure 15).

The ratios (R_S) of the mean load at stall to the maximum mean load and (R_D) of the mean load at the minimum in the load curve immediately after the stall to the maximum mean load are given in figures 12 and 13 for wing "A" and in figures 15 and 16 for wings "B" and "BSP". These ratios may be important if they occur at slightly different times on opposite wings of the space shuttle vehicle and thereby contribute large rolling moments. Some of the R_S data in figure 12 has been flagged to indicate that the stall angle was not reached during the most rapid part of the rotation. For the slow rotations, some R_S data was eliminated when there was a jump in strain gage readings at the stall. This jump may have been caused by a slight slippage between the wing and the tongue, and there was a zero change (but not a slope change) in the strain-gage calibrations before and after the tests.

It is important to realize that the present results are load results, i.e., normal force results, and not lift. The magnitudes of the maximum mean loads are defined by the C_N values given in figures 11 through 16. These are derived from the strain gage outputs, calibrated to give bending moment, under the assumption that the wing center of pressure lies on the mean aerodynamic chord, as illustrated in figure 1.

The ranges of Mach number and dynamic pressure given in figures 11 through 16 result from variable blockage as the wing rotates from $\alpha = 66^\circ$ to $\alpha = 0^\circ$. The time lag in arriving at the final tunnel conditions for $\alpha = 0^\circ$ is unknown, but it is reasonable to assume that the tunnel conditions for $\alpha = 66^\circ$ apply throughout the rapid rotations.

The results discussed so far pertain to the maximum total loads (including vibrations) caused by rapid rotation. Stall flutter, on the other hand, would tend to be inhibited by rapid, as opposed to slow, rotation. During the slow rotations referred to earlier, there was no visible flutter of any kind, that is, no visible steady or growing oscillations (to indicate zero or unstable total damping).

For a sound speed, a_∞ , of 1050 ft/sec, for a semi-chord, b , of 0.55 ft at the 3/4 semispan, and for a circular frequency, ω_α , of 836 rad/sec (the highest frequency involving 1st torsion of wing "A"), the stall flutter parameter, $\frac{\omega_\alpha b}{a_\infty}$, is 0.44. For wings "B" and "BSP", ω_α is 868 rad/sec, and

$\frac{\omega_\alpha b}{a_\infty}$ is 0.45.

Both of these $\frac{\omega_\alpha b}{a_\infty}$ values are lower than the value of 0.48 for which stall flutter occurred for the straight space shuttle wing model of reference 2. Hence, wings "A", "B", and "BSP" should have exhibited stall flutter for consistency with reference 2. By the same token, wing model one of reference 1 should have had stall flutter at the higher subsonic speeds ($0.6 = M = 1.0$). The reason for this inconsistency may be Reynolds number effects associated with the fact that the model of reference 2 is only one-third the size of the present models and has no boundary layer trip. On the other hand, flutter is often such a delicate balance of small damping forces that the inconsistency may be only an apparent one, particularly in view of the "near flutter" results to be discussed next.

Discussion of Results for Fixed Angles of Attack

The autocorrelation computer was used for measuring total damping to determine "near flutter". This could be done only at fixed angles of attack since the computer requires a stationary random data sample. The fixed angles selected were those which yielded the maximum response in torsion and bending, together with 0° , 2° , and 66° in most cases.

"Near flutter" is defined herein as occurring when the total damping is stable but the aerodynamic part is zero or unstable. The total damping is the aerodynamic part plus the structural (or still-air) part. Due to accuracy limitations in the damping data, "near flutter" is considered to be established only when the total damping is less than half of the lowest applicable value of the still-air damping, to be probable between the half value and the full value, and to be possible between the full value and twice the full value.

Where applicable still-air values are given in figures 17 through 25, they are taken from the tables in the section on "Frequencies, Damping Values, and Mode Shapes in Still Air". Where applicable values are not available for figures 17 through 25, the value of $\zeta = 0.01$ is used for the criteria just stated. The still-air ζ values are not adjusted for frequency differences between still-air and wind-on conditions because those differences may be measurement errors.

For wing "A", on the basis of the present criteria, "near flutter" is established at $M = 0.28$ with $\alpha = 64^\circ$ in figure 17(a), at $M = 0.30$ with $\alpha = 2^\circ$ in figures 18(a) and 18(b), and at $M = 0.45$ with $\alpha = 2^\circ$ in figures 20(a) and 20(b). For wings "B" and "BSP", "near flutter" is not established.

The complete results for the criteria are presented for wing "A" in the following table:

<u>M</u>	<u>Degrees α</u>	<u>HZ f</u>	<u>Mode Description</u>	<u>Hydraulic Pressure</u>	<u>Wing Root</u>	<u>Strain Gage Type</u>	<u>Figure</u>	<u>"Near Flutter"</u>
0.28	64	174	3rd Bending and 2nd Torsion	Off	Clamped	Bending	17(a)	Estab.
0.28	64	174	"	Off	Clamped	Torsion	17(b)	Probable
0.28	48	174	"	Off	Clamped	Torsion	17(b)	Probable
0.28	64	34	1st Bending	Off	Clamped	Bending	17(c)	Absent
0.28	48	34	"	Off	Clamped	Bending	17(c)	Possible
0.30	+2	174	3rd Bending and 2nd Torsion	Off	Clamped	Bending	18(a)	Estab.
0.30	2	174	"	Off	Clamped	Torsion	18(b)	Estab.
0.30	2	90	1st Torsion and 2nd Bending	Off	Clamped	Bending	18(a)	Possible
0.30	18	98	"	Off	Clamped	Bending	18(a)	Probable
0.30	20	174	3rd Bending and 2nd Torsion	Off	Clamped	Torsion	18(b)	Possible
0.30	2,14,18	34	1st Bending	Off	Clamped	Bending	18(c)	Absent
0.40	64	133	1st Torsion and 3rd Bending	Off	Clamped	Bending	19(a)	Possible
0.40	64	133	"	Off	Clamped	Torsion	19(b)	Possible
0.40	64	34	1st Bending	Off	Clamped	Bending	19(c)	Absent
0.45	2	133	1st Torsion and 3rd Bending	Off	Clamped	Bending	20(a)	Estab.
0.45	2	133	"	Off	Clamped	Torsion	20(b)	Estab.
0.45	13.5	133	"	Off	Clamped	Bending	20(a)	Absent
0.45	13.5	133	"	Off	Clamped	Torsion	20(b)	Absent
0.45	18	133	"	Off On	Clamped Unclamped	Torsion	20(b)	Absent
0.45	2	34	1st Bending	Off	Clamped	Bending	20(c)	Absent
0.60	0	182	3rd Bending and 2nd Torsion	On	Unclamped	Bending	21(a)	Possible
0.60	0	182	"	On	Unclamped	Torsion	21(b)	Probable
0.60	13	133	1st Torsion and 3rd Bending	Off On	Clamped Unclamped	Bending	21(a)	Probable
0.60	19	83	2nd Bending	Off	Clamped	Bending	21(a)	Possible
0.60	0, 25	121-129	1st Torsion and 3rd Bending	On	Unclamped	Torsion	21(b)	Absent
0.60	0, 25	34	1st Bending	On	Unclamped	Bending	21(c)	Probable

For Wing "B" the following table applies:

<u>M</u>	<u>Degrees α</u>	<u>HZ f</u>	<u>Mode Description</u>	<u>Hydraulic Pressure</u>	<u>Wing Root</u>	<u>Strain Gage Type</u>	<u>Figure</u>	<u>"Near Flutter"</u>
0.30	12,14,16	148	1st Torsion	On	Clamped	Bending	22(a)	Possible
0.30	14	148	"	On	Unclamped	Bending	22(a)	Possible
0.30	12	180-186	3rd Bending	On	Clamped	Torsion	22(b)	Probable
0.30	13,14,16	180-186	"	On	Clamped	Torsion	22(b)	Possible
0.45	13	148	1st Torsion	On	Clamped	Bending	23(a)	Possible
0.45	14	148	1st Torsion	On	Unclamped	Bending	23(a)	Possible
0.45	10,12	175-182	3rd Bending	On	Clamped	Torsion	23(b)	Possible
0.45	14	175-182	"	On	Unclamped	Torsion	23(b)	Possible

And for wing "BSP"

0.29	25	175	3rd Bending	On	Clamped	Torsion	24	Probable
0.29	28	175	3rd Bending	On	Clamped	Torsion	24	Possible
0.45	29,31	175	3rd Bending	On	Clamped	Torsion	25	Probable

With reference once again to flutter in the stall-angle region (stall flutter), the preceding table for wing "A" indicates probable "near flutter" at $M = 0.30$ with $\alpha = 18^\circ$ in figure 18(a) and at $M = 0.60$ with $\alpha = 13^\circ$ in figure 21(a). The table for wing "B" shows probable "near flutter" at $M = 0.30$ with $\alpha = 12^\circ$ in figure 22(b) while that for wing "BSP" shows the same at $M = 0.29$ with $\alpha = 25^\circ$ in figure 24 and at $M = 0.45$ with $\alpha = 29^\circ$ and 31° in figure 25. (The frequency for wings "B" and "BSP" is described as third bending but may contain some of the torsion usually associated with stall flutter.) Since there is a probable "near flutter" in the stall-angle region, it is possible that a reduction in structural damping by, say, a factor of two would produce actual stall flutter. Thus, the inconsistency between the present results and the observed stall flutter of reference 2 may well be only apparent.

It should be noted that the preceding tables do not contain the observed variations of damping with dynamic pressure, q_∞ . (Note that q_∞ is directly proportional to the square of the commonly used flutter parameter $\frac{GJ}{b\omega_\alpha \sqrt{\mu}} V$, where GJ is the root torsional stiffness and V is the flow velocity.). The "near flutter" criterion in the tables is based on the lowest damping in the q_∞ variations. The variations can be seen in figures 17 through 25, and the only comment to be made at present is that figure 17(a) indicates the possibility of a sharp dip in damping at $q_\infty = 85$ psf.

Figures 17 through 25 also contain variations with q_∞ of the root mean square oscillations, both bending, h , and torsion, θ , and also their ratio. It should be noted that, except for 1st bending, the frequencies specified on the figures were those filter settings which gave the lowest damping values on the correlator, and do not restrict the frequency content of the oscillations.

The damping values read on the torsion and bending gages in figures 17 through 25 should be the same since spatial filtering should not affect decays which are frequency filtered. The damping differences noted between the (a-) and (b) figures probably result from differences in signal level at the frequencies of low damping, plus the fact that the filters affect the damping measurements least for the lowest measured damping levels.

Standard deviations have been calculated for two of the damping values by dividing the random data into five segments. For the point in figure 20(a) having a mean ζ of 0.003, the standard deviation is 0.001; and for the point in figure 17(c) with a mean ζ of 0.012, the standard deviation is 0.002.

Some mention should also be made of the possibility that the measured damping values may be affected by wind tunnel resonance, the organ-pipe effect from wall to wall across the stream. Since resonant frequencies across a circular section are not known, it would be desirable to repeat the test in a different wind tunnel.

Effect of Root Fixity on Flutter and Overload Results

The still-air damping values, ζ , tabulated in an earlier section cover a range from 1.0% to 2.6% of critical for all vibration modes with the wing root clamped and essentially the same range (0.9% to 2.8% of critical) for all modes but first bending with the wing root unclamped. These damping levels resulted from bearing slop in the wing rotation mechanism, and even the lowest values are enough higher than the damping for most wind tunnel models to cause occasional differences in flutter results. These lowest values, however, are typical values for a full scale vehicle; and, fortunately, the lowest values are the most believable of the present measurements.

With the wing root clamped, there was no established, or even probable, "near flutter" in first bending at fixed angles of attack. In the higher frequency modes, there was no substantial total damping difference in figures 17 through 25 due to clamping and unclamping the wing root; and the clamping insensitivity of the still-air damping has already been noted. With the most likely still-air damping values being typical for full scale, then, it would seem that the (necessarily unclamped) rotation test is reasonably representative as to flutter.

In the overload results of the rotation test, however, the predominant frequency was first bending. For this mode, unclamping the wing raised the still-air damping from 2.1% to 4.1% of critical with wing "A" and from 1.9% to 6.7% of critical for wings "B" and "BSP" (the latter two wings being considered identical in still-air damping). Thus, if the aerodynamic damping additions are relatively small, the damping in the critical first bending mode will be unrealistically high during wing rotation.

Fortunately, however, damping values around 6.7% of critical do not significantly change the magnitude of an undamped vibratory response to rapid wing rotation. Undamped vibrations would persist longer, of course, (namely, forever), but the decreasing mean load during rotation would leave the R_{DL} ratios unaffected (with R_{DL} being the ratio of maximum total load, including vibrations, to maximum mean load).

CONCLUDING REMARKS

A rotation loading and flutter test has been conducted in the Ames 12-foot Pressure Wind Tunnel at Mach numbers from 0.28 to 0.60 for a semispan model space shuttle wing (straight, aspect ratio 7, semispan 5 ft) and two variations from that wing.

The following conclusions are based on the part of the test in which the wing was rotated rapidly from 66° to 0° angle of attack and also rotated slowly between the two angles:

- (1) At an elapsed rotation time of 0.6 seconds, scaled from the full scale vehicle, the maximum total load (including vibrations) is only 12% higher than the maximum mean load for the basic wing. This is not much worse than the (non-statistical) buffet overload figure of 11% at $\alpha = 66^\circ$ in the present report and is better than the 17% for buffet in reference 3.

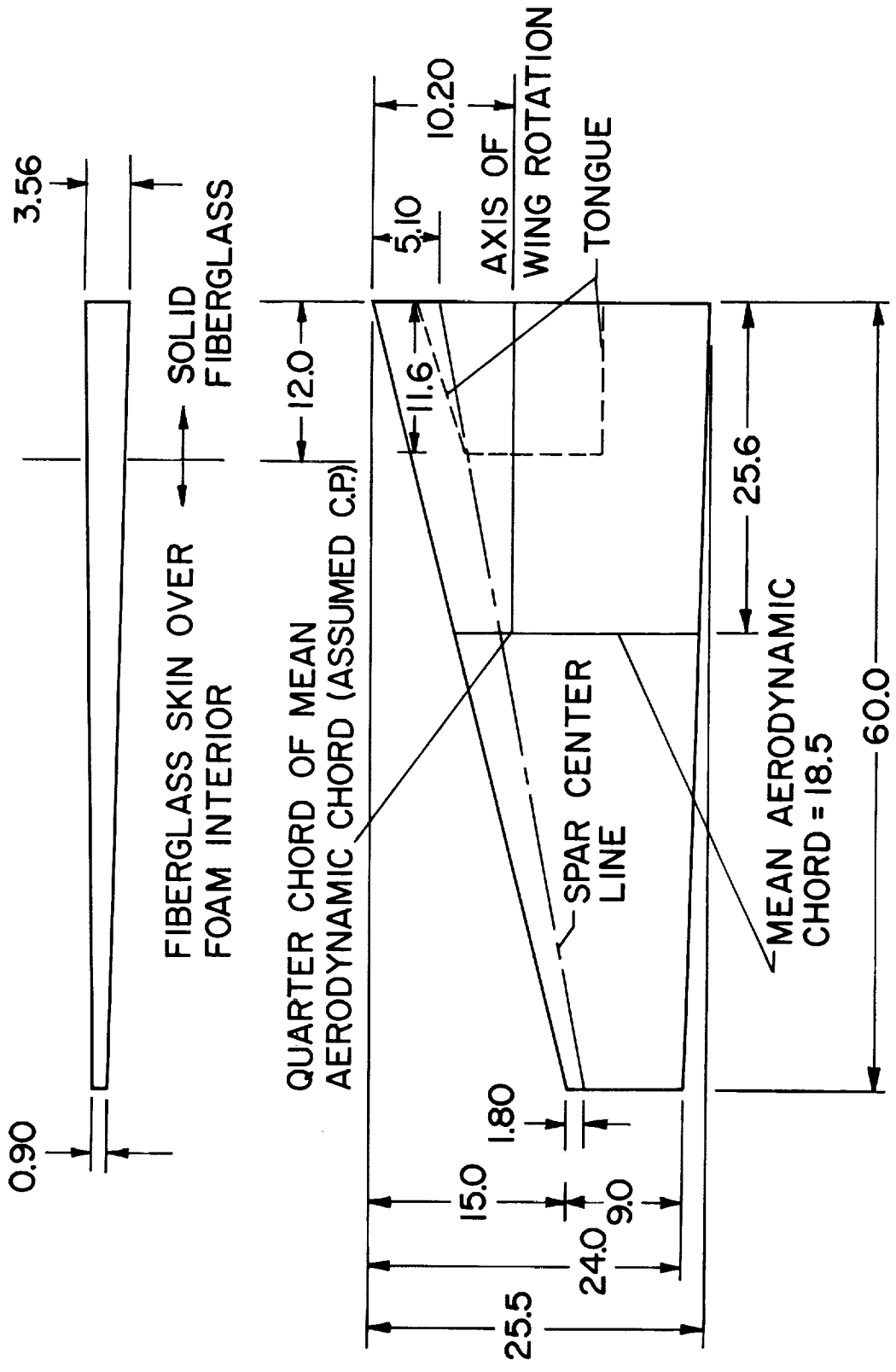
- (2) For a rotation time of 0.4 seconds, the above overload figure increases to 20%.
- (3) For a wing stiffer in torsion, the 12% overload figure decreases somewhat; and no further change is caused by the addition of a leading-edge spoiler.
- (4) There was no visible flutter (steady or growing oscillations) during the slow rotations between $\alpha = 66^\circ$ and $\alpha = 0^\circ$ for any of the wings.

The following conclusions are based on the part of the test in which total damping was measured from random samples at the fixed angles of maximum response, generally supplemented with $\alpha = 0^\circ$, $\alpha = 2^\circ$, and $\alpha = 66^\circ$:

- (1) "Near flutter" (stable total damping but zero or unstable aerodynamic damping) is established at $M = 0.28$ with $\alpha = 64^\circ$, at $M = 0.30$ with $\alpha = 2^\circ$, and at $M = 0.45$ with $\alpha = 2^\circ$ for the basic wing.
- (2) For the torsionally stiffer wing, "near flutter" is not established, with or without a leading-edge spoiler.

REFERENCES

1. Erickson, Larry L., Gambucci, Bruno, J., and Wilcox, Phillip R.: Effects of Space Shuttle Configuration on Wing Buffet and Flutter Part II - Thick High Aspect-Ratio Wing. NASA Space Shuttle Technology Conference. Volume III - Dynamic and Aeroelasticity. NASA TM X-2274, April, 1971, pp. 201-229.
2. Goetz, Robert C.: Lifting and Control Surface Flutter. Space Transportation System Technology Symposium. Volume II - Dynamics and Aeroelasticity. NASA TM X-52876, July, 1970, pp. 177-198.
3. Runyan, Harry L. and Reed, Wilmer, H., III: Shuttle: Dynamics and Aeroelasticity - An Appraisal. Aeronautics and Astronautics, Vol. 9, February, 1971, pp. 48-57.
4. Cole, Henry A., Jr.: On-the-Line Analysis of Random Vibrations. AIAA Paper No. 68-288, AIAA/ASME 9th Structures, Structural Dynamics and Materials Conference, April 1-3, 1968.
5. Warner, Robert W., and Wilcox, Phillip R.: Hypersonic and Transonic Buzz Measurements on the Lower Pitch Flap of the M2-F2 Lifting Entry Configuration. Proposed NASA TN, 1971.



ALL DIMENSIONS IN INCHES.

Figure 1.- Overall model wing geometry for all wings (materials and spar location for wing "A").

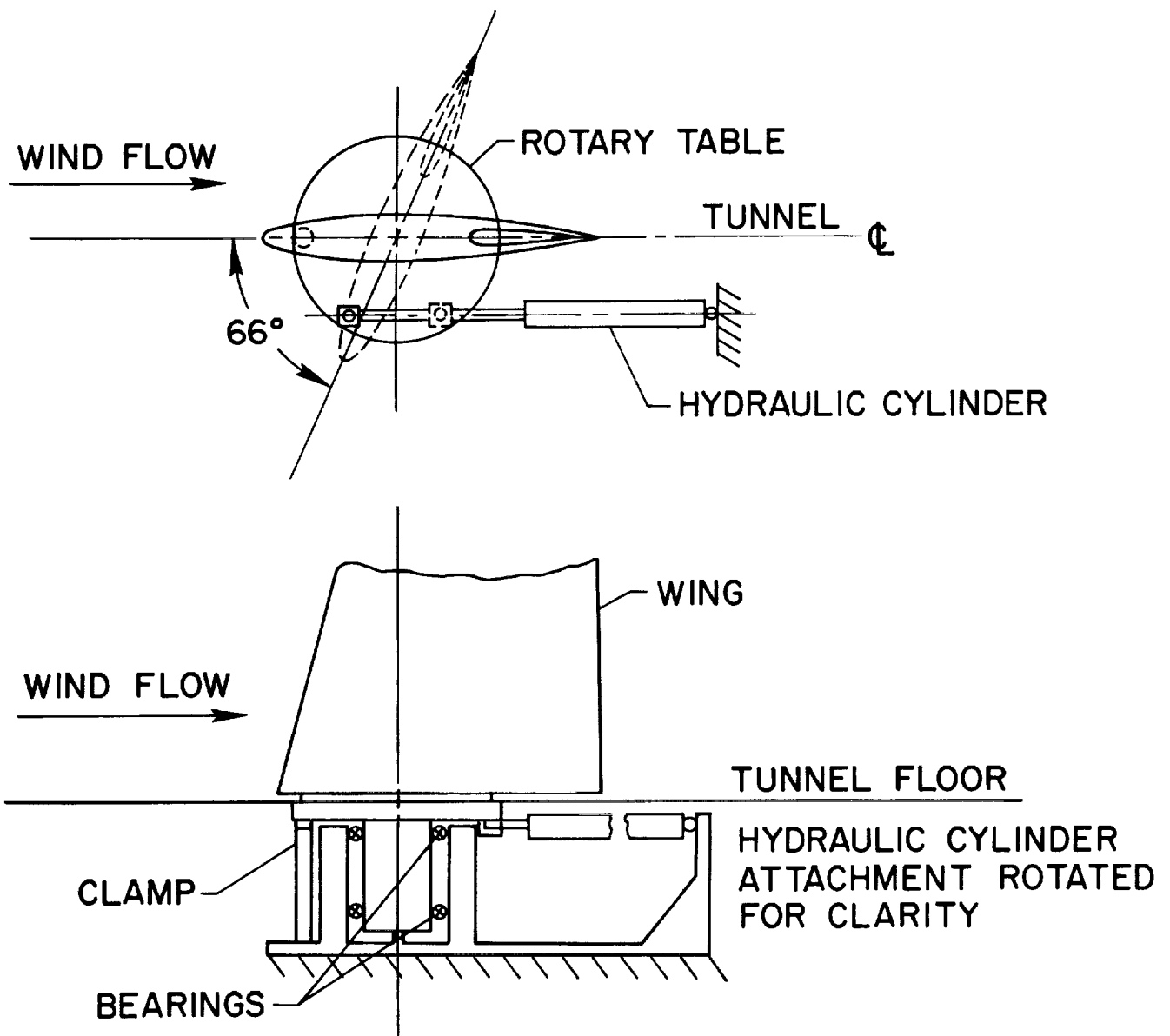
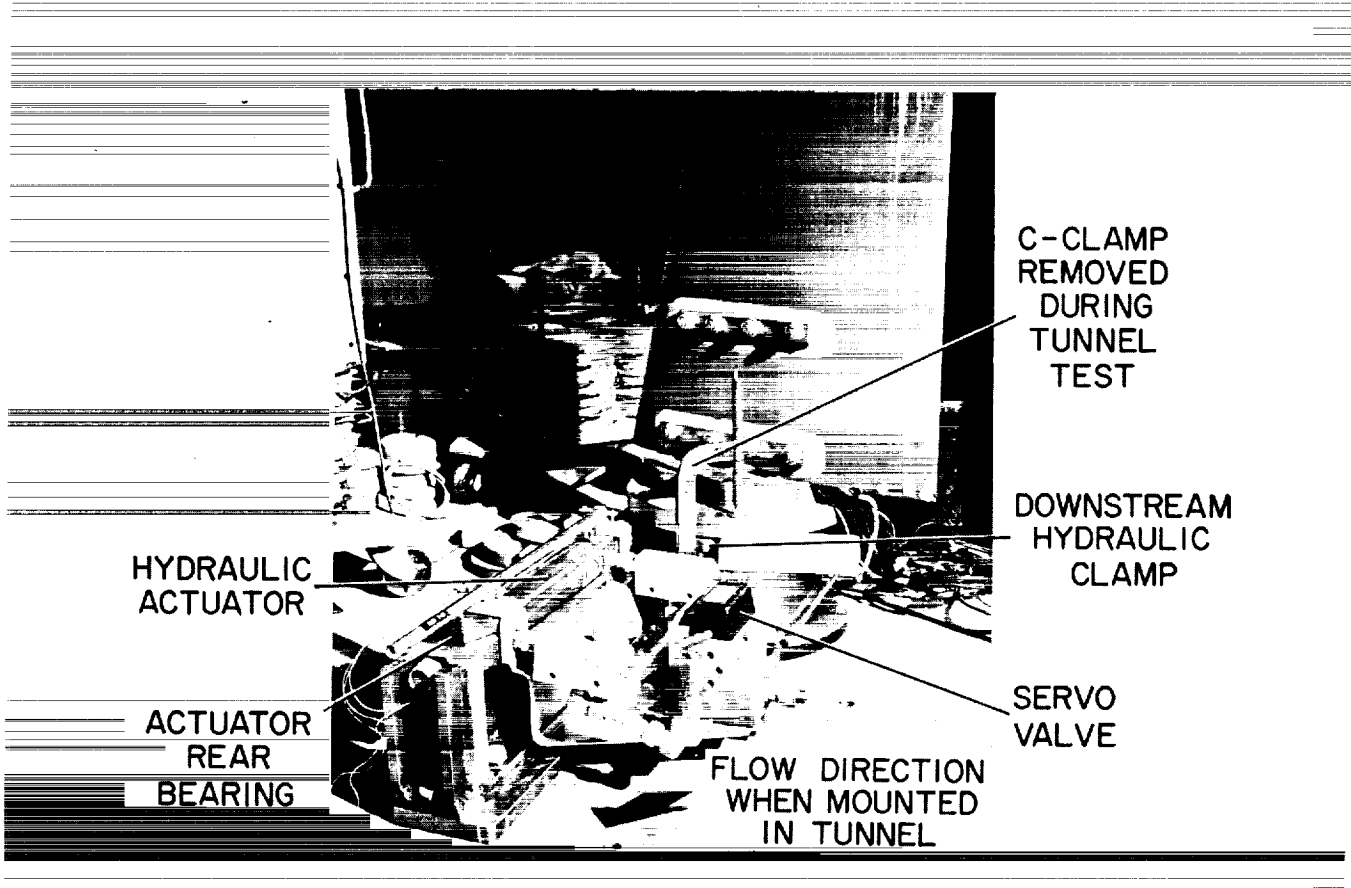


Figure 2.- Schematic of rotation mechanism.

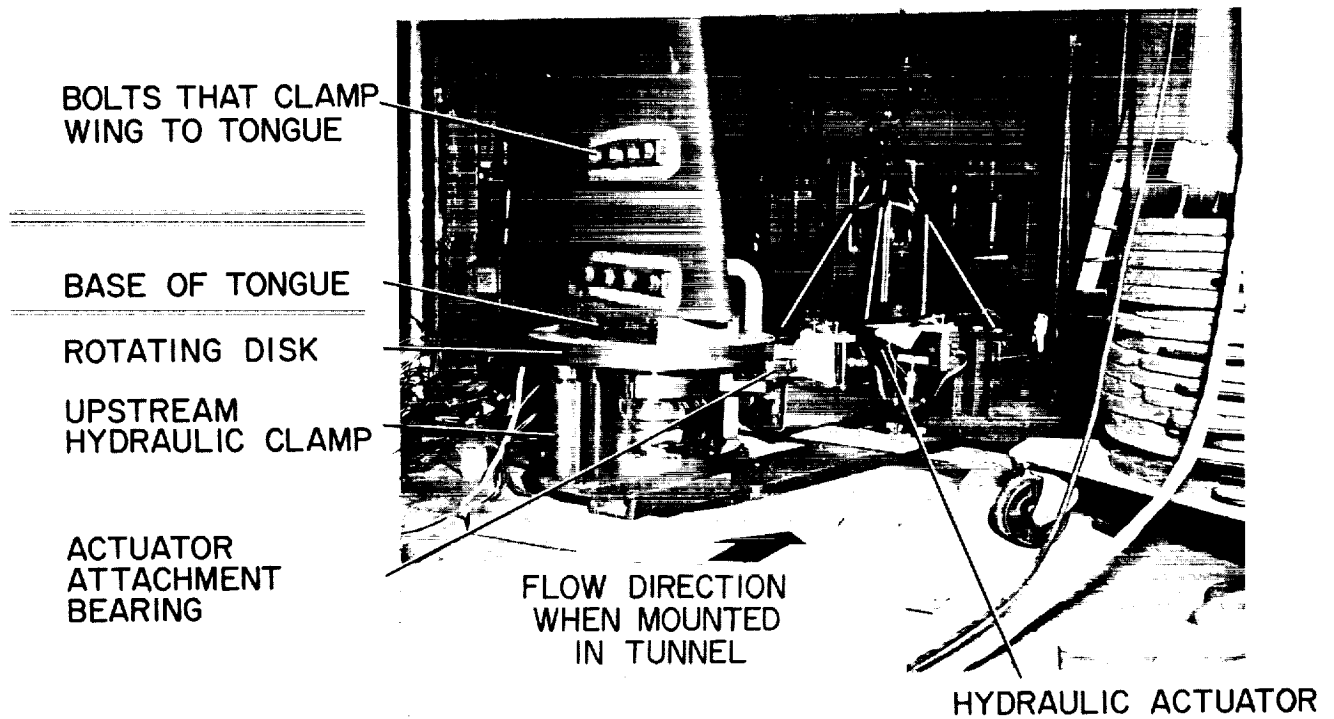
VIEW FROM DOWNSTREAM



(a) View from downstream.

Figure 3.- Photographs of rotation mechanism with wing at 66° angle of attack.

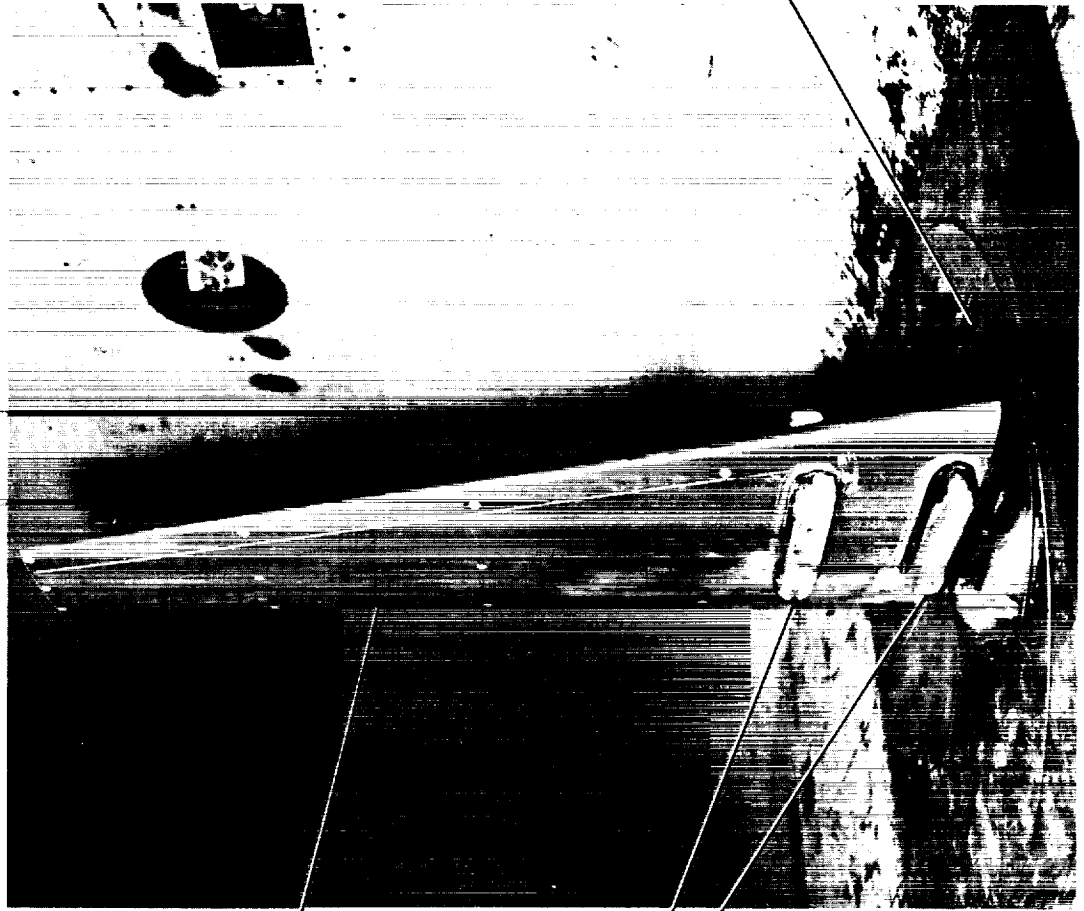
VIEW FROM UPSTREAM



(b) View from upstream.

Figure 3.- Concluded.

WING INSTALLED IN AMES 12 ft PRESSURE WIND TUNNEL



BOUNDARY
LAYER TRIP

FAIRINGS
FOR
BOLT HEADS

ROTATING
BASE FAIRING

Figure 4.- Wing installed in Ames 12-foot pressure wind tunnel.

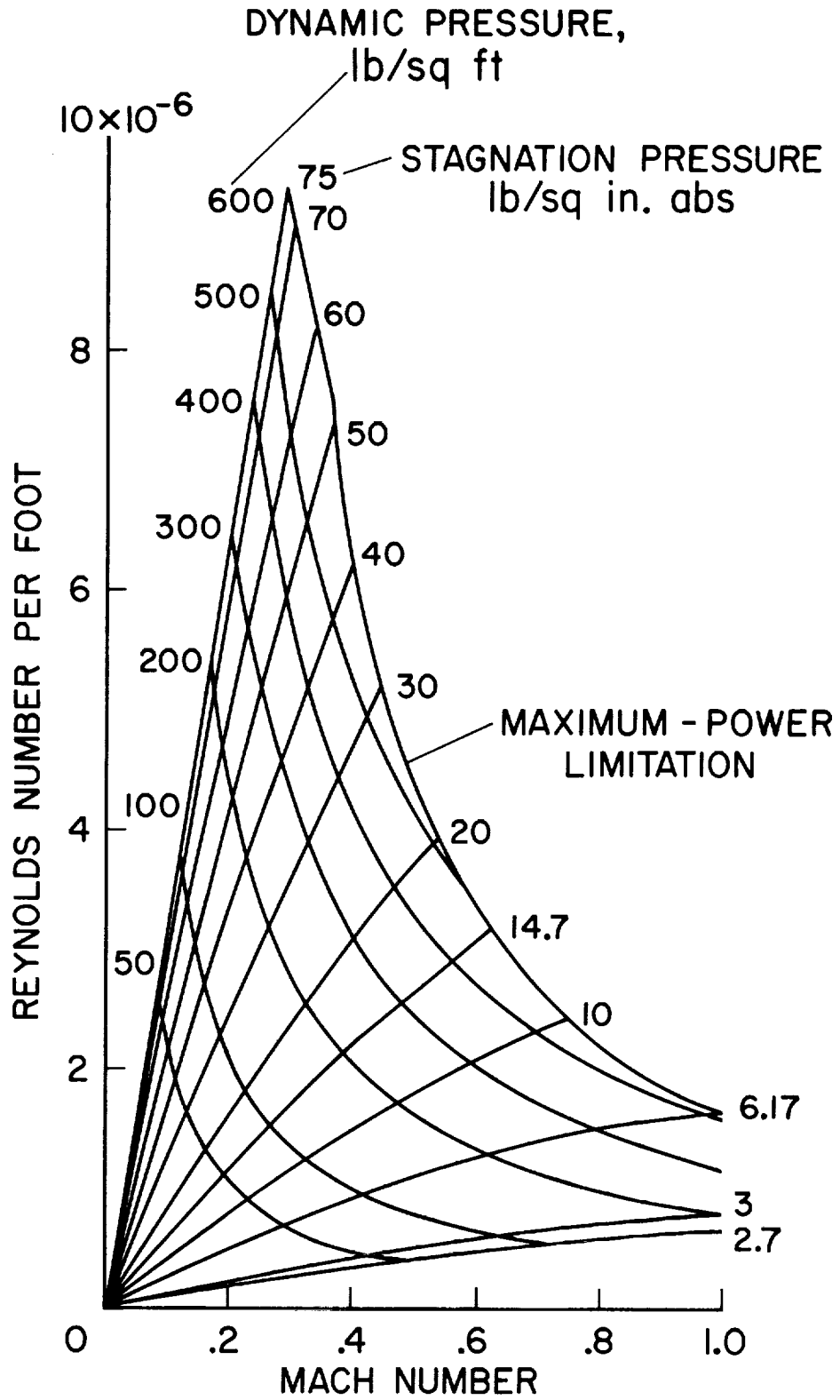
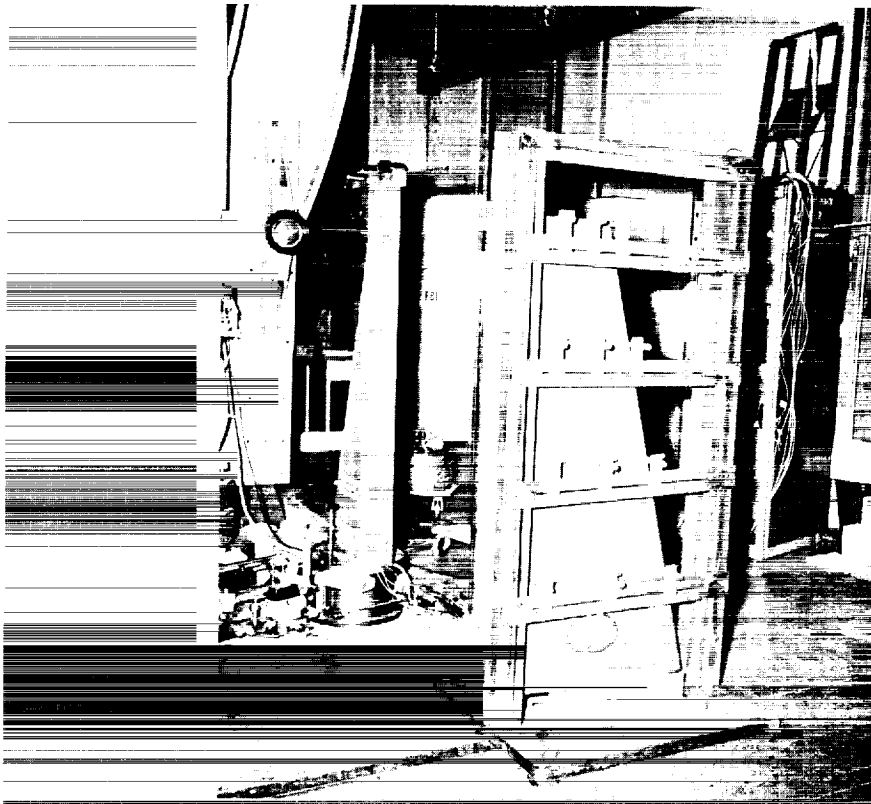


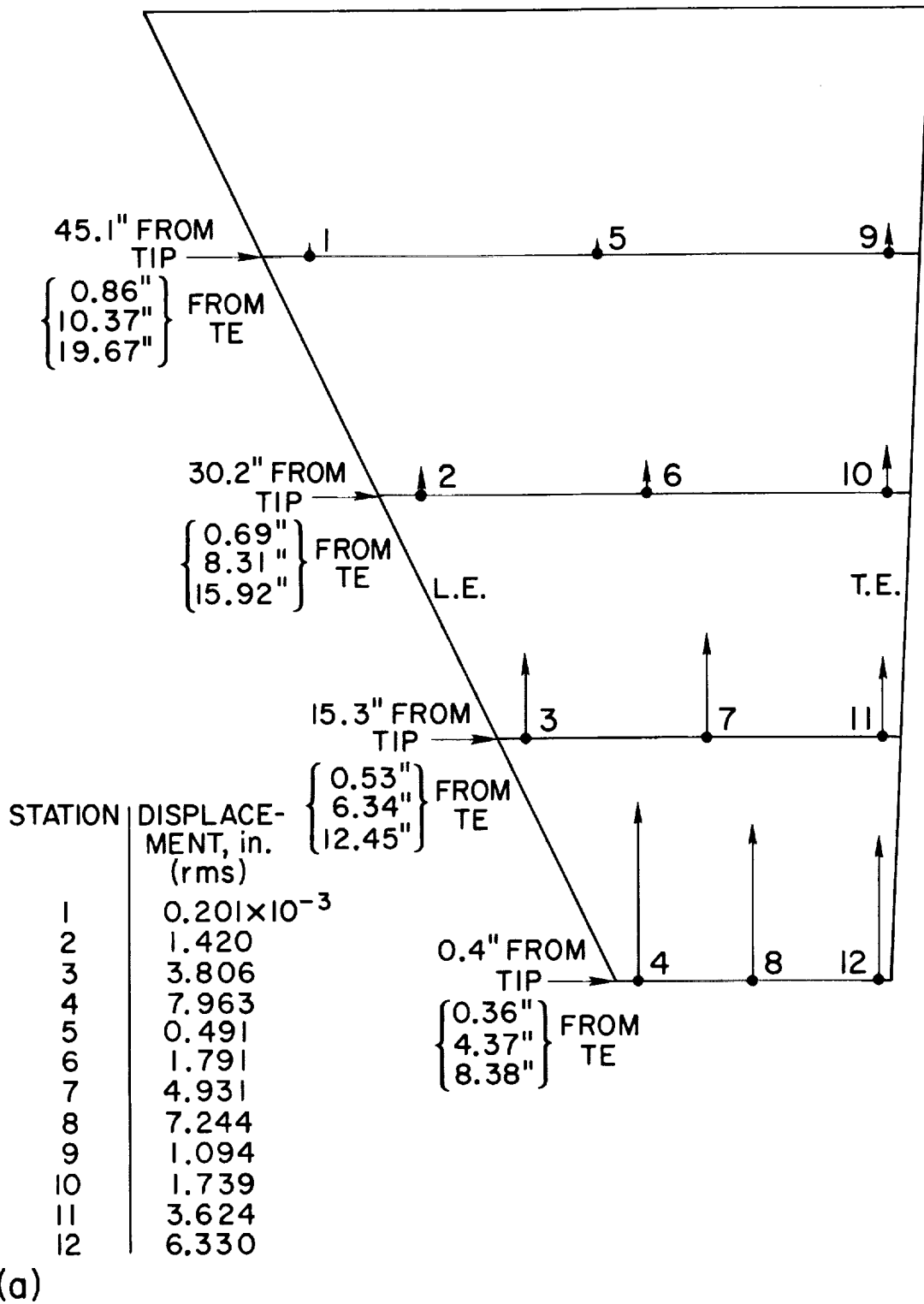
Figure 5.- Operating characteristics of the Ames 12-foot pressure wing tunnel.

MODE SHAPE FRAME WITH WING ON DUMMY MOUNT



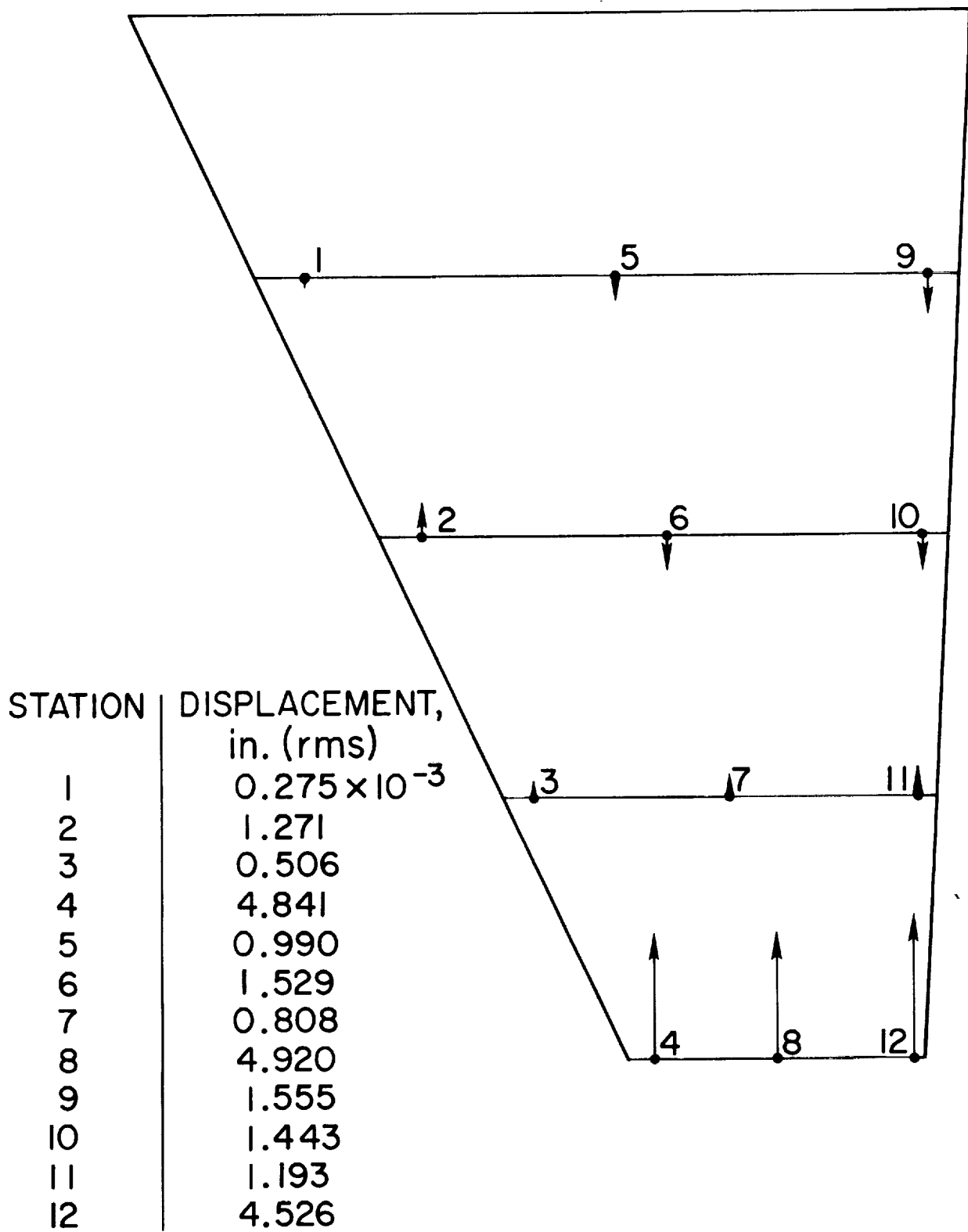
MODE
SHAPE
TRANSDUCER

Figure 6.- Mode shape frame with wing on dummy mount.



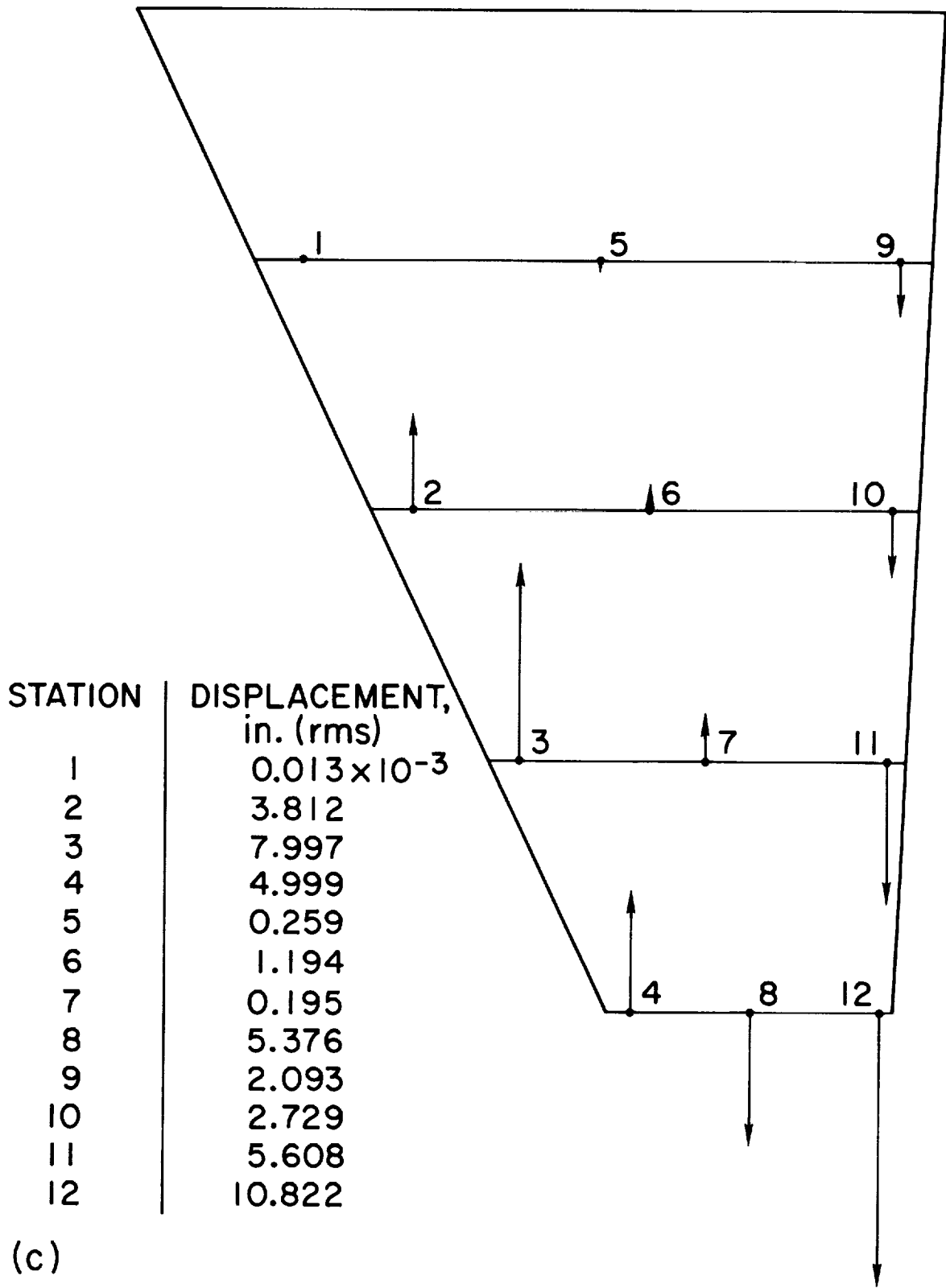
(a) 1st bending, $f = 42.5$ Hz.

Figure 7.- Mode shapes for wing "A" at $\alpha = 15^\circ$ with shaking at leading edge of wing tip (Station 4).



(b) 2nd bending, $f = 85.7$ Hz.

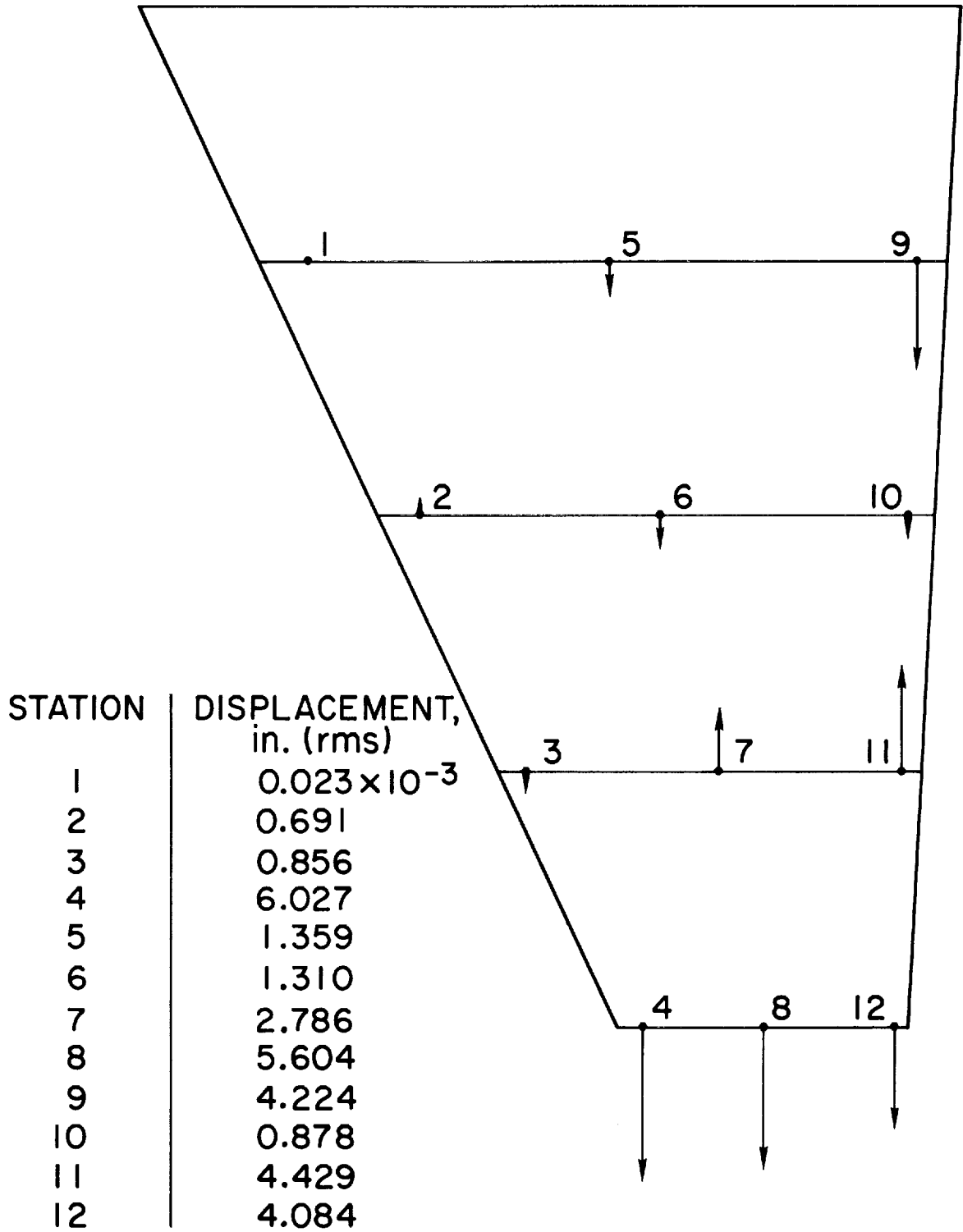
Figure 7.- Continued.



(c)

(c) 1st torsion and 3rd bending, $f = 141.7$ Hz.

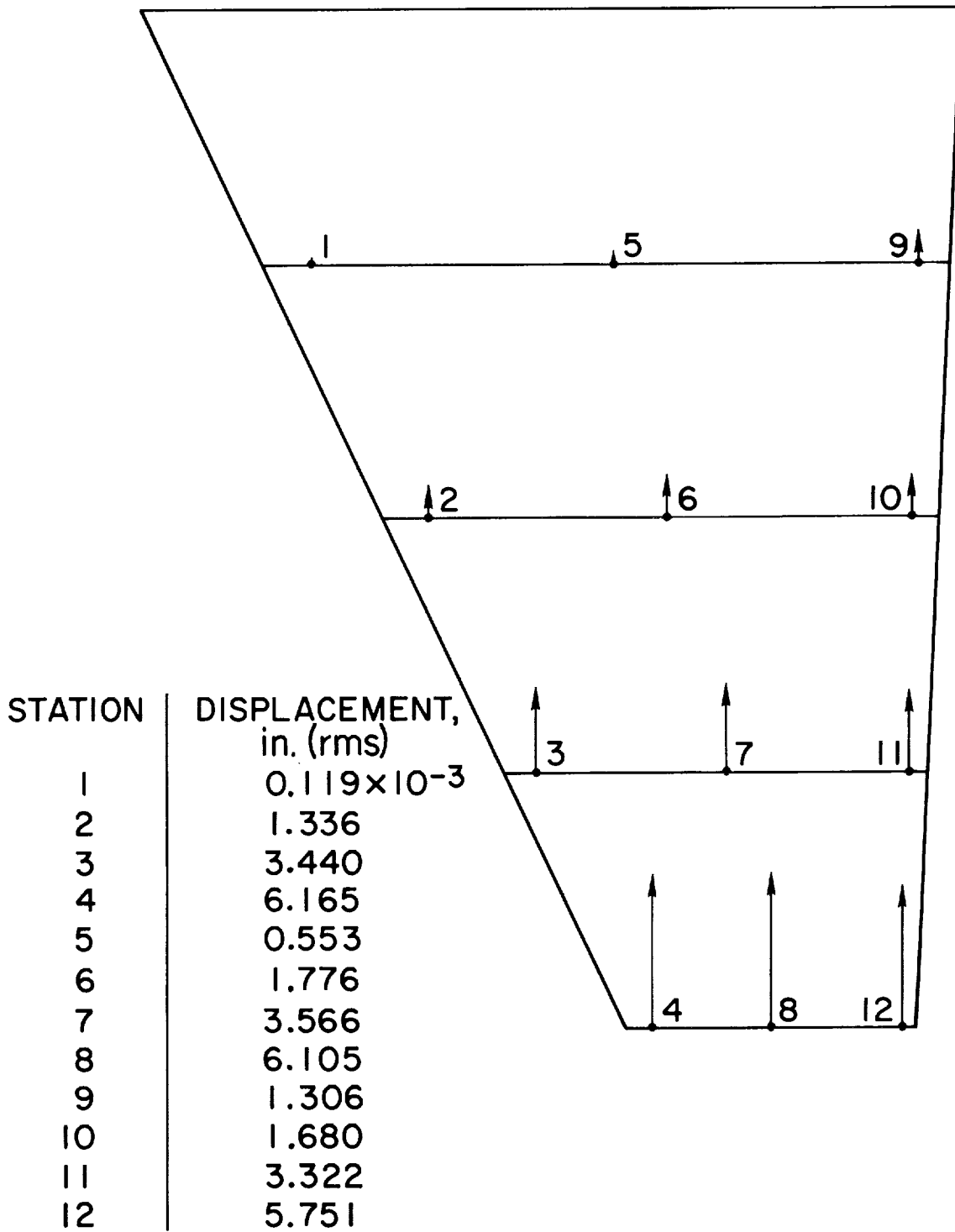
Figure 7.- Continued.



(d)

(d) 3rd bending and 2nd torsion, $f = 178.6$ Hz.

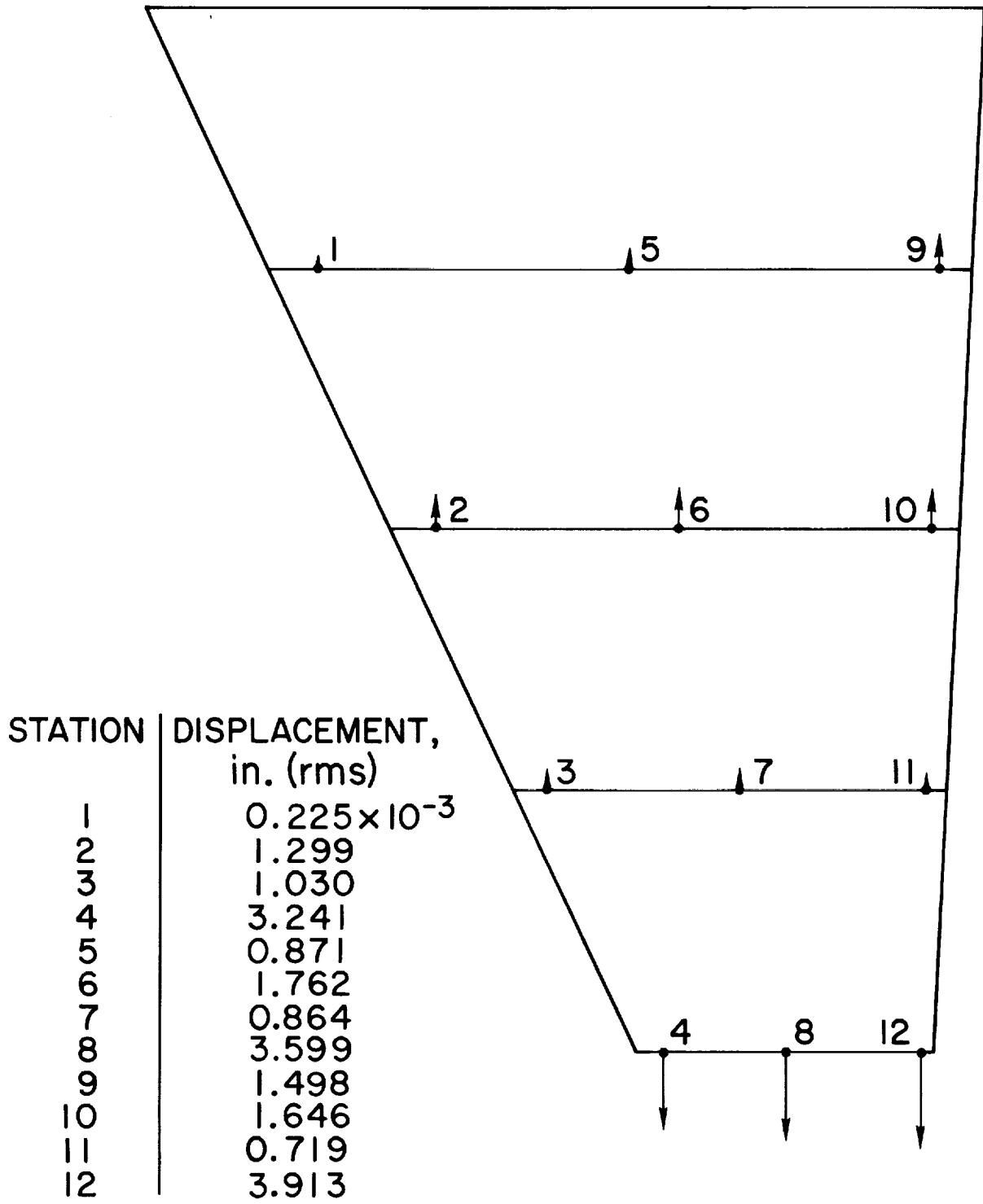
Figure 7.- Concluded.



(a)

(a) 1st bending, $f = 39.5$ Hz.

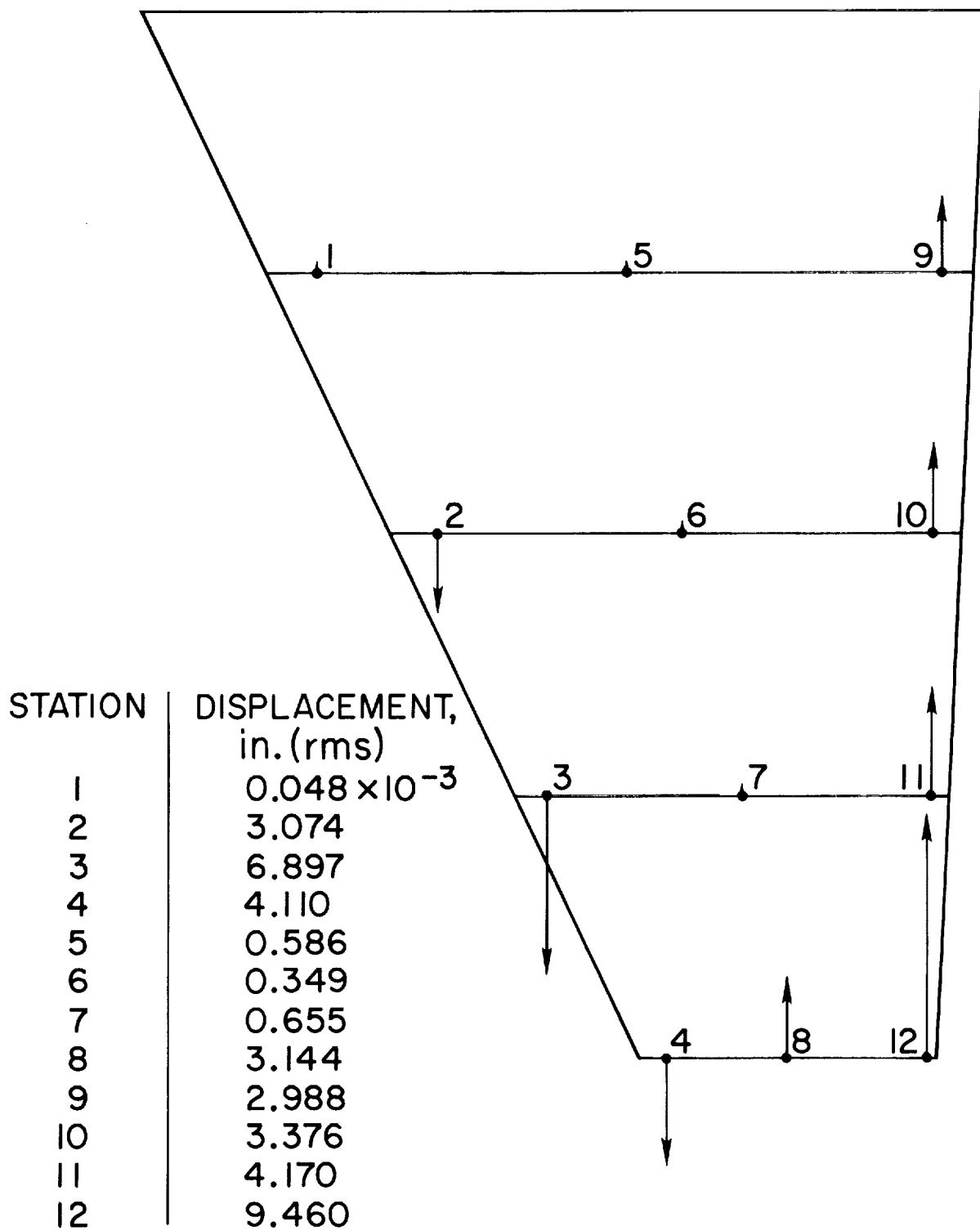
Figure 8.- Mode shapes for wing "A" at $\alpha = 15^\circ$ with shaking at trailing edge of wing tip (Station 12).



(b)

(b) 2nd bending, $f = 81.8$ Hz.

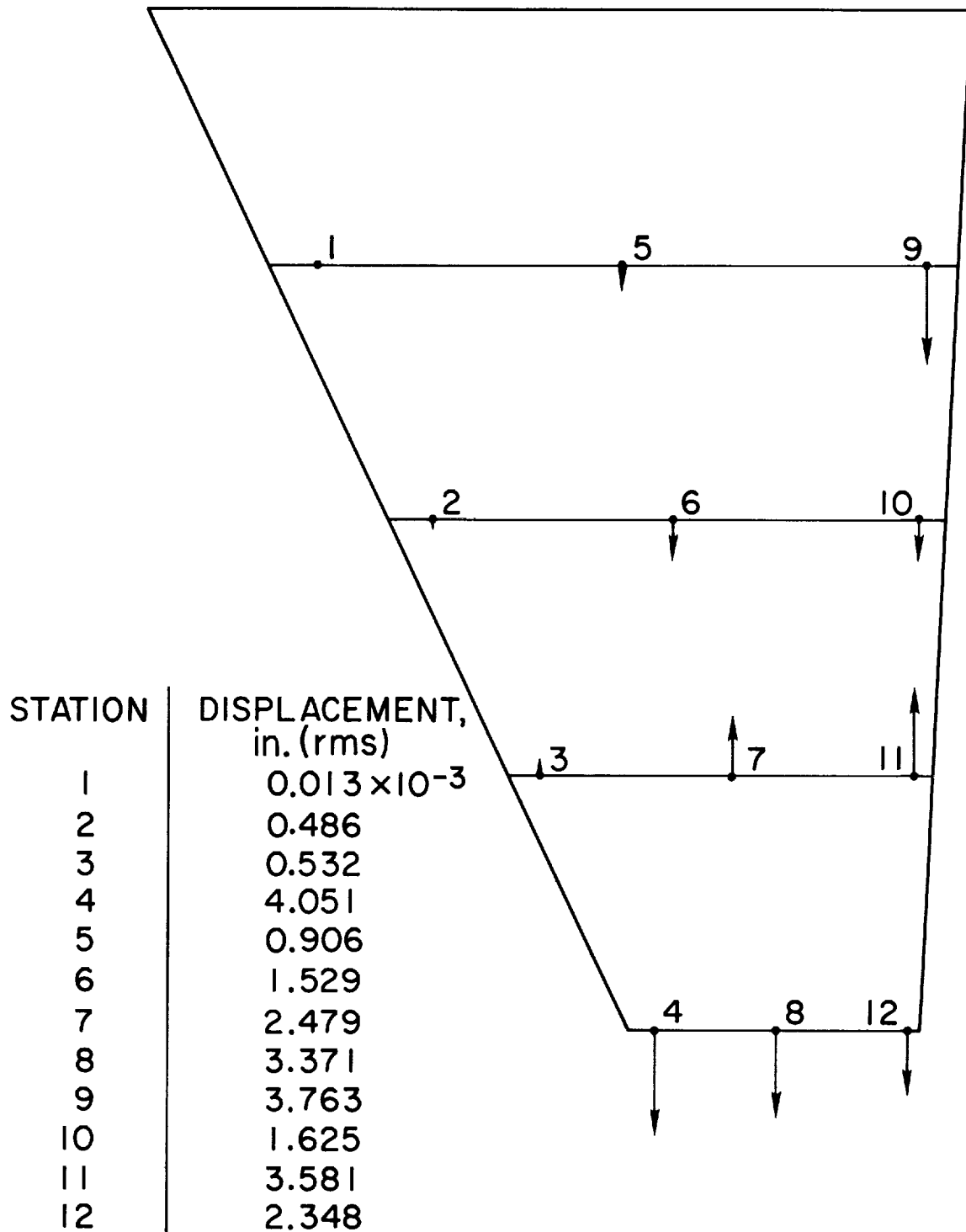
Figure 8.- Continued.



(c)

(c) 1st torsion and 3rd bending, $f = 140$ Hz.

Figure 8.- Continued.



(d)

(d) 3rd bending and 2nd torsion, $f = 170$ Hz.

Figure 8.- Concluded.

UNFILTERED RESPONSE SPECTRA FOR WING "A"
 $M = 0.45$ $\alpha = 2^\circ$ $q_\infty = 146.8 \text{ psf}$

1st
BENDING
34.5Hz

1st
TORSION
133Hz

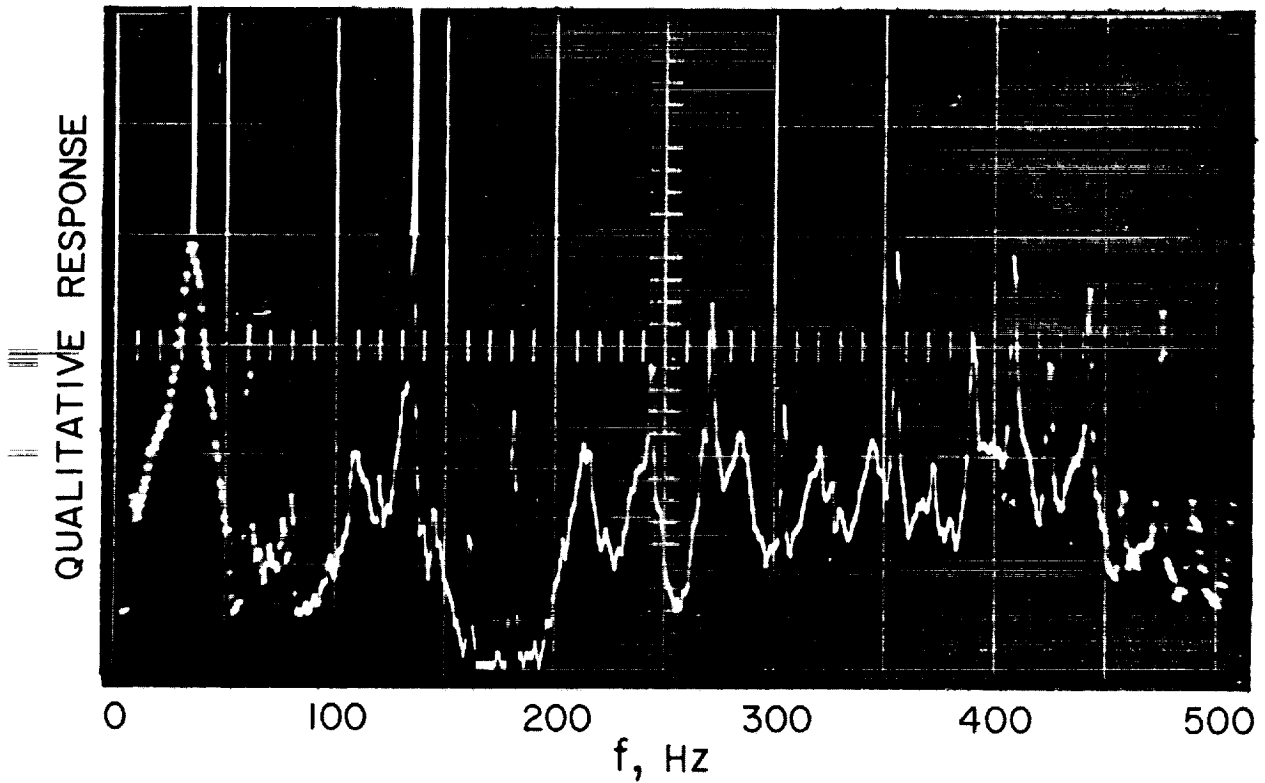


Figure 9.- Unfiltered response spectra for wing "A", $M = .45$, $\alpha = 2^\circ$,
 $q_\infty = 146.8 \text{ psf}$.

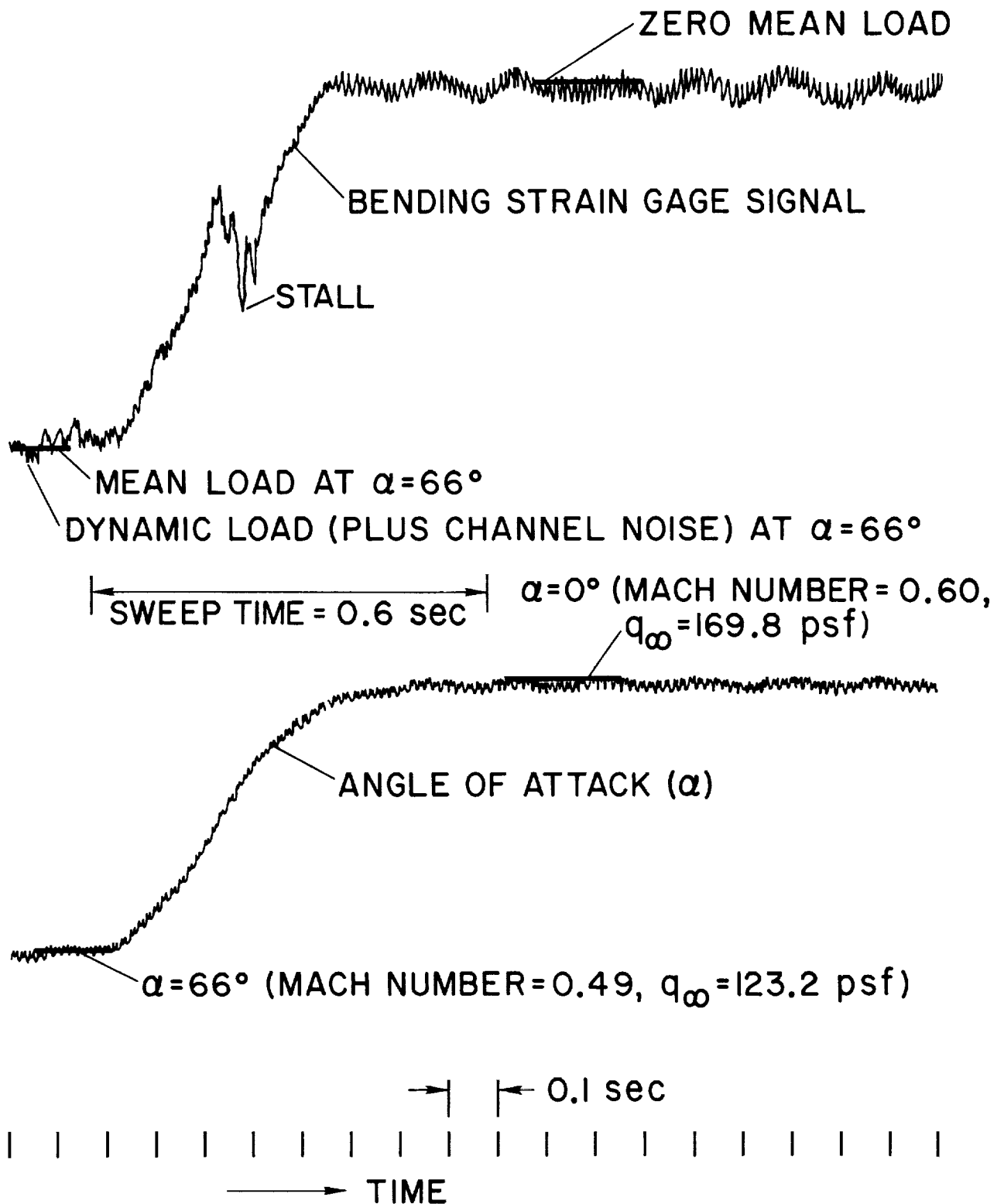
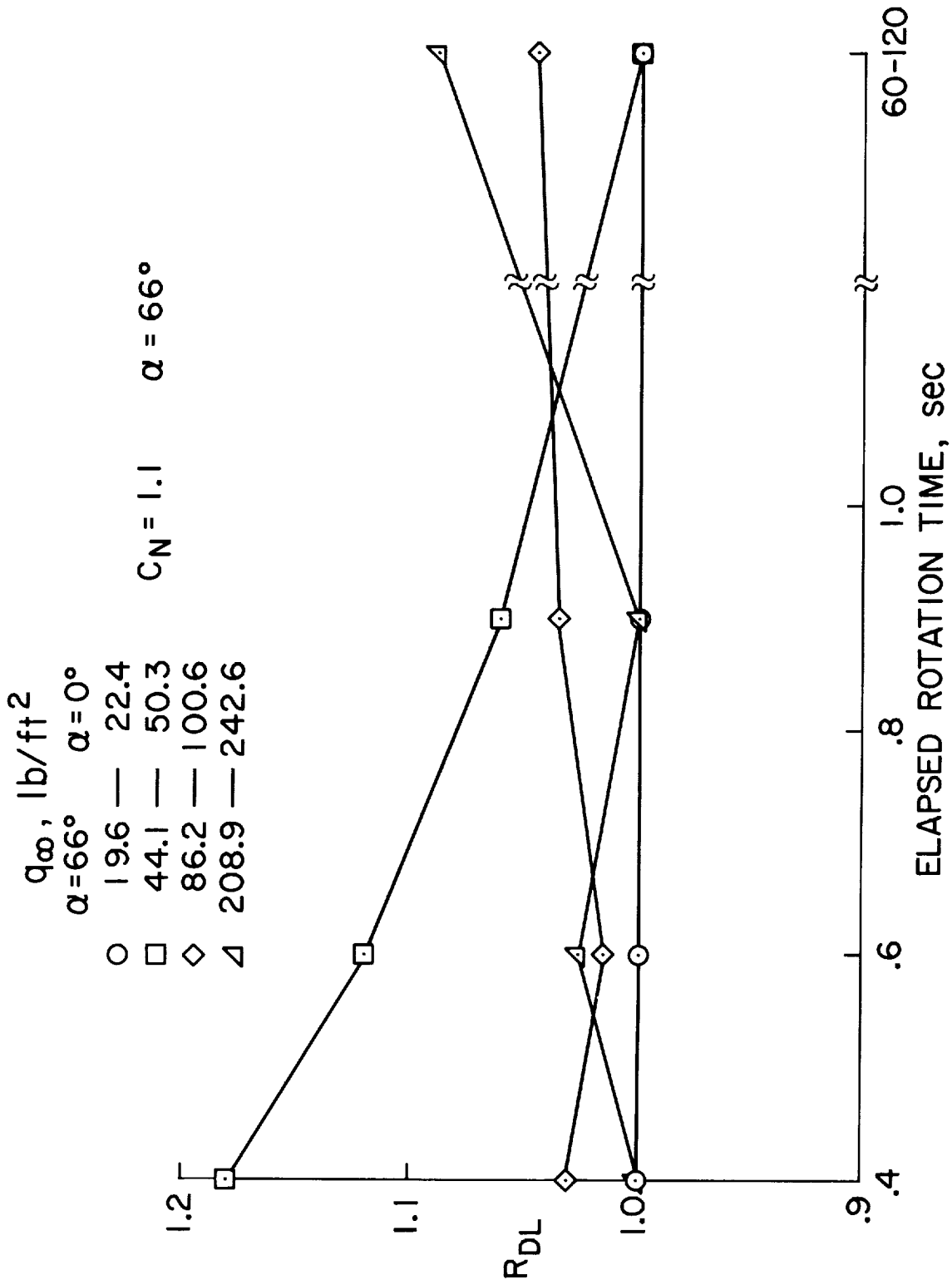
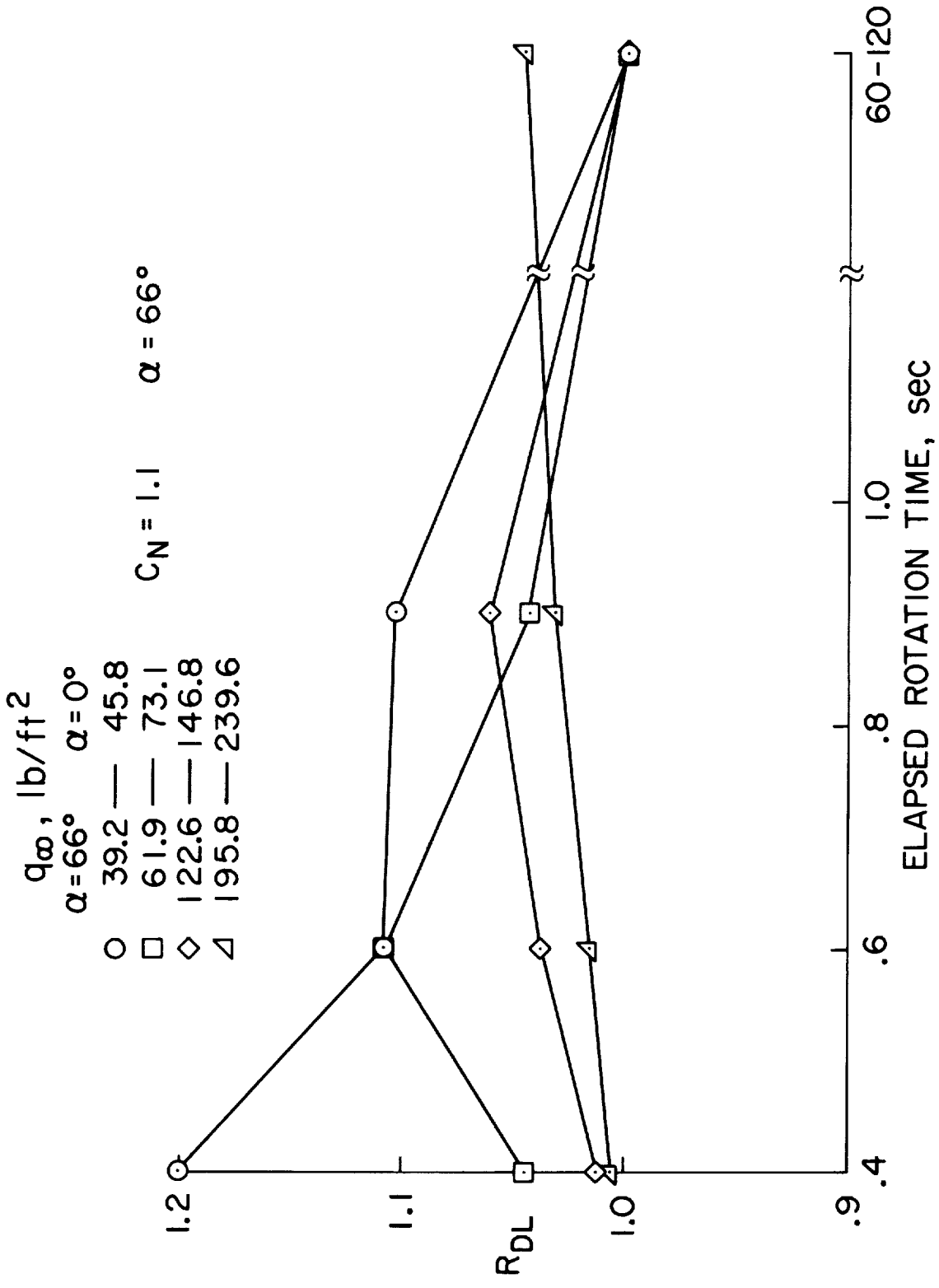


Figure 10.- Time history of bending during wing rotation with a sweep time of 0.6 sec. and Mach numbers from 0.49 to 0.60.



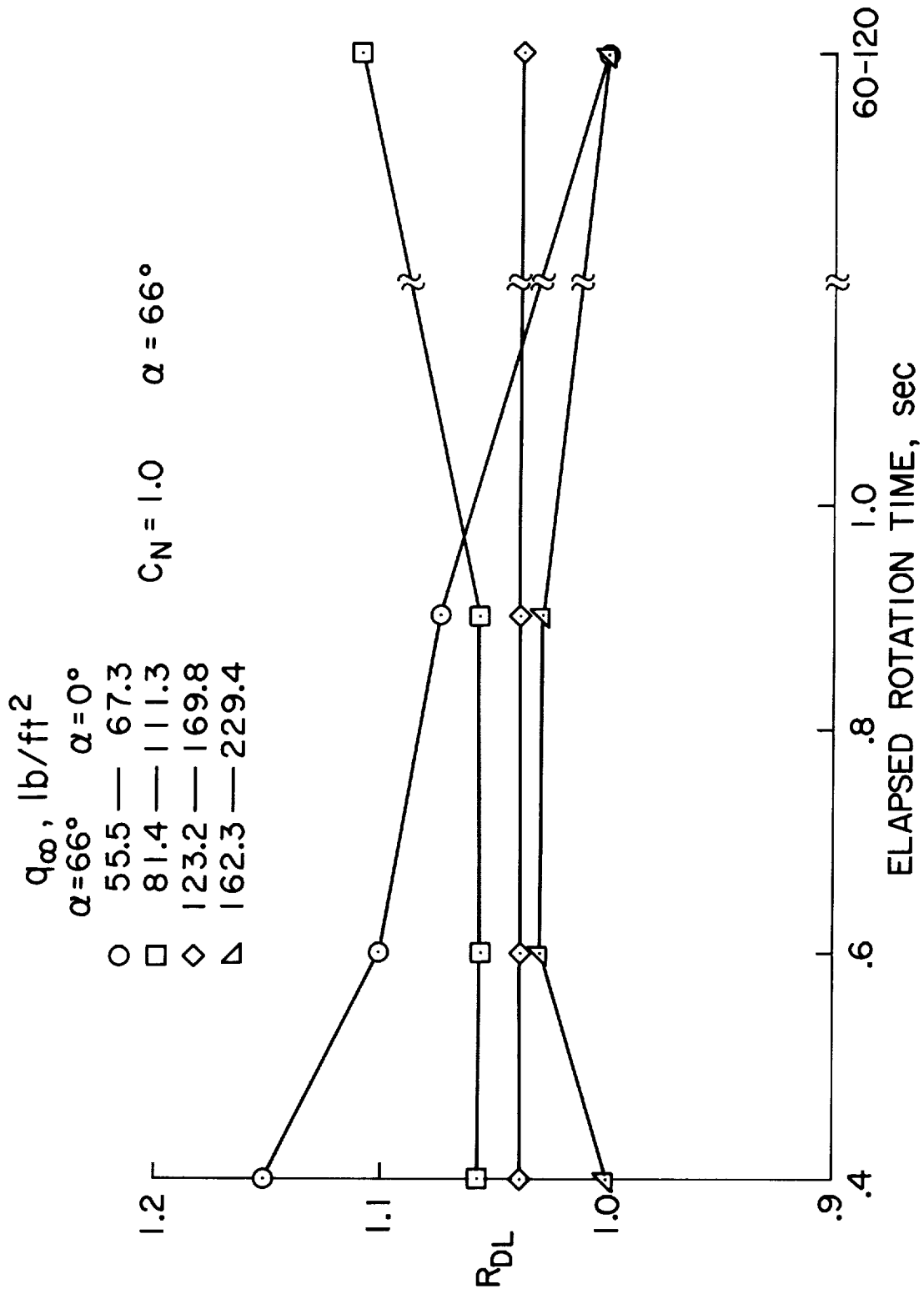
(a) $M = 0.28$ (at $\alpha = 66^\circ$) to 0.30 (at $\alpha = 0^\circ$).

Figure 11.- Ratio (R_{DL}) of maximum total load (including vibrations) to maximum mean load for rotation of wing "A".



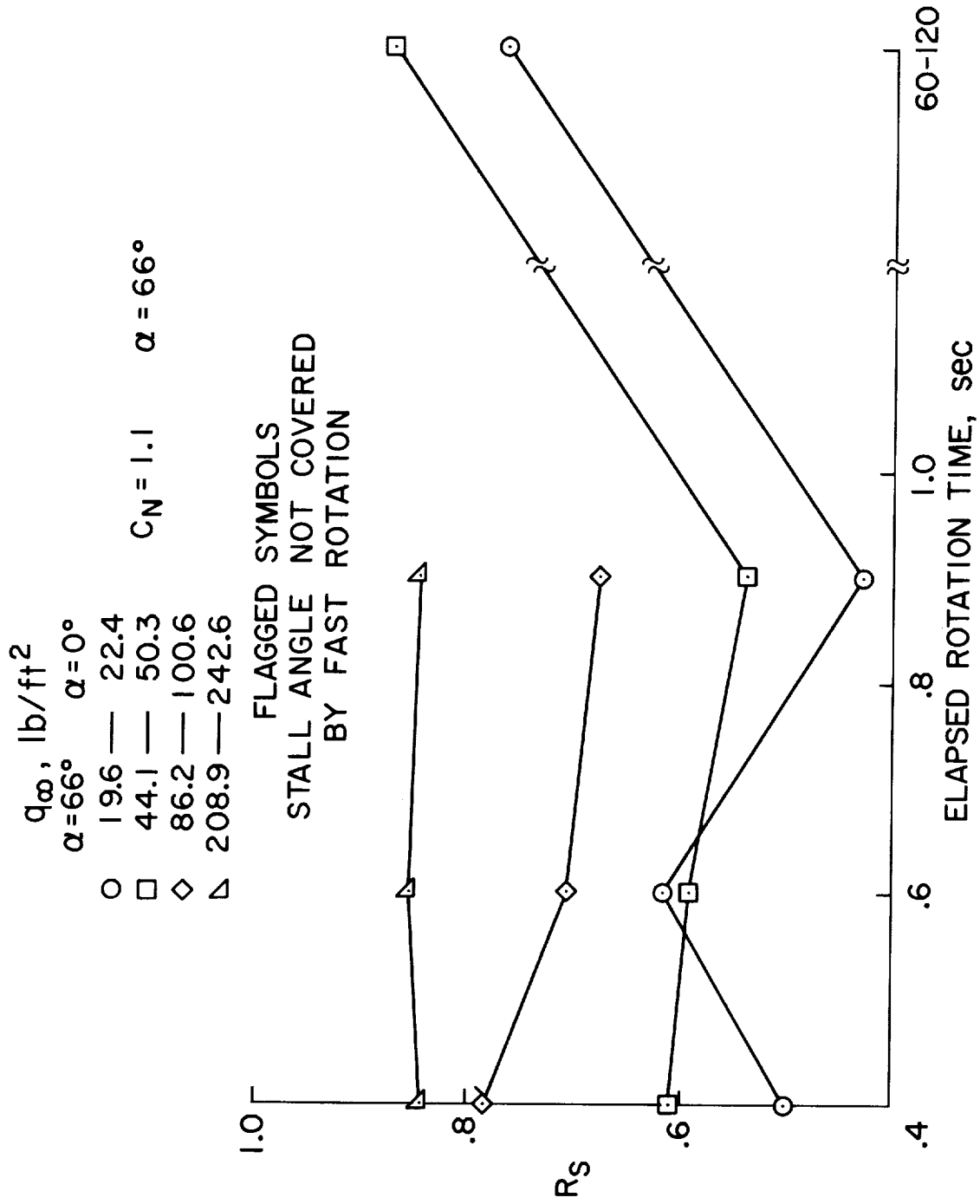
(b) $M = 0.40$ (at $\alpha = 66^{\circ}$) to 0.45 (at $\alpha = 0^{\circ}$).

Figure 11.- Continued.

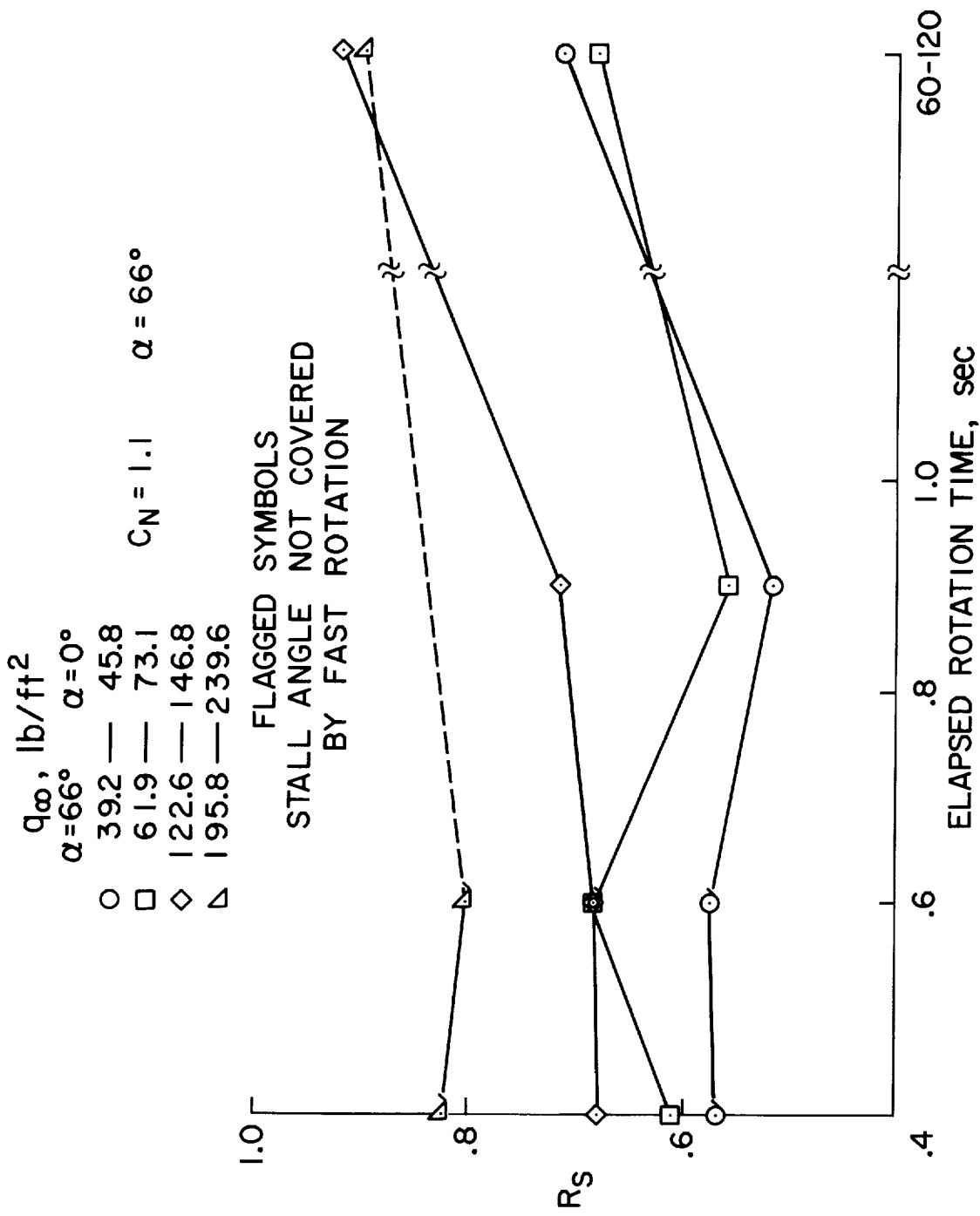


(c) $M = 0.49$ (at $\alpha = 66^\circ$) to 0.60 (at $\alpha = 0^\circ$).

Figure 11.- Concluded.

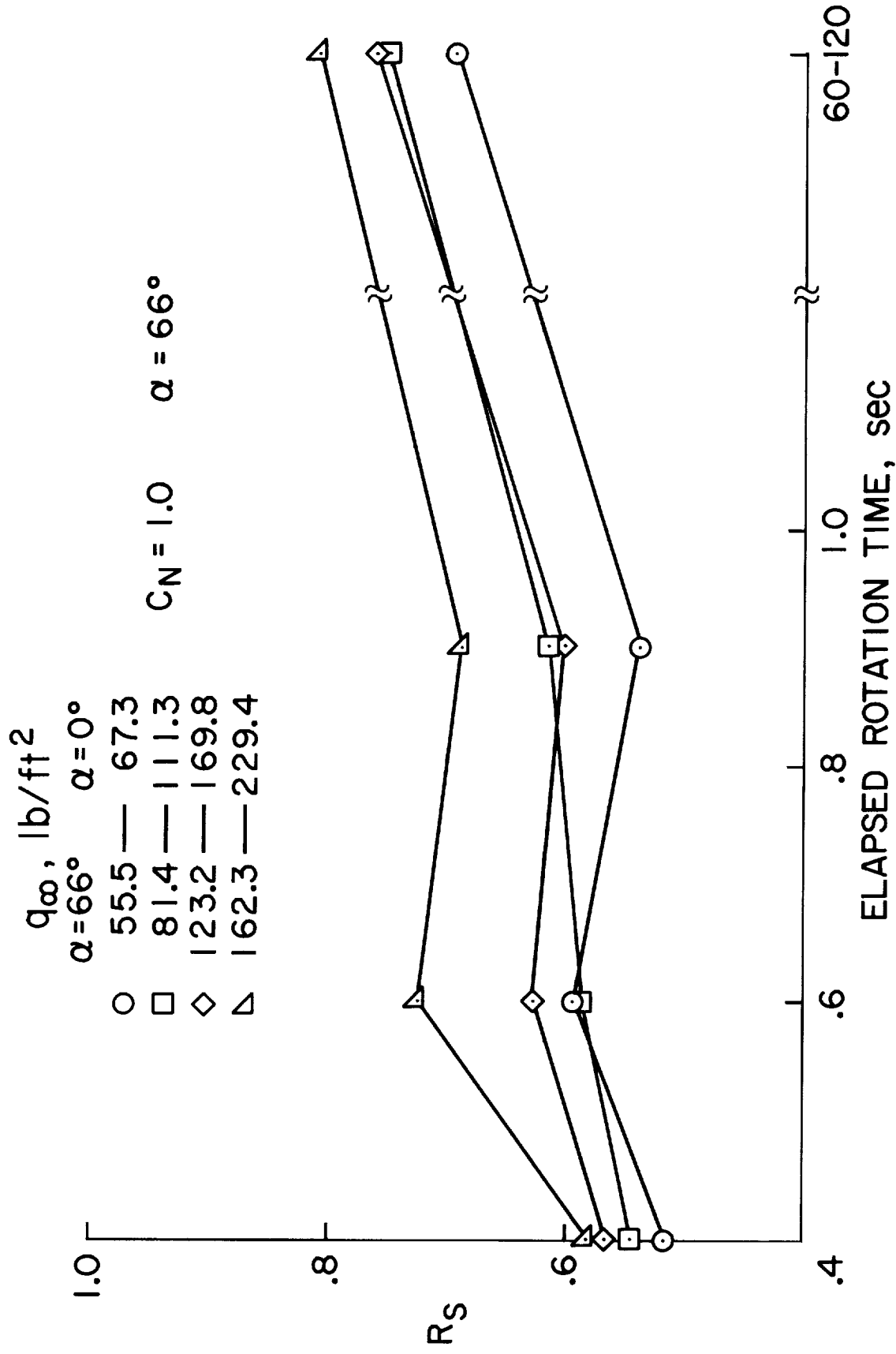


(a) $M = 0.28$ (at $\alpha = 66^\circ$) to 0.30 (at $\alpha = 0^\circ$).
 Figure 12.- Ratio (R_s) of mean load at stall to maximum mean load for rotation of wing "A".



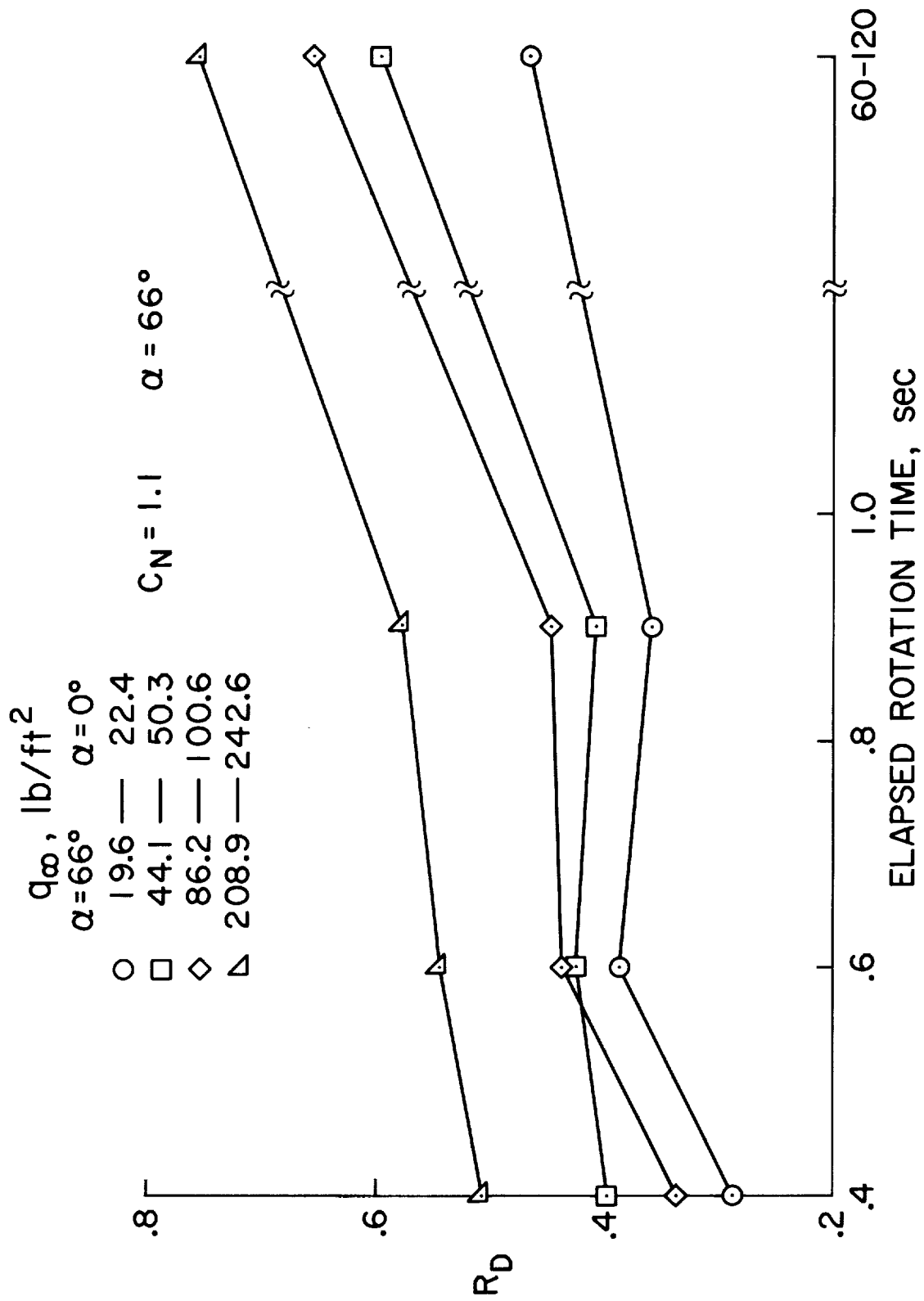
(b) $M = 0.40$ (at $\alpha = 66^\circ$) to 0.45 (at $\alpha = 0^\circ$).

Figure 12.- Continued.



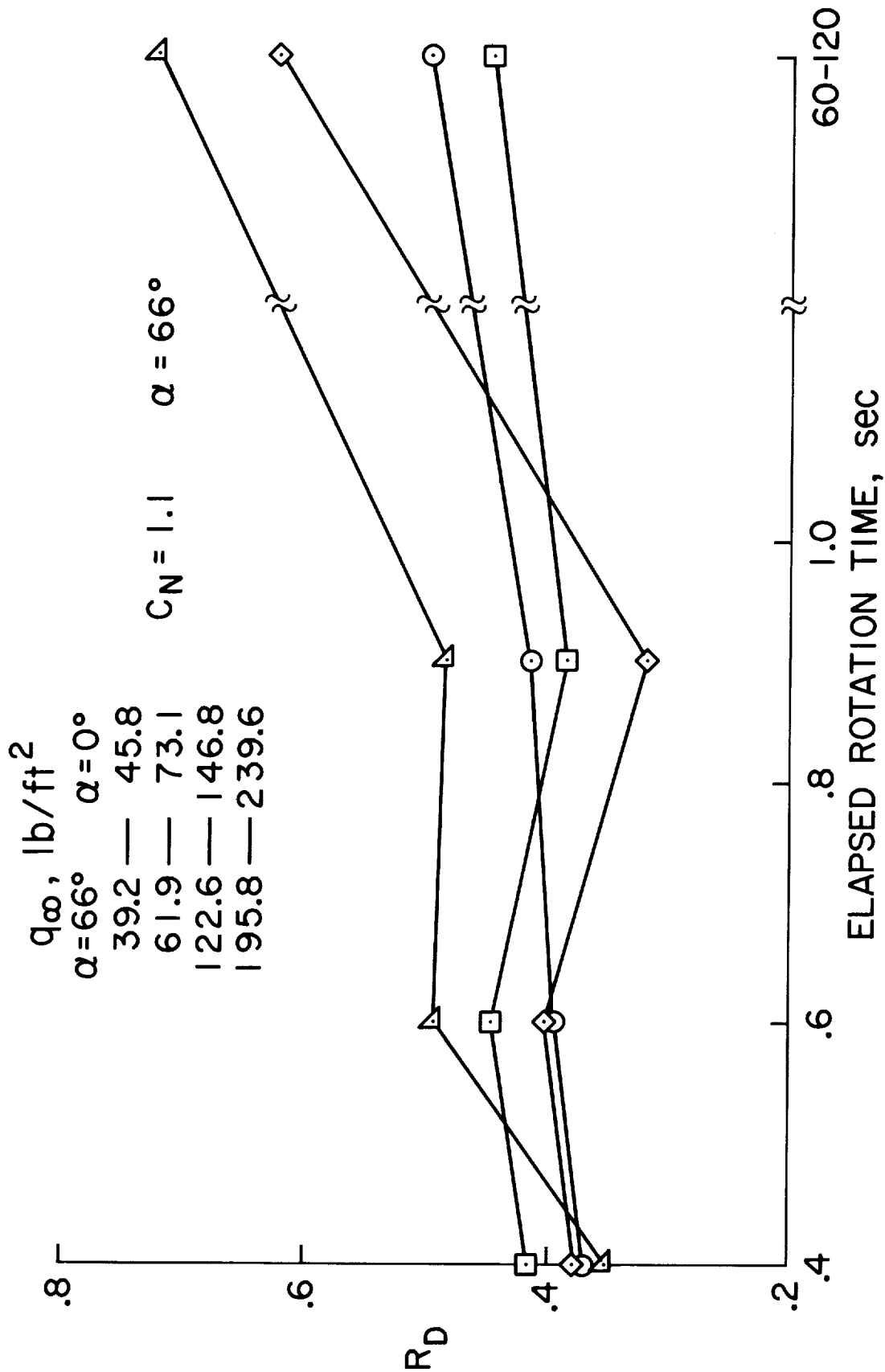
(c) $M = 0.49$ (at $\alpha = 66^\circ$) to 0.60 (at $\alpha = 0^\circ$).

Figure 12.- Concluded.



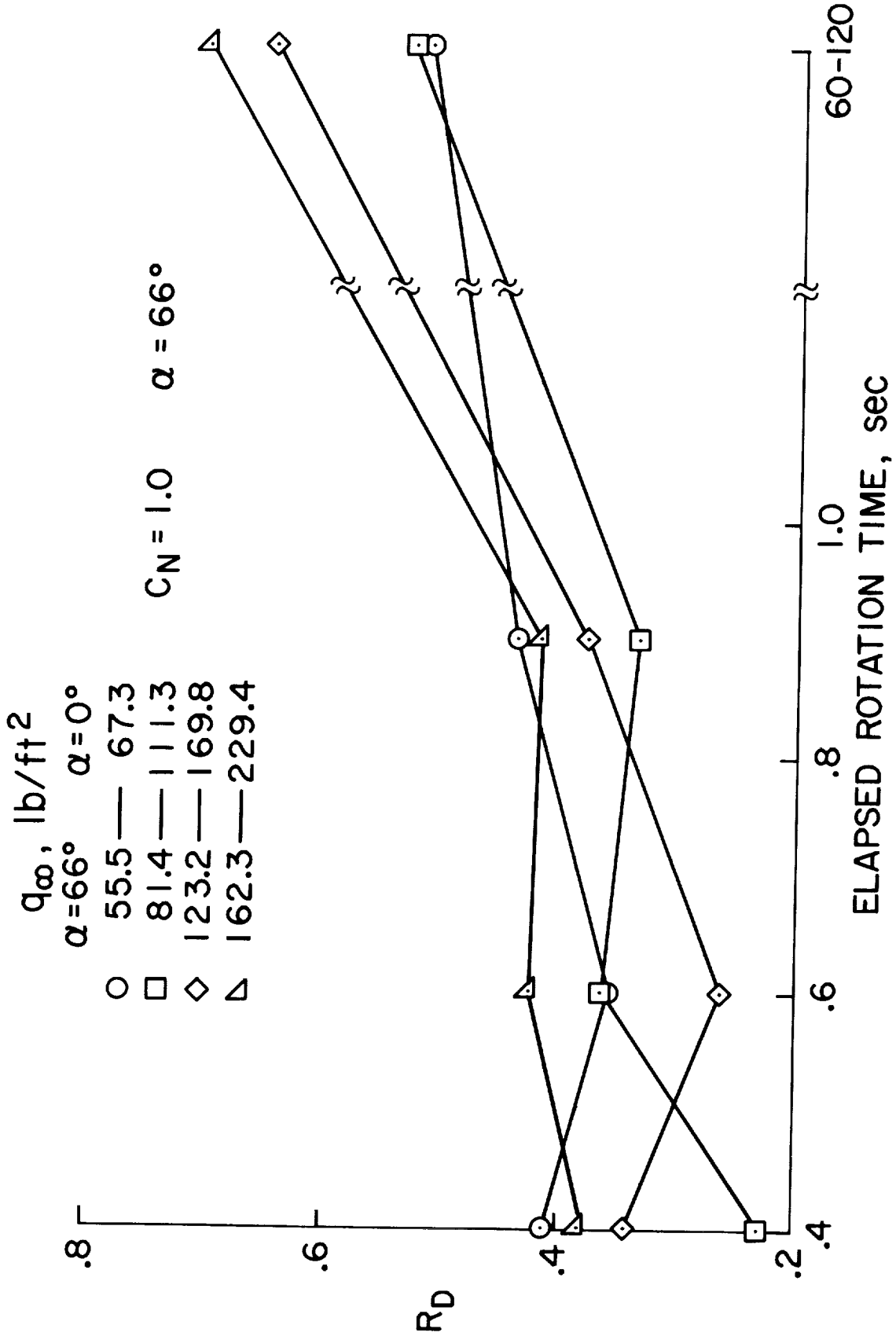
(a) $M = 0.28$ (at $\alpha = 66^{\circ}$) to 0.30 (at $\alpha = 0^{\circ}$).

Figure 13.- Ratio (R_D) of mean load at tip to maximum mean load for rotation of wing "A".



(b) $M = 0.40$ (at $\alpha = 66^\circ$) to 0.45 (at $\alpha = 0^\circ$).

Figure 13.- Continued.



(c) $M = 0.49$ (at $\alpha = 66^{\circ}$) to 0.60 (at $\alpha = 0^{\circ}$).

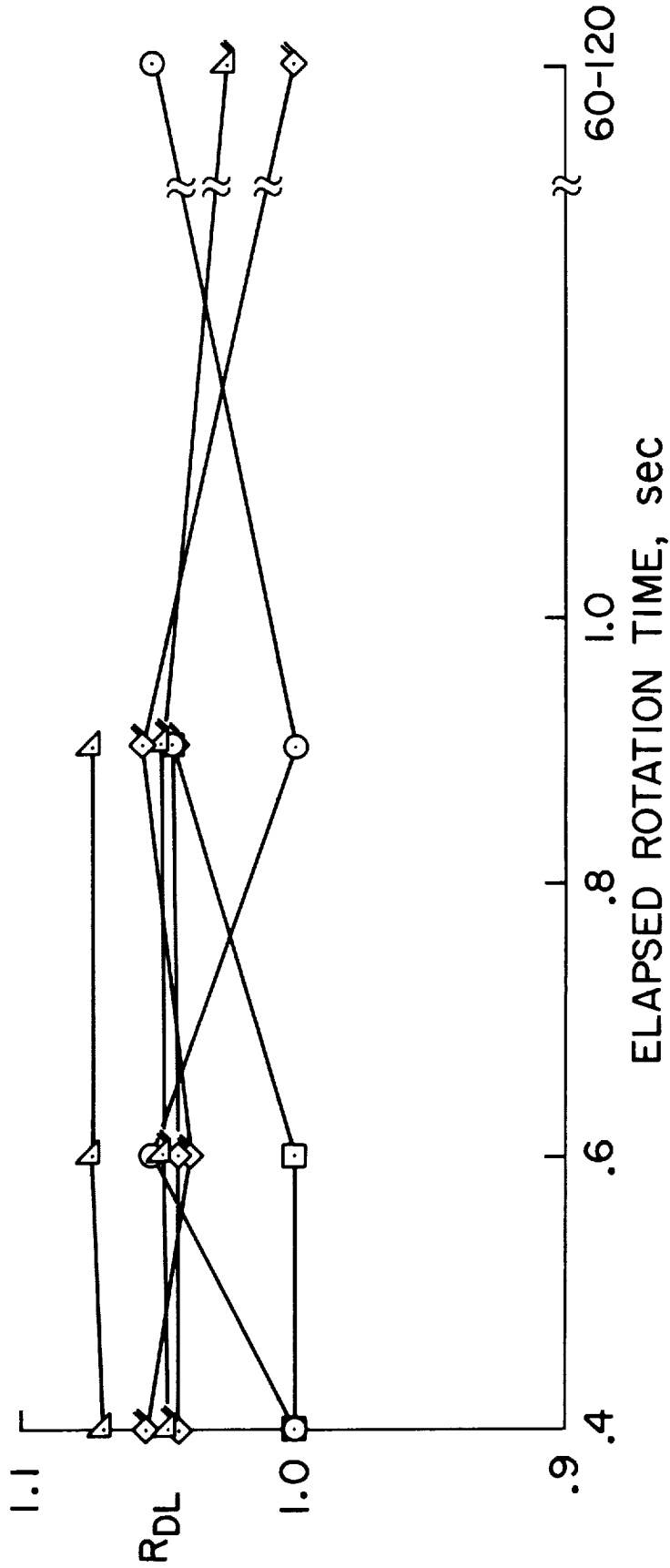
Figure 13.- Concluded.

q_{∞} , lb/ft²

$\alpha = 66^{\circ}$	$\alpha = 0^{\circ}$
○ 35.8 — 43.8	○ 35.8 — 43.8
□ 46.3 — 56.7	□ 46.3 — 56.7
◇ 48.5 — 59.4	◇ 48.5 — 59.4
△ 55.3 — 67.7	△ 55.3 — 67.7

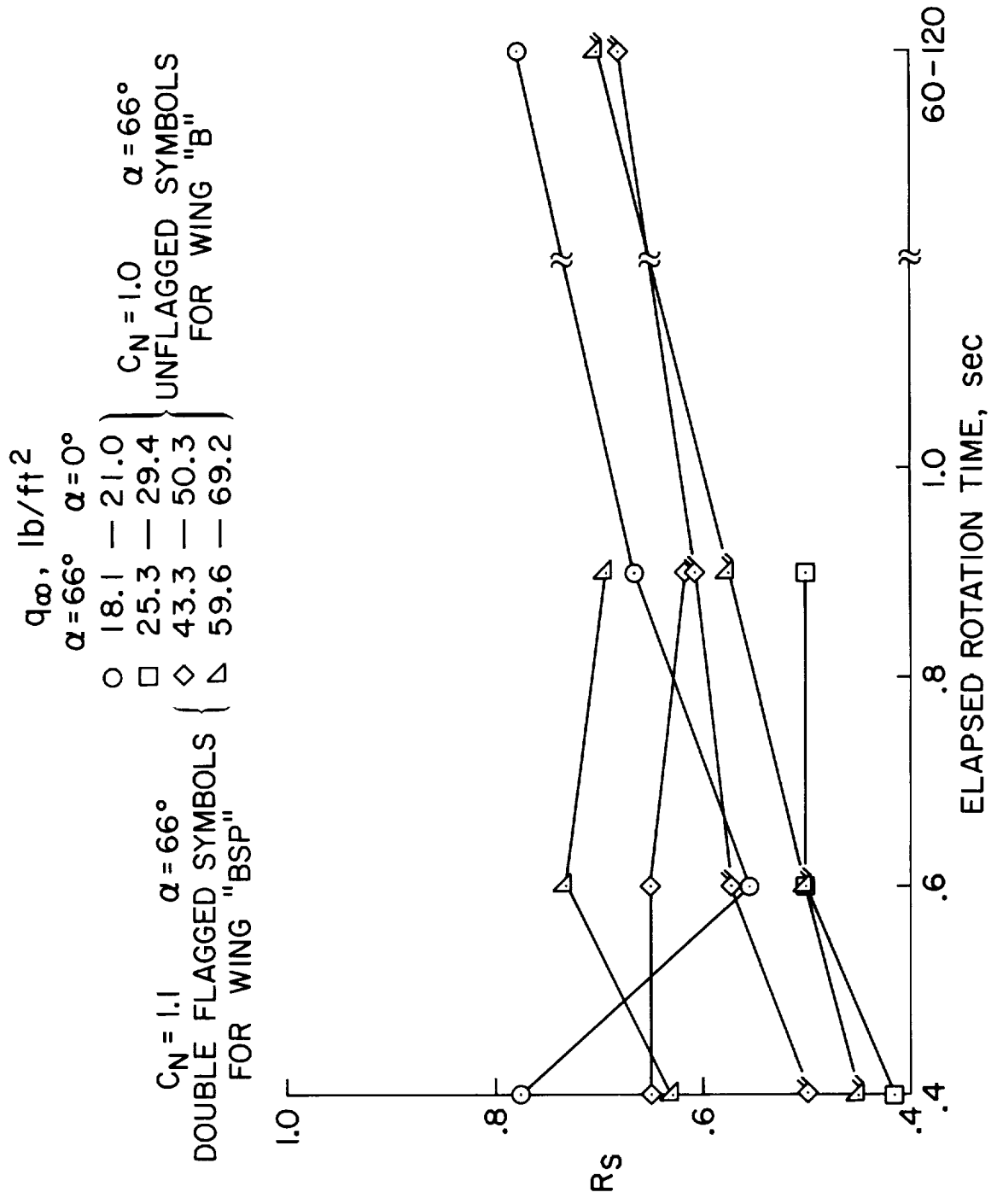
$C_N = 1.3$ $\alpha = 66^{\circ}$ $C_N = 1.1$ $\alpha = 66^{\circ}$

DOUBLE FLAGGED SYMBOLS { UNFLAGGED SYMBOLS
FOR WING "BSP" FOR WING "B"



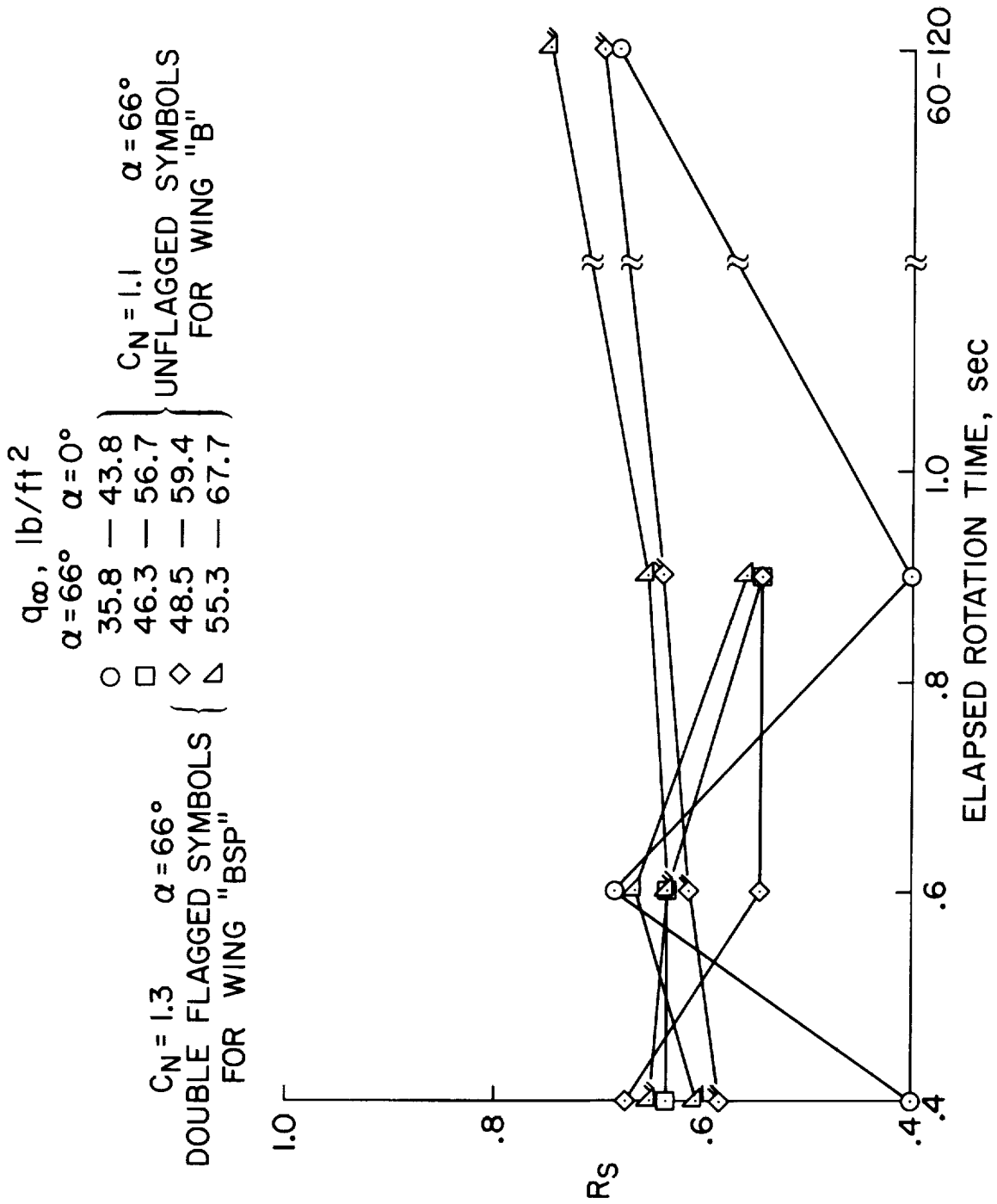
(b) $M = 0.40$ (at $\alpha = 66^{\circ}$) to 0.45 (at $\alpha = 0^{\circ}$).

Figure 14.- Concluded.



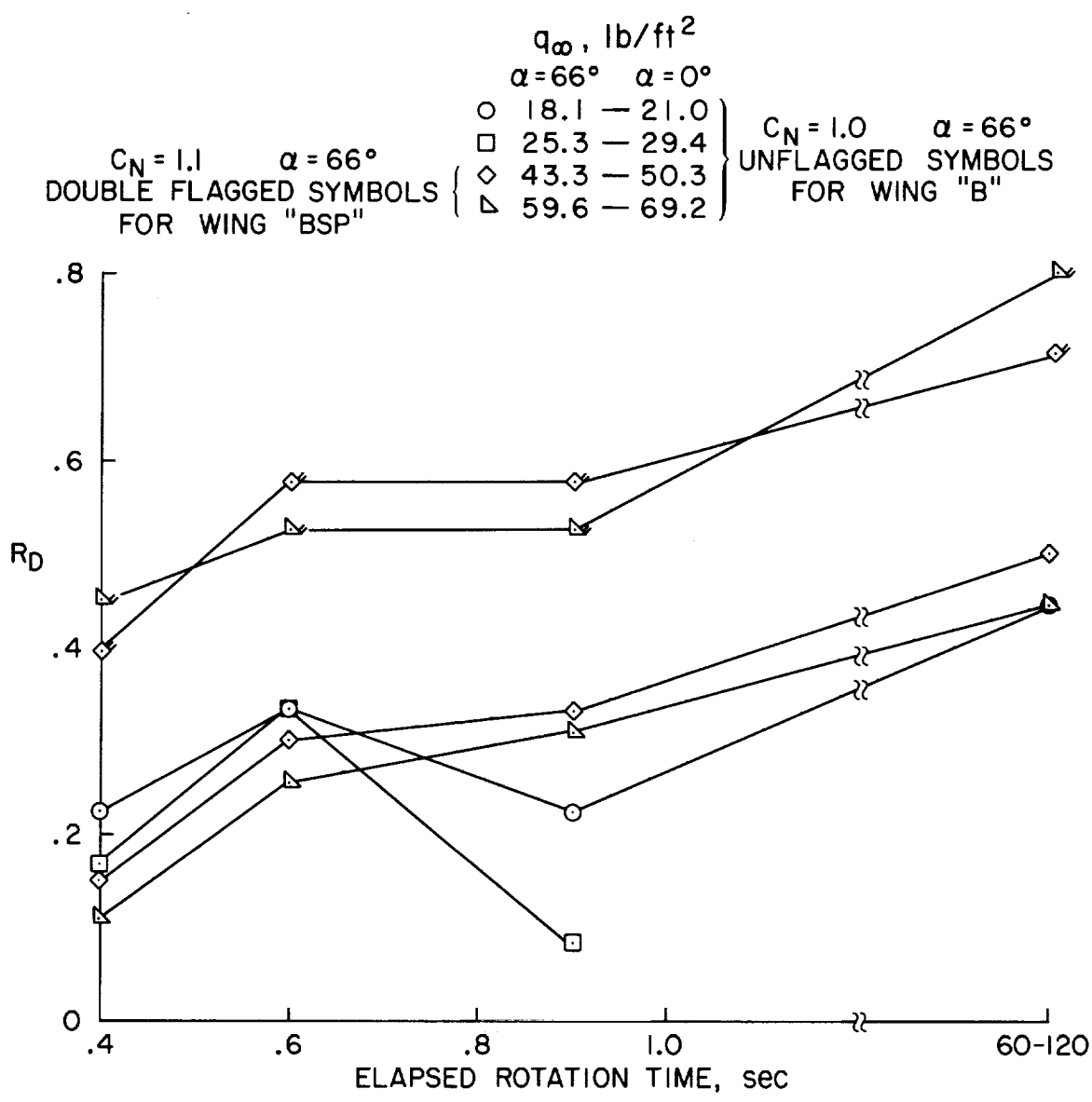
(a) $M = 0.28$ (at $\alpha = 66^\circ$) to 0.30 (at $\alpha = 0^\circ$).

Figure 15.- Ratio (R_S) of mean load at stall to maximum mean load for rotation of wings "B" and "BSP".



(b) $M = 0.40$ (at $\alpha = 66^\circ$) to 0.45 (at $\alpha = 0^\circ$).

Figure 15.- Concluded.



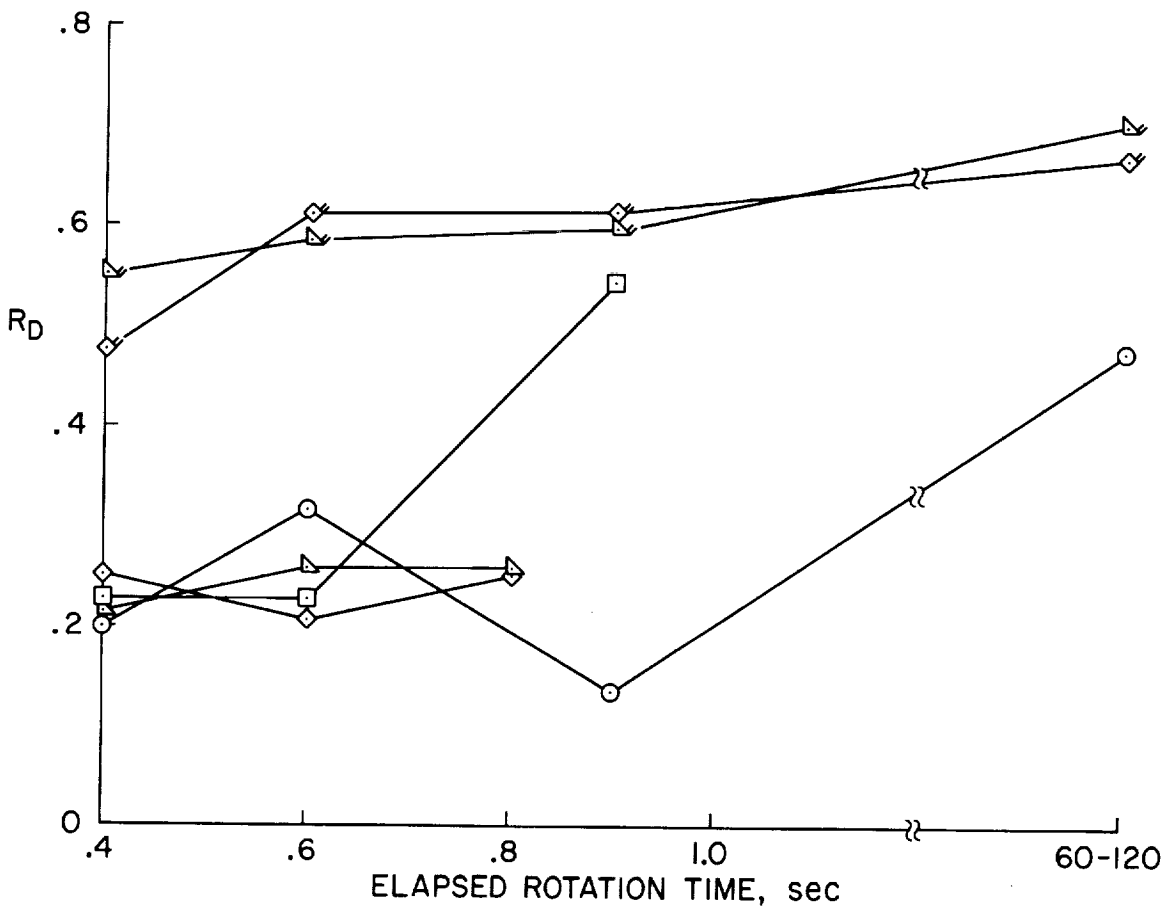
(a) $M = 0.28$ (at $\alpha = 66^{\circ}$) to 0.30 (at $\alpha = 0^{\circ}$).

Figure 16.- Ratio (R_D) of mean load at dip to maximum mean load for rotation of wings "B" and "BSP".

q_{∞} , lb/ft²

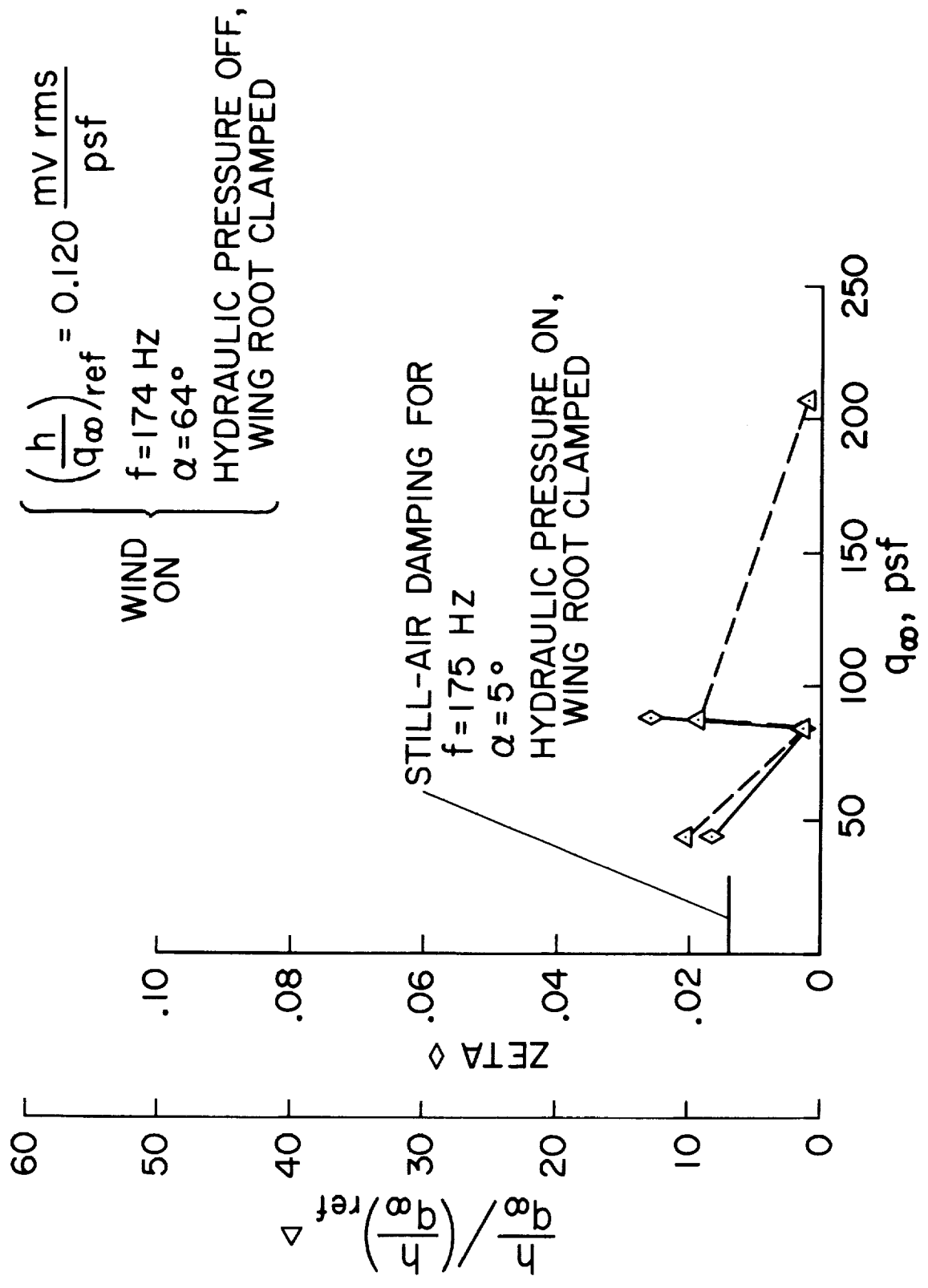
	$\alpha = 66^\circ$	$\alpha = 0^\circ$	
$C_N = 1.3$ $\alpha = 66^\circ$ DOUBLE FLAGGED SYMBOLS FOR WING "BSP"	○	—	43.8
	□	—	56.7
	◇	—	59.4
	△	—	67.7

$C_N = 1.1$ $\alpha = 66^\circ$
 UNFLAGGED SYMBOLS
 FOR WING "B"

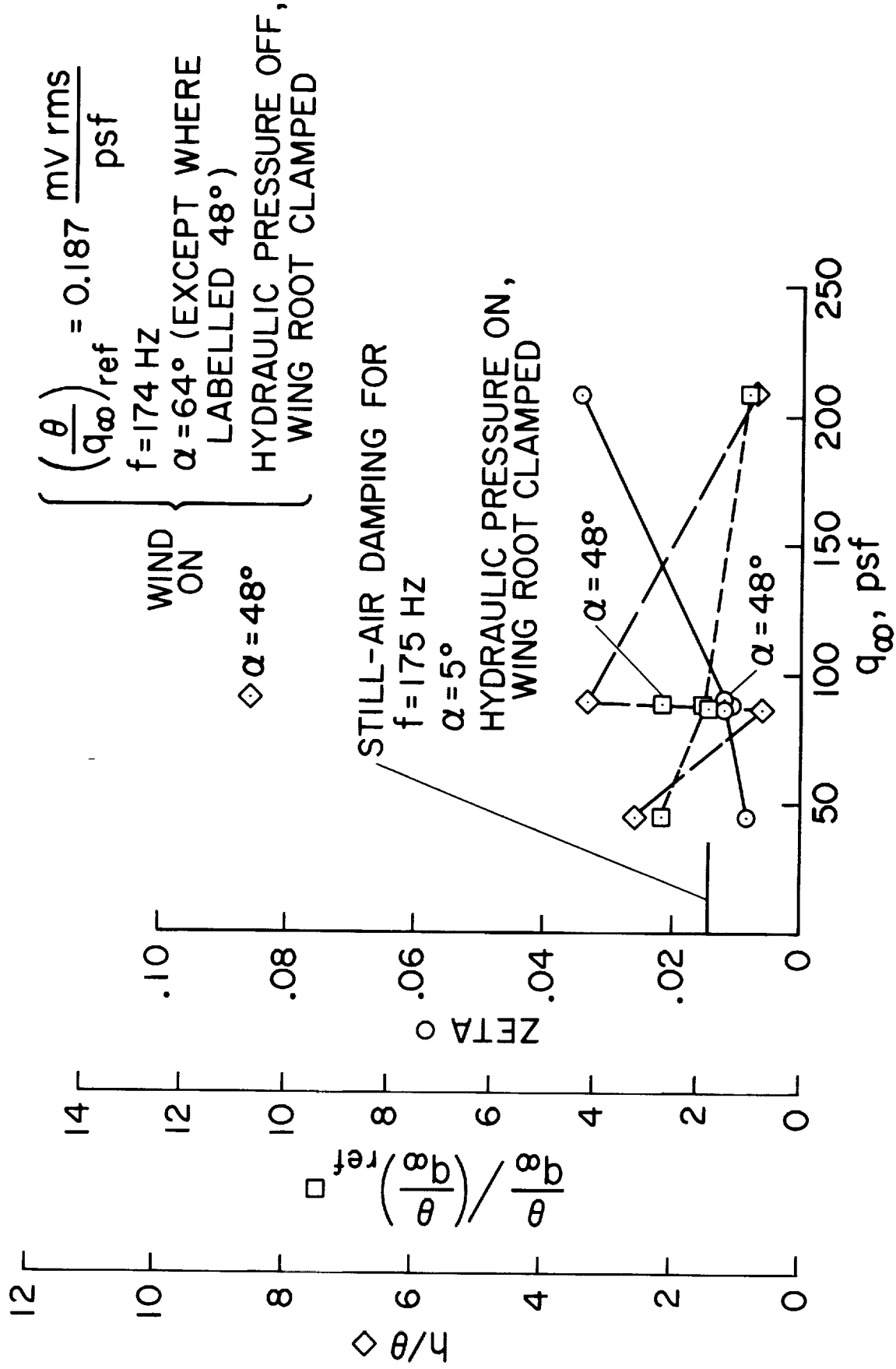


(b) $M = 0.40$ (at $\alpha = 66^\circ$) to 0.45 (at $\alpha = 0^\circ$).

Figure 16.- Concluded.



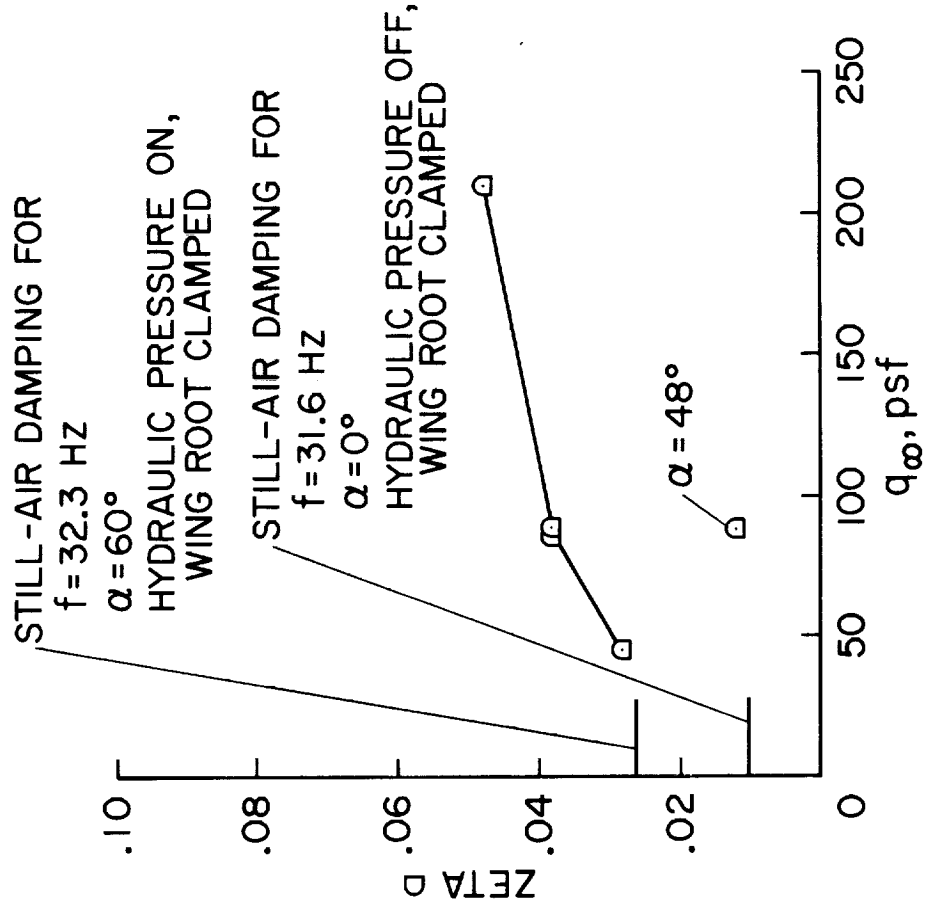
(a) Bending at 174 Hz (3rd bending and 2nd torsion).
 Figure 17.- Total damping and root mean square oscillations at M = 0.28 for wing "A".



(b) Torsion at 174 Hz (3rd bending and 2nd torsion).

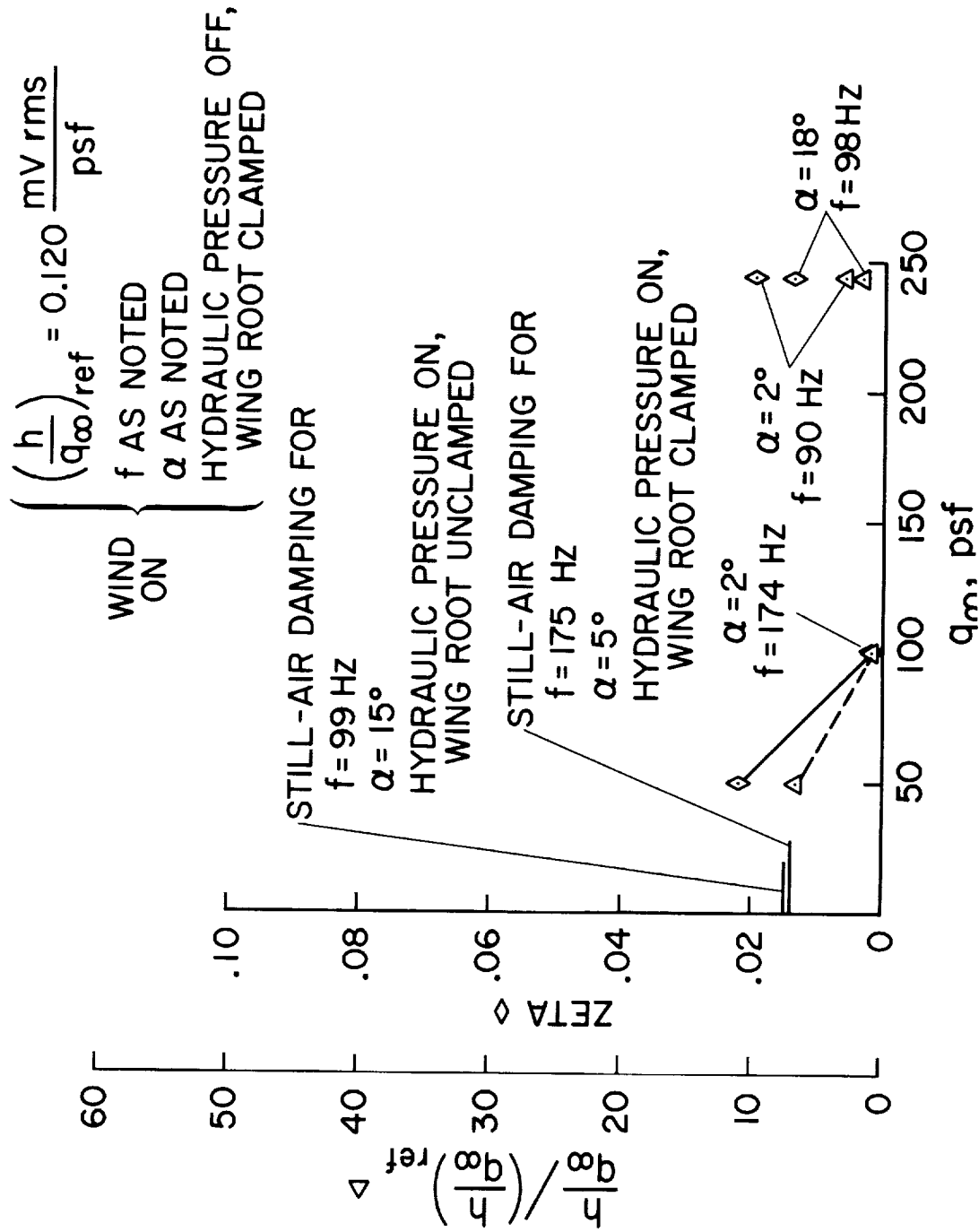
Figure 17.- Continued.

$f = 34 \text{ Hz}$
 $\alpha = 64^\circ$ (EXCEPT WHERE LABELLED 48°)
 WIND ON { HYDRAULIC PRESSURE OFF, WING ROOT CLAMPED



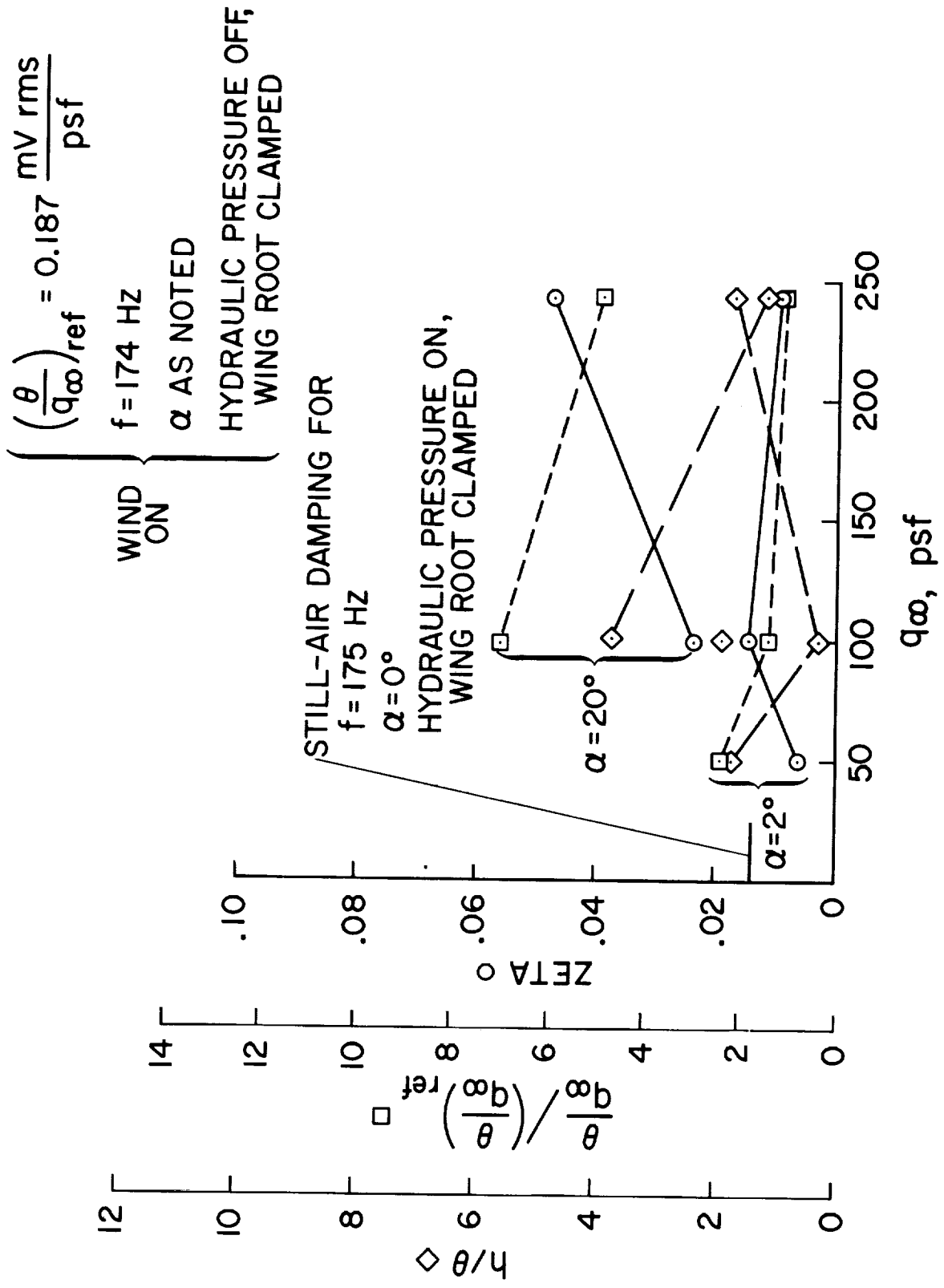
(c) Bending at 34 Hz (1st bending).

Figure 17.- Concluded.



(a) Bending at 90 to 98 Hz (1st torsion and 2nd bending) and at 174 Hz (3rd bending and 2nd torsion).

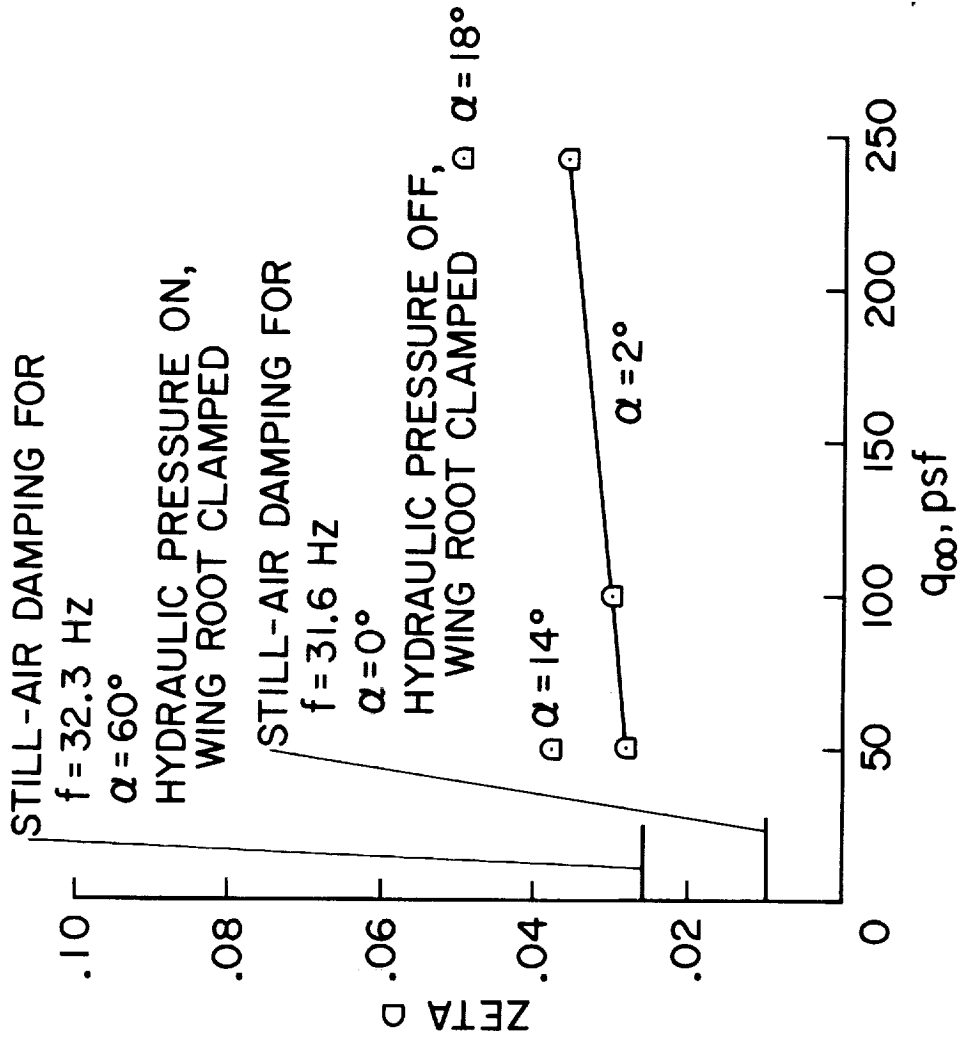
Figure 18.- Total damping and root mean square oscillations at $M = 0.30$ for wing "A".



(b) Torsion at 174 Hz (3rd bending and 2nd torsion).

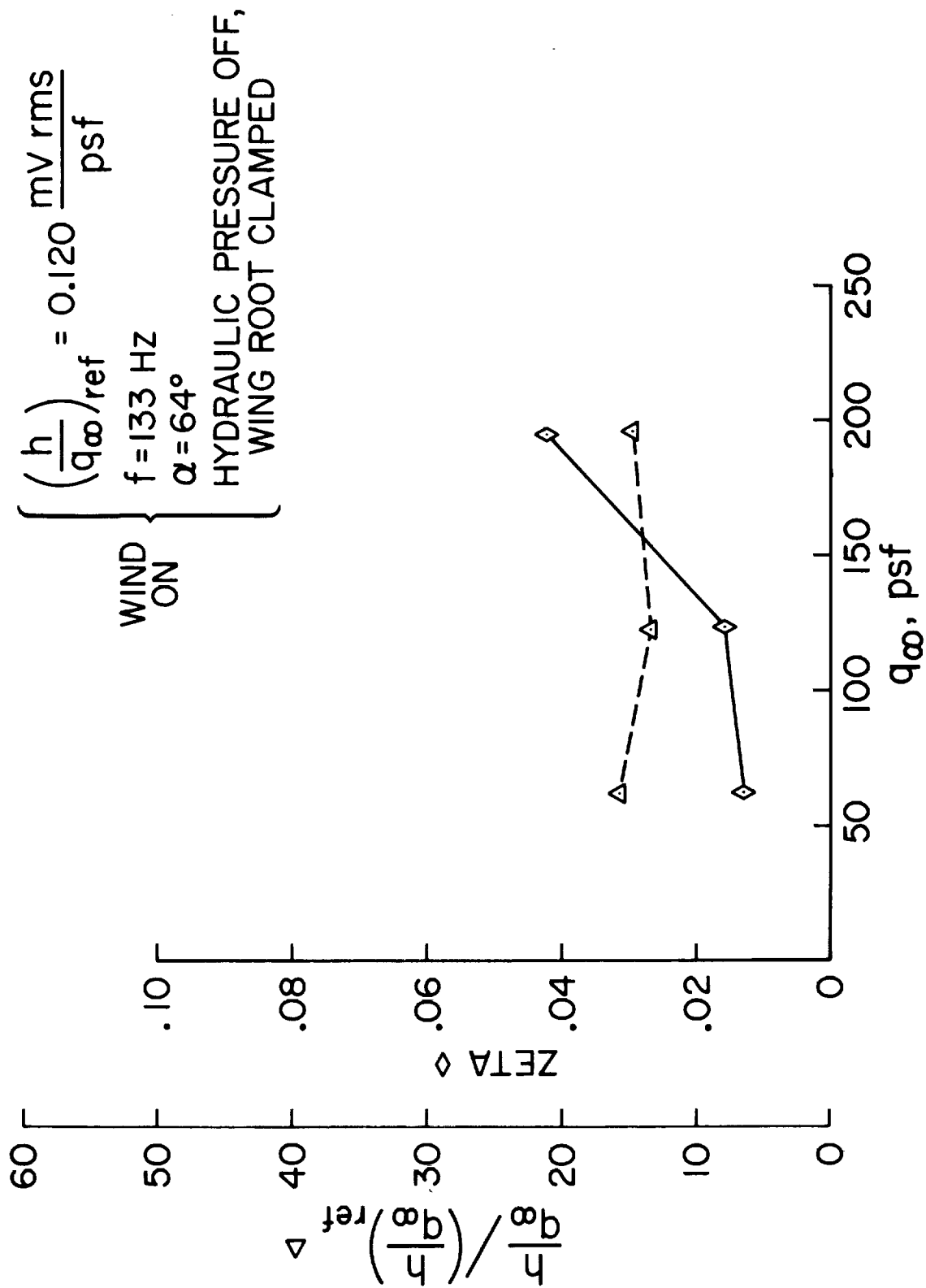
Figure 18.- Continued.

WIND ON $\left\{ \begin{array}{l} f = 34 \text{ HZ} \\ \alpha \text{ AS NOTED} \\ \text{HYDRAULIC PRESSURE OFF,} \\ \text{WING ROOT CLAMPED} \end{array} \right.$

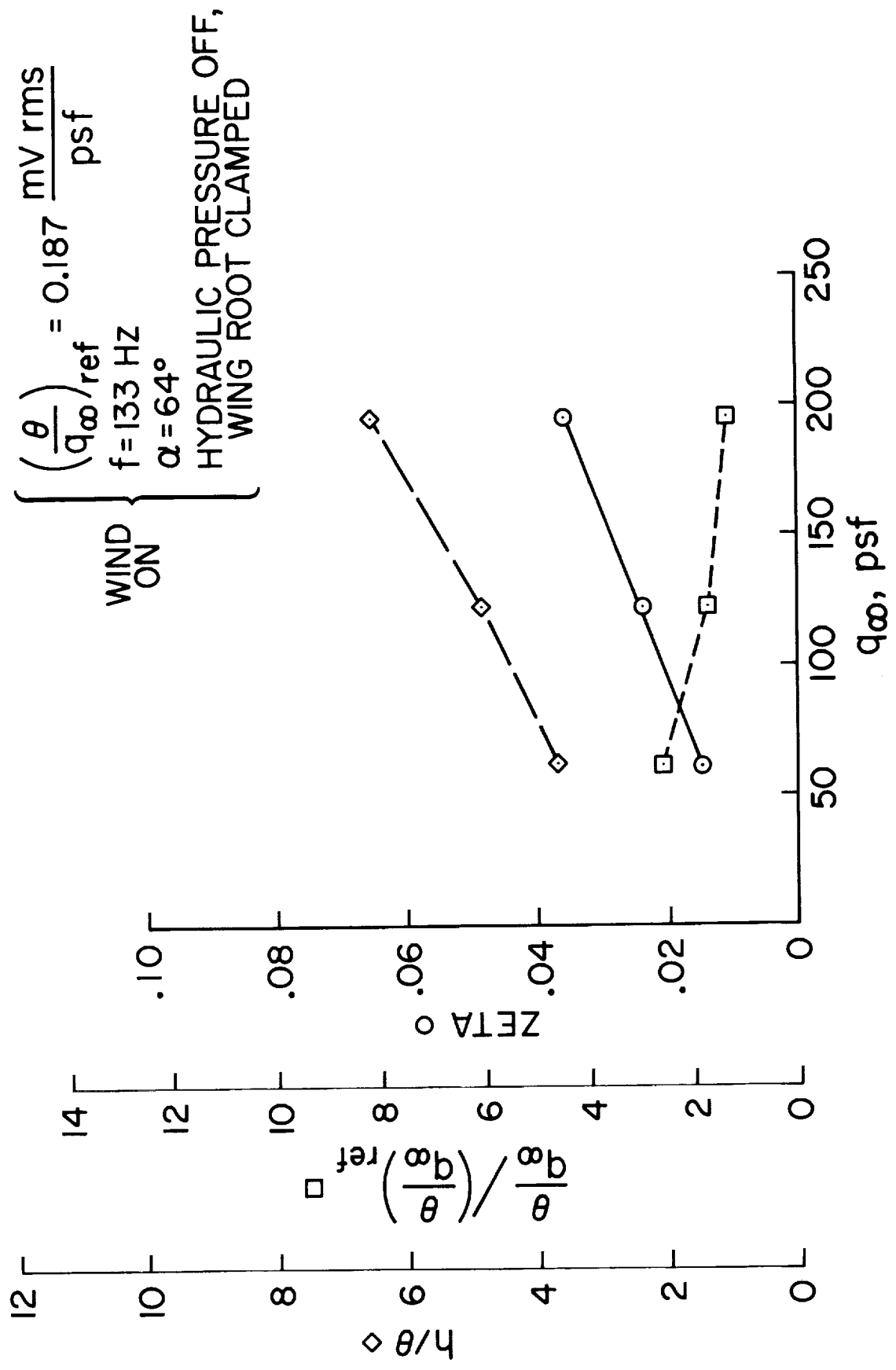


(c) Bending at 34 Hz (1st bending).

Figure 18.- Concluded.



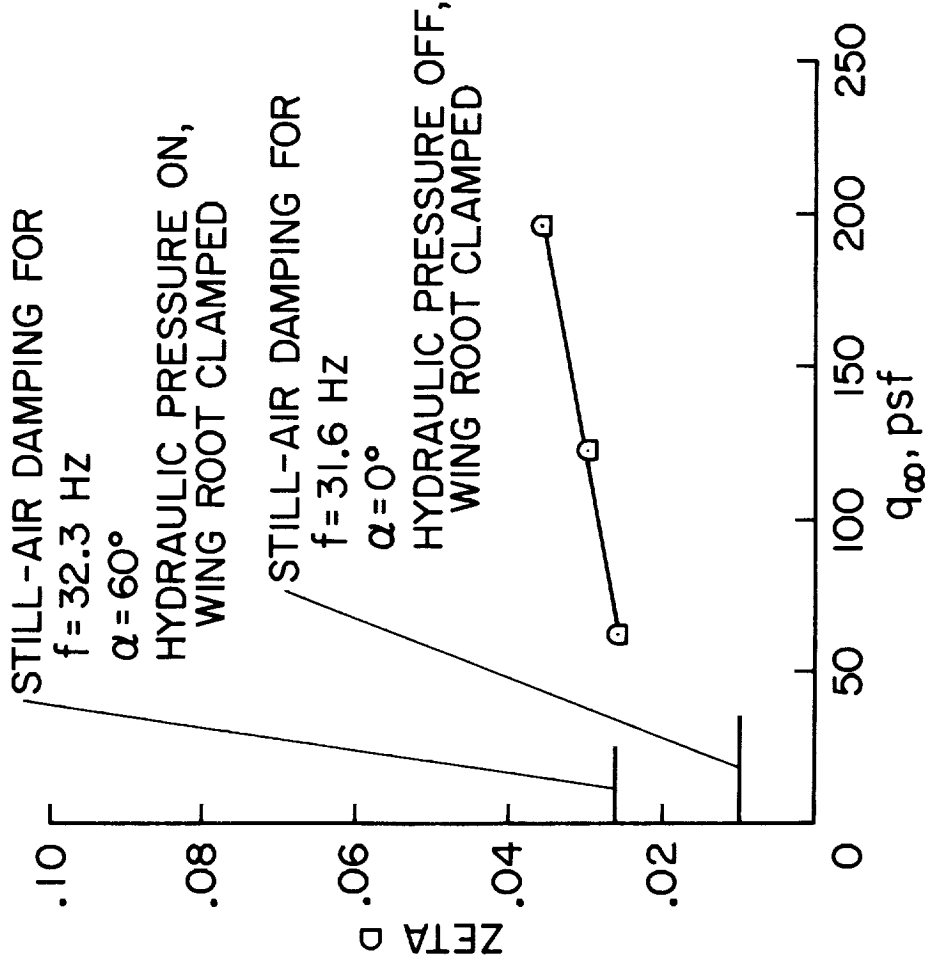
(a) Bending at 133 Hz (1st torsion and 3rd bending).
 Figure 19.- Total damping and root mean square oscillations at $M = 0.40$ for wing "A".



(b) Torsion at 133 Hz (1st torsion and 3rd bending).

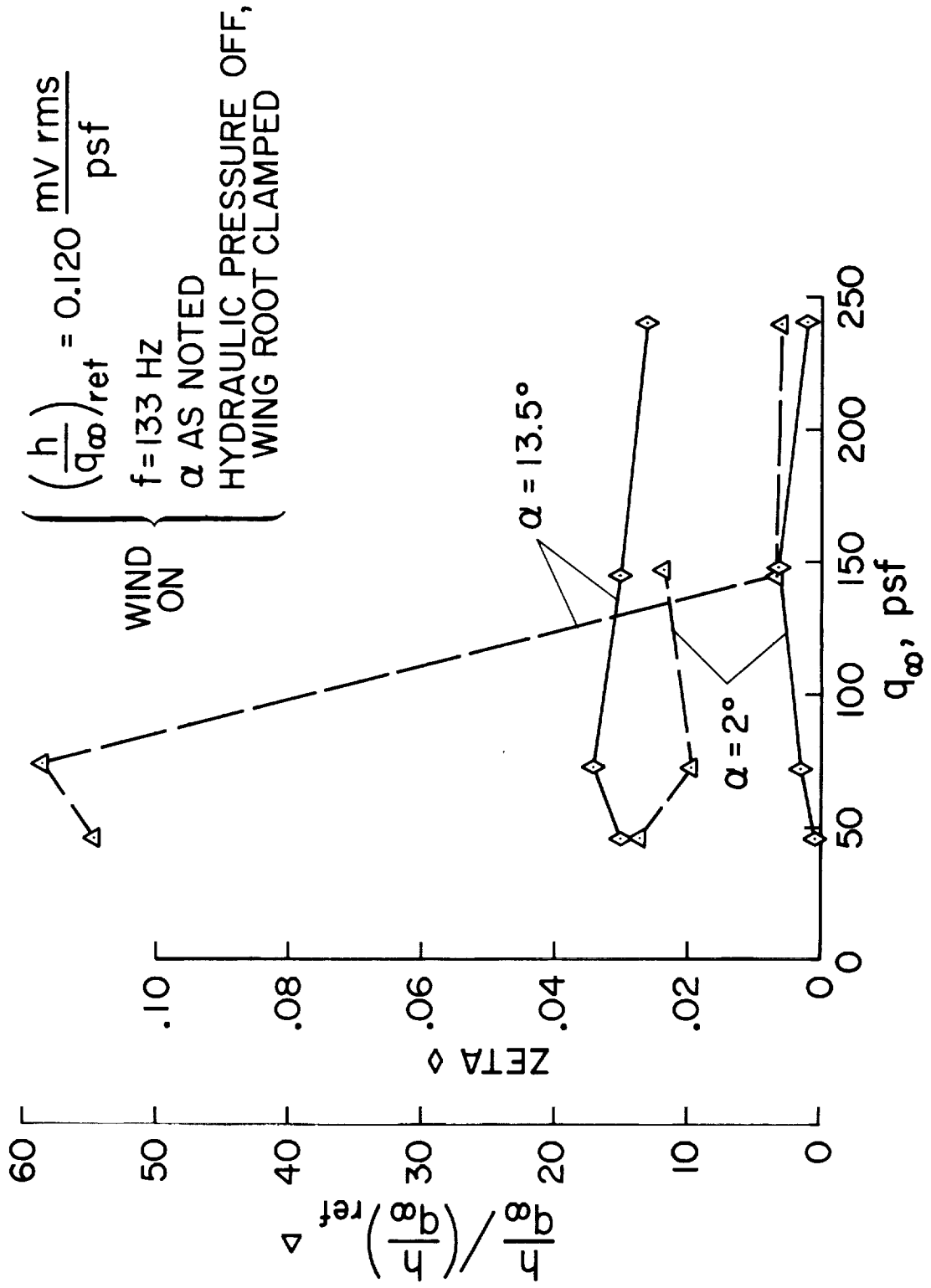
Figure 19.- Continued.

$f = 34 \text{ HZ}$
 $\alpha = 64^\circ$
 WIND ON
 HYDRAULIC PRESSURE OFF,
 WING ROOT CLAMPED

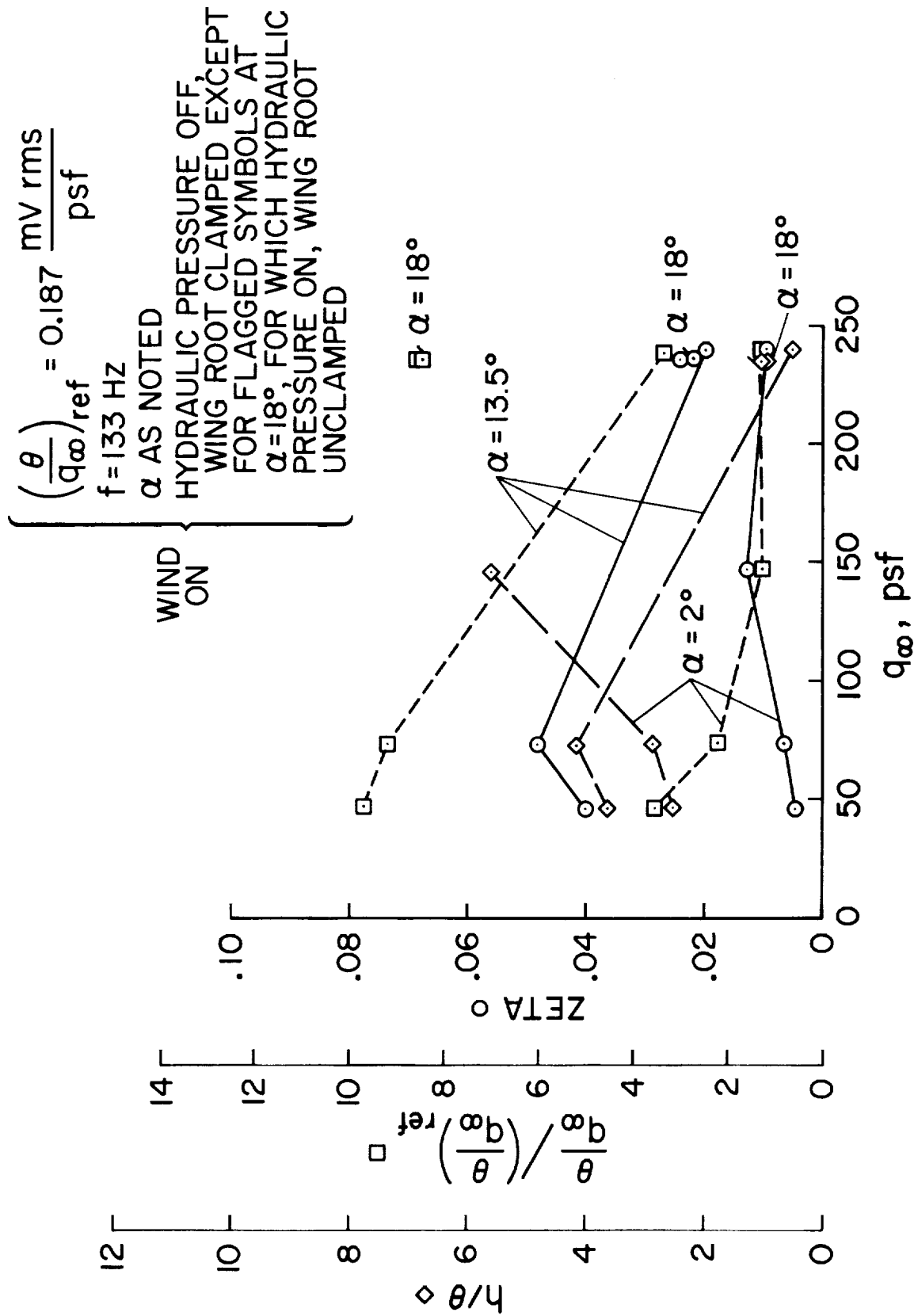


(c) Bending at 34 Hz (1st bending).

Figure 19.- Concluded.



(a) Bending at 133 Hz (1st torsion and 3rd bending).
 Figure 20.- Total damping and root mean square oscillations at $M = 0.45$ for wing "A".



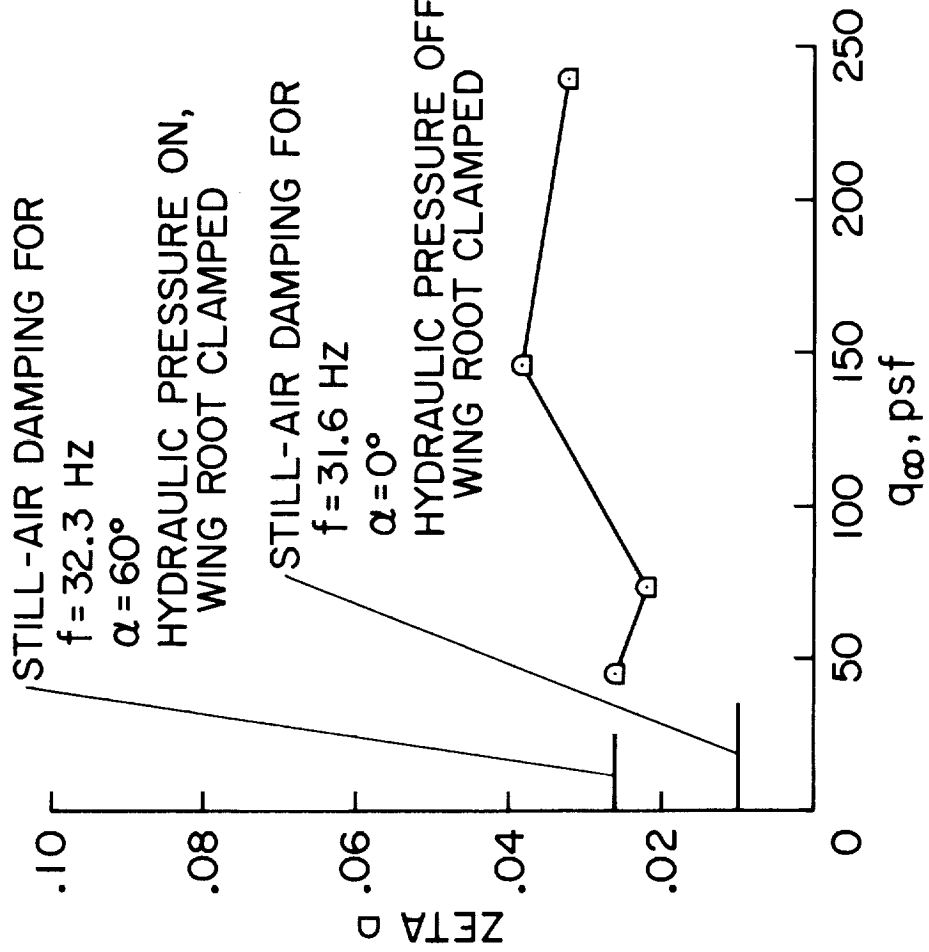
(b) Torsion at 133 Hz (1st torsion and 3rd bending).

Figure 20.- Continued.

$f = 34 \text{ Hz}$
 $\alpha = 2^\circ$
 WIND ON { HYDRAULIC PRESSURE OFF,
 WING ROOT CLAMPED

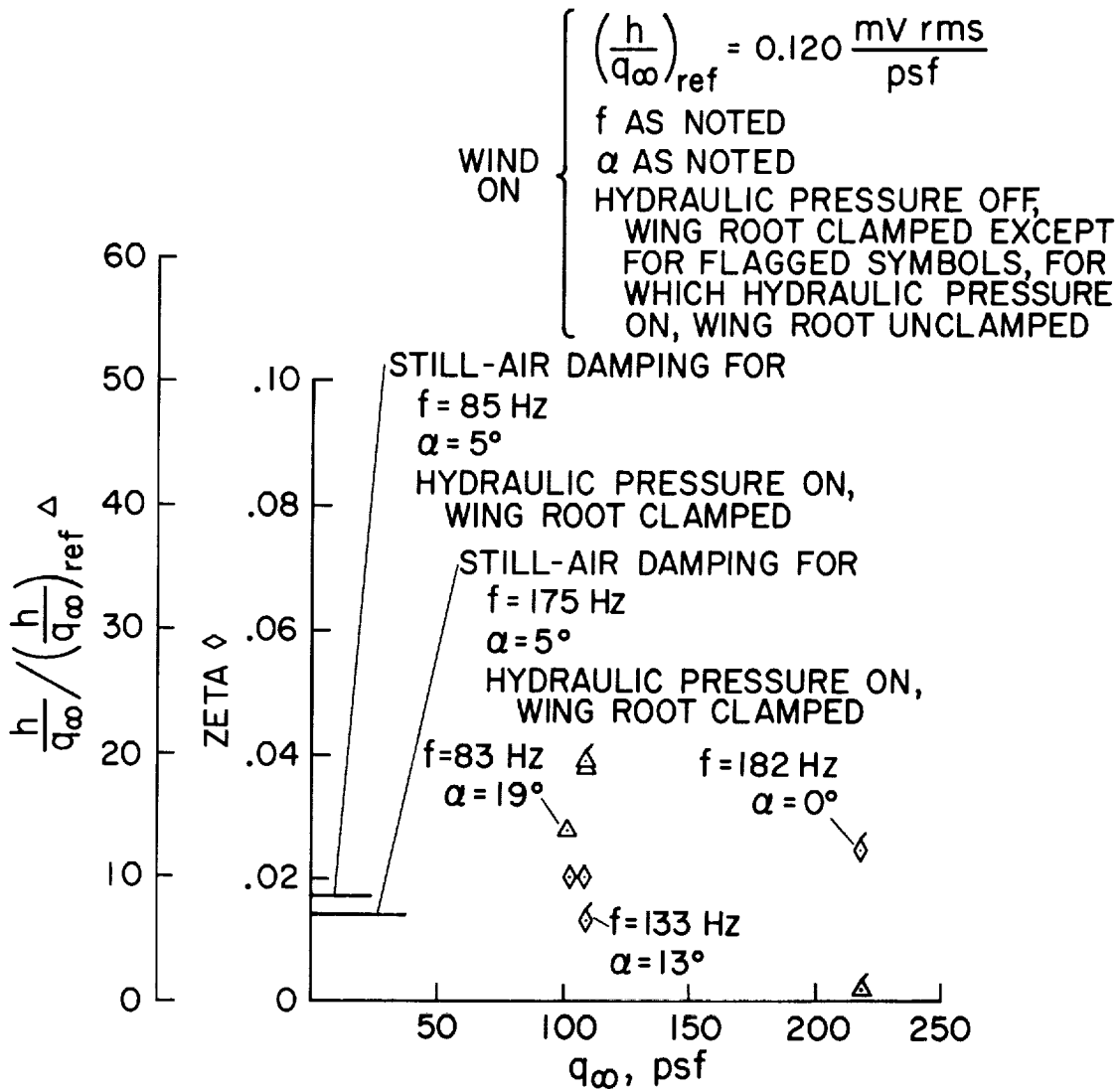
STILL-AIR DAMPING FOR
 $f = 32.3 \text{ Hz}$
 $\alpha = 60^\circ$
 HYDRAULIC PRESSURE ON,
 WING ROOT CLAMPED

STILL-AIR DAMPING FOR
 $f = 31.6 \text{ Hz}$
 $\alpha = 0^\circ$
 HYDRAULIC PRESSURE OFF,
 WING ROOT CLAMPED



(c) Bending at 34 Hz (1st bending).

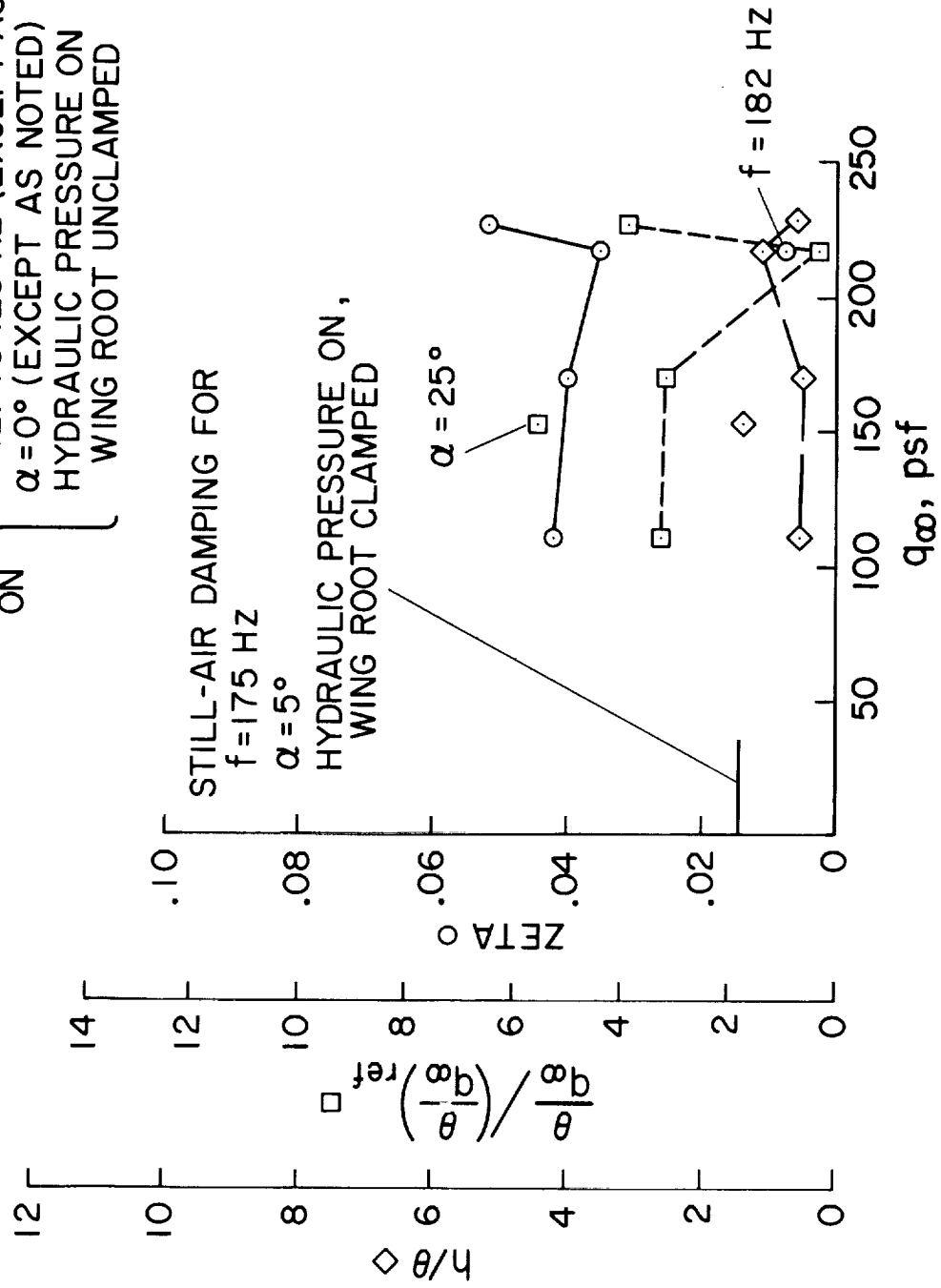
Figure 20.- Concluded.



(a) Bending at 83 Hz (2nd bending), 133 Hz (1st torsion and 3rd bending), and 182 Hz (3rd bending and 2nd torsion).

Figure 21.- Total damping and root mean square oscillations at $M = 0.60$ for wing "A".

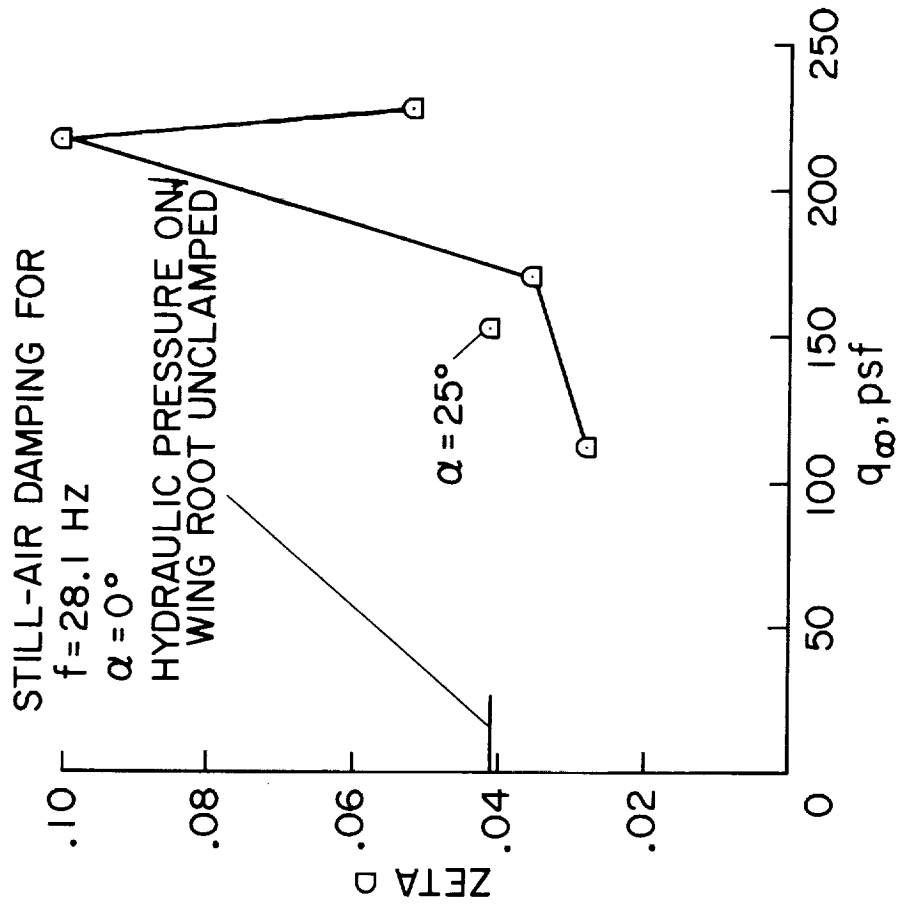
$\left(\frac{\theta}{q_{\infty}} \right)_{ref} = 0.187 \frac{mv \text{ rms}}{psf}$
 WIND ON }
 f = 121 TO 129 HZ (EXCEPT AS NOTED)
 $\alpha = 0^{\circ}$ (EXCEPT AS NOTED)
 HYDRAULIC PRESSURE ON
 WING ROOT UNCLAMPED



(b) Torsion at 121 to 129 Hz (1st torsion and 3rd bending) and 182 Hz (3rd bending and 2nd torsion).

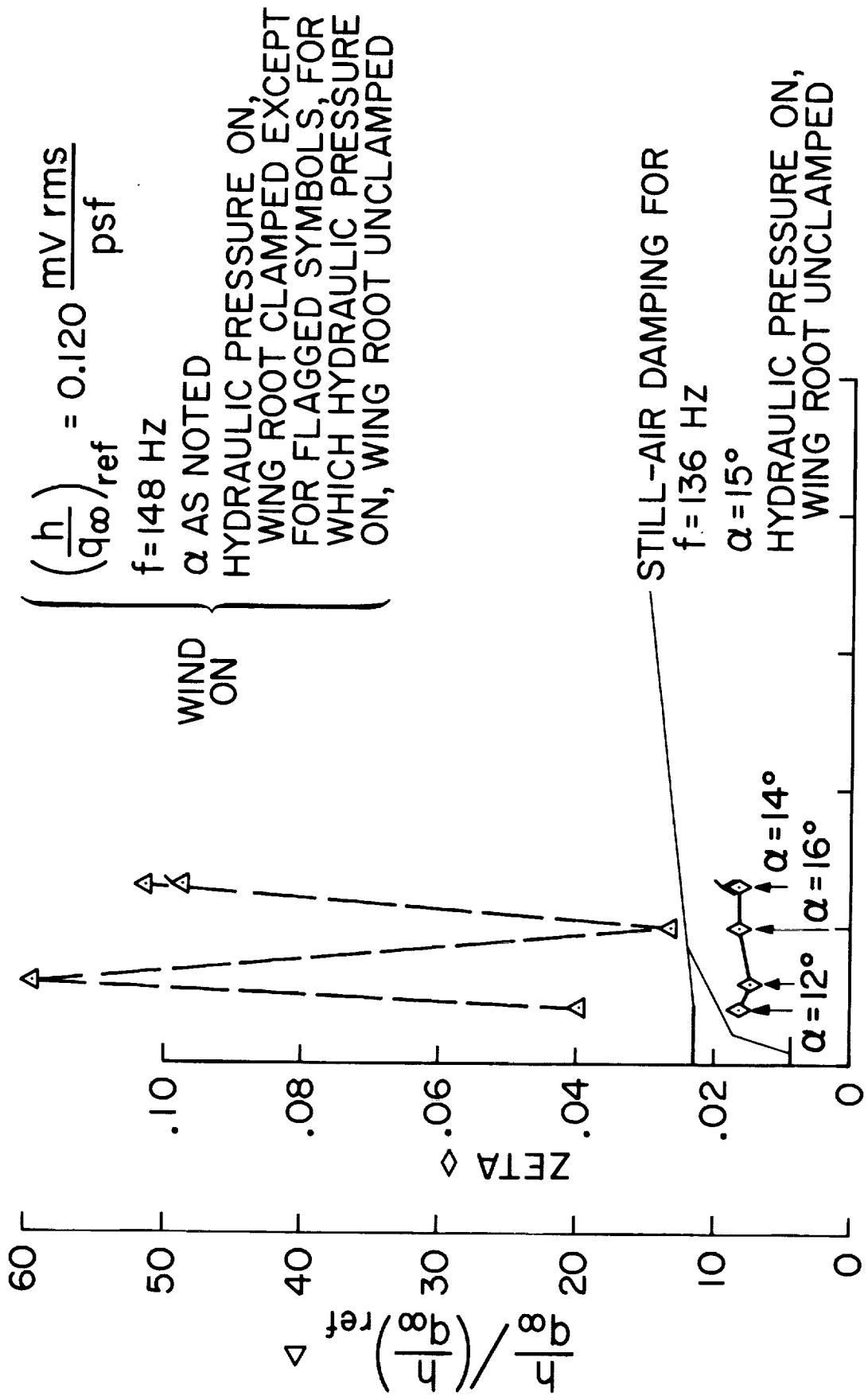
Figure 21.- Continued.

$f = 34 \text{ Hz}$
 $\alpha = 0^\circ$ (EXCEPT AS NOTED)
 WIND ON } HYDRAULIC PRESSURE ON,
 WING ROOT UNCLAMPED



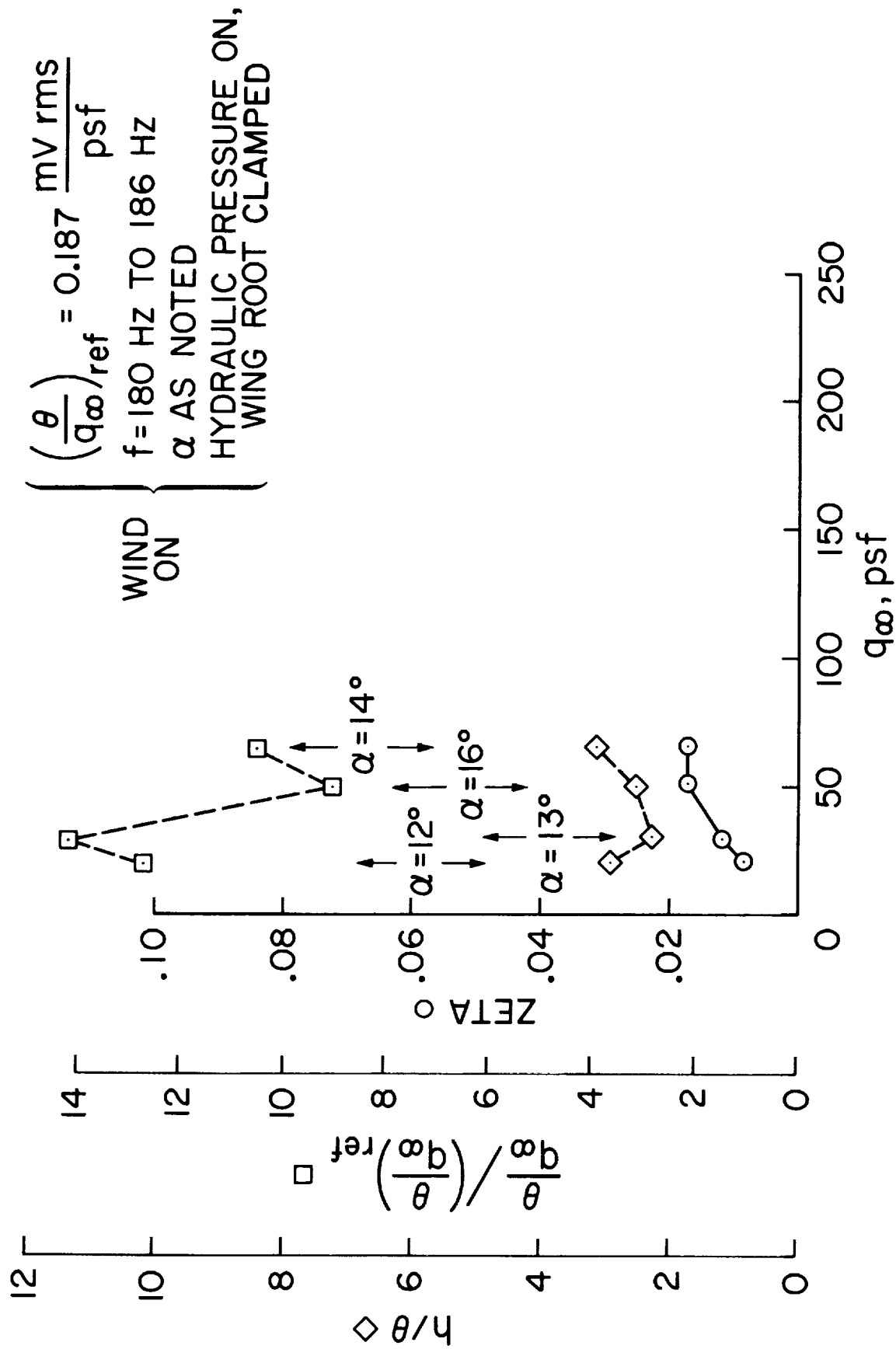
(c) Bending at 34 Hz (1st bending).

Figure 21.- Concluded.



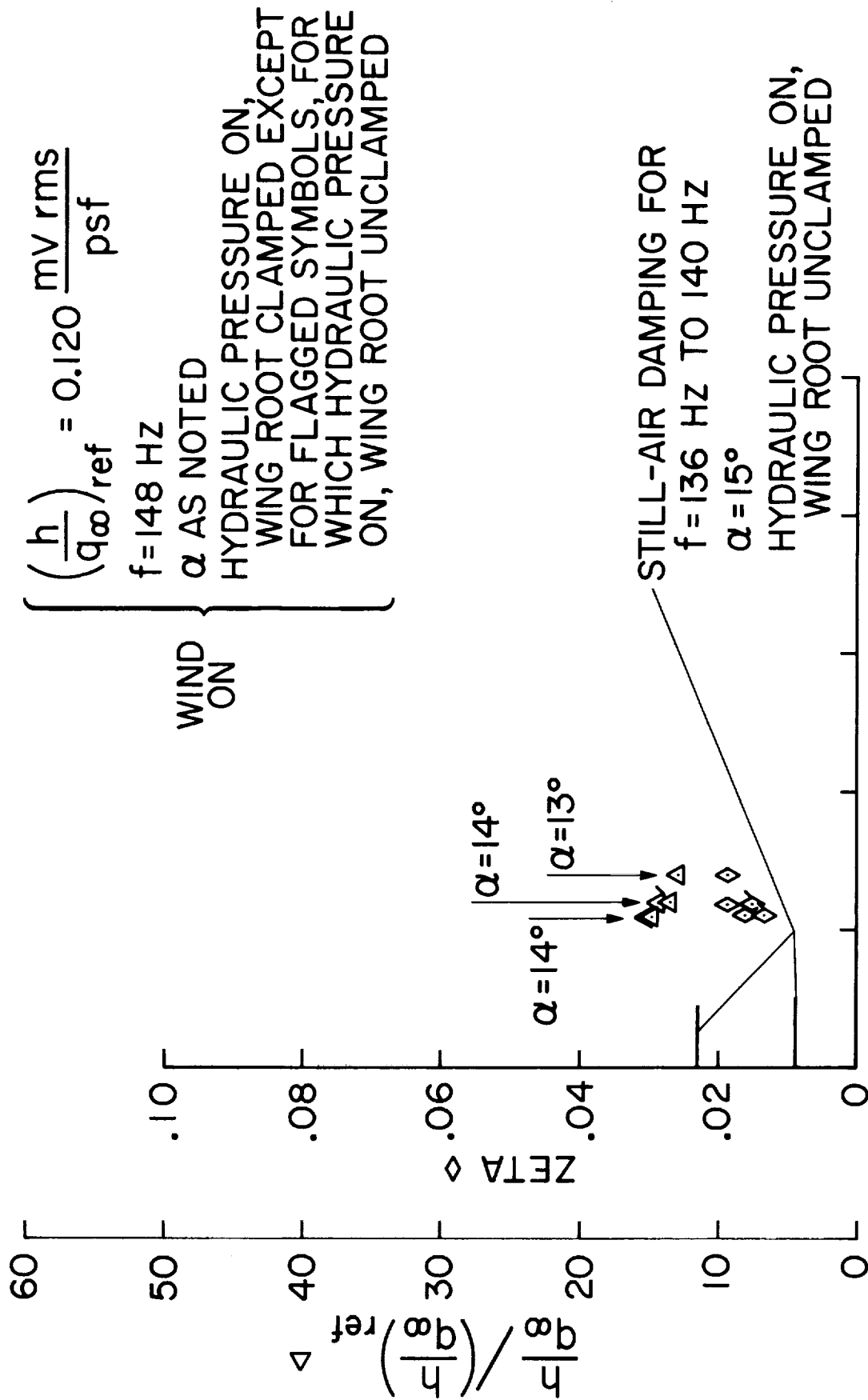
(a) Bending at 148 Hz (1st torsion).

Figure 22.- Total damping and root mean square oscillations at $M = 0.30$ for wing "B".



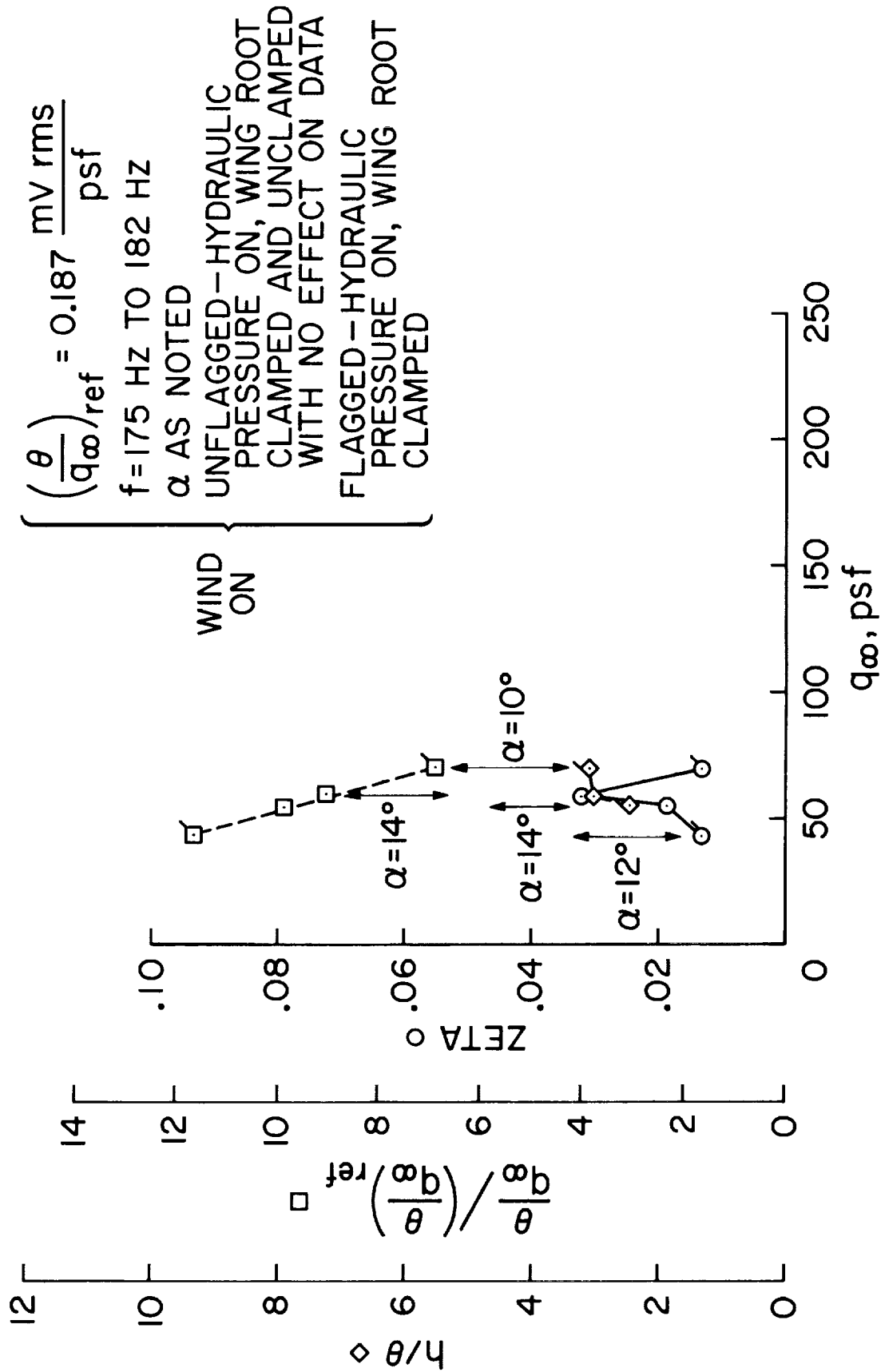
(b) Torsion at 180 Hz to 186 Hz (3rd bending).

Figure 22.- Concluded.



(a) Bending at 148 Hz (1st torsion).

Figure 23.- Total damping and root mean square oscillations at $M = 0.45$ for wing "B".



(b) Torsion at 175 Hz to 182 Hz (3rd bending).

Figure 23.- Concluded.

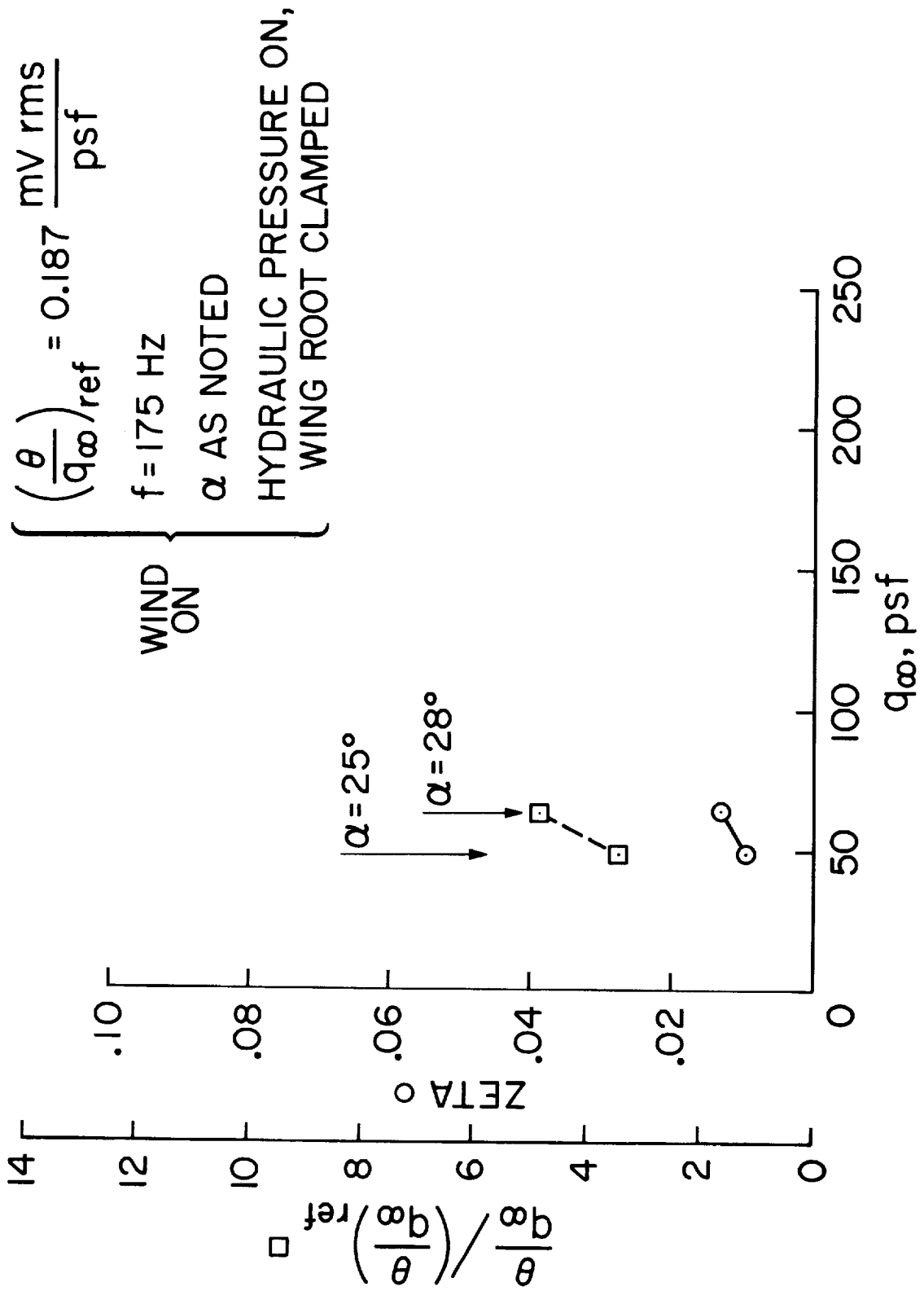


Figure 24.- Total damping and root mean square oscillations at $M = 0.29$ for wing BSP - torsion at 175 Hz (3rd bending).

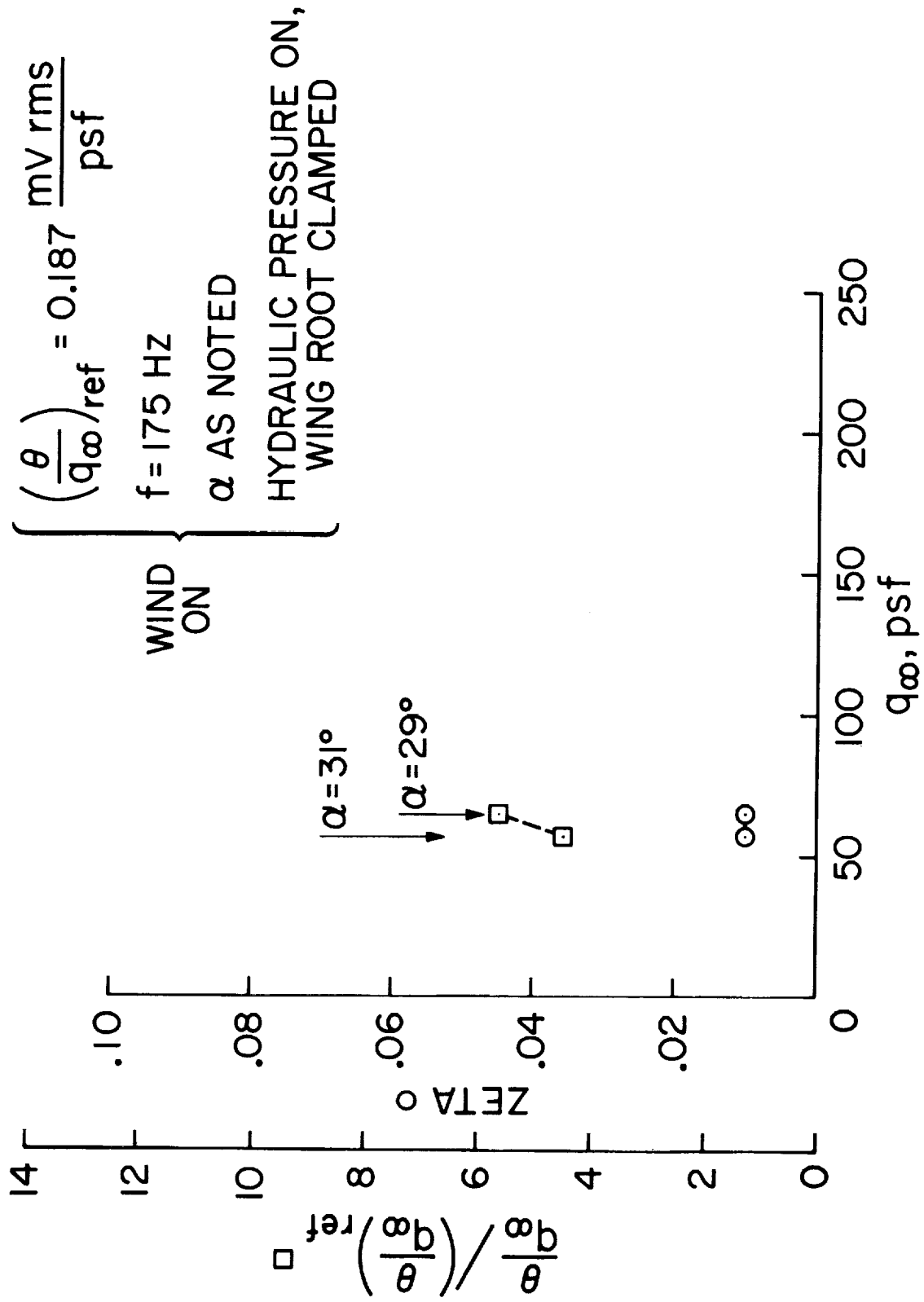


Figure 25.- Total damping and root mean square oscillations at $M = 0.45$ for wing BSP - torsion at 175 Hz (3rd bending).